UTILIZING ULTRAFAST SPECTROSCOPY TO STUDY CHARGE SEPARATION FOR SOLAR ENERGY CONVERSION

Melissa Katherine Gish

A dissertation submitted to the faculty at the University of North Carolina at Chapel Hill in partial fulfillment of the requirements for the degree of Doctor of Philosophy in the Department of Chemistry.

Chapel Hill
2018

Approved by:

John Papanikolas

Yosuke Kanai

Joanna Atkin

Jillian Dempsey

Marcey Waters

ABSTRACT

Melissa Katherine Gish: Utilizing Ultrafast Spectroscopy to Study Charge Separation for Solar Energy Conversion
(Under the Direction of John Papanikolas)

The ever-increasing demand for useable energy coupled with the depletion of fossil fuels require a shift to renewable energy resources. The dye-sensitized photoelectrosynthesis cell (DSPEC) takes inspiration from photosynthesis. The DSPEC is a tandem cell where a series of photon absorption and electron transfer events lead to water oxidation at a photoanode and CO_2 reduction at a photocathode to store energy in chemical bonds (solar fuels). While overall efficiencies can be determined through electrochemistry, these methods fail to reveal information about underlying charge separation dynamics that may inhibit performance. To develop a fully realized picture of these dynamics, we need to utilize time-resolved transient absorption spectroscopy.

This dissertation presents several systematic studies of charge separation dynamics on surfaces and in solution. We explored the thickness dependent interfacial dynamics of dye-sensitized core/shell films and how those dynamics change upon annealing these films. Next, we investigated the effects of immobilizing the dye on the surface with thin layers of a conductive metal oxide. Finally, we examined the length-dependent dynamics of a donor-acceptor system incorporating a thiophene oligomer donor and naphthalene diimide acceptors in solution. This work was made possible through extensive collaborations with the groups of Dr. Thomas J. Meyer and Dr. Kirk Schanze.

To my loving parents…

ACKNOWLEDGEMENTS

First, I would like to thank my advisor John Papanikolas for his support and guidance throughout my tenure at UNC. I have learned so much about science, communication, and teamwork as a part of the Papanikolas group and I will take these lessons with me throughout my career. I have had the privilege of working with amazing people throughout my time in the Papanikolas group. In particular, I would like to thank Stephanie Bettis for mentoring me in my first years, and Zach Morseth for being a great teammate. Additionally, I would also like to acknowledge Erika van Goethem, and Leah Bowers for being great coworkers and friends.

I would like to acknowledge Kyle Brennaman for his mentorship, and friendship throughout the years. I couldn't have done this without his input, teachings, and our numerous discussions about science and life. My other main collaborator, Alex Lapides, has been a great scientific partner and friend through grad school and beyond.

I would not have been able to get through this experience without the love and support of my family and friends. My parents, Tom and Lori Gish, have been incredibly supportive throughout my life and I would not be here without them. My oldest friends, Liz, Caitlin, Kathryn, Nicole, Max, Greg and Adam, have always been there for me, ready to chat, or just to laugh for over 15 years now and I am so proud of the people we have grown up to be.

I am so lucky to have met such great people in grad school who also happen to be amazing scientists and friends. Kita, you have been my partner in crime since the day we met and your support and ability to make me laugh are invaluable to me. From joining labs to orals to job

hunting to Kesha concerts, we have experienced so much together and I am a better person for knowing you. Thomas, you have been an incredible friend and mentor, and our coffee, lunch, TCSPC, and blue cup chats helped me get through many of the obstacles in this process. To say that I couldn't have made it through grad school without you two is an understatement. Gill and Nate, y'all have been amazing friends since day one and always provide great conversation and support. I would also like to thank Taylor and Dan for their friendship during this last year of grad school. I didn't expect to meet all of these lifelong friends when I started this process, but I am so grateful to know all of you.

Last, but certainly not least: Carter, thank you for all of your love and support for the past 5 years. I would not be here without you and Cal to come home to every day. I am looking forward to the years of adventures and fun ahead of us.

TABLE OF CONTENTS

LIST OF TABLES

LIST OF FIGURES

LIST OF ABBREVIATIONS AND SYMBOLS

A	absorbance
ΔA	change in absorbance
ALD	atomic layer deposition
a-TiO_2	amorphous titanium dioxide
bpy	2,2'- bipyridine
$bpy^{\bullet-}$	2,2'-bipyridine radical anion
BS	beam splitter
BBO	β-barium borate
°C	degrees Celsius
CaF_2	Calcium fluoride
CMOS	complementary metal oxide semiconductor
CO	carbon monoxide
CO_2	carbon dioxide
CPA	chirped pulse amplifier
CSS	charge separated state
CR	charge recombination
DSPEC	dye-sensitized photoelectrosynthesis cell
e^-	electron
e^- inj	electron injection
ESA	excited state absorption
ET	electron transfer
fsTA	femtosecond transient absorption
fs	femtosecond
FWHM	full width half maximum
GSB	ground state bleach
h	Planck's constant
h^+	hole

H^+	proton
H_2O	water
$HClO_4$	hydrochloric acid
k	rate constant
IR	infrared
ISC	intersystem crossing
L	lens
ln	natural logarithm
M	mirror
MeOH	methanol
^{1}MLCT	singlet metal-to-ligand charge transfer
^{3}MLCT	triplet metal-to-ligand charge transfer
ms	millisecond
μs	microsecond
ν	frequency
n-TiO_2	annealed, nanocrystalline titanium dioxide
NDI	naphthalene diimide
$NDI^{\bullet-}$	naphthalene diimide radical anion
NiO	nickel oxide
nm	nanometer
ns	nanosecond
nT	thiophene oligomer
nT-NDI	naphthalene diimide end-capped thiophene oligomers
O_2	oxygen gas
OPA	optical parametric amplifier
pH	logarithm of the reciprocal of hydrogen ion concentration
π-π*	pi-to-pi* transition
pT	poly(3-hexyl) thiophene

ps	picosecond
QY	quantum yield
R	775 nm reflector
Ru	ruthenium
Ru_{cat}	ruthenium catalyst
RuP	$[Ru^{II}(2,2'\text{-bpy})_2(4,4'\text{-}(PO_3H_2)_2\text{bpy})]^{2+}$
SE	stimulated emission
SnO_2	tin oxide
T	temperature
τ	time constant
TCO	transparent conducting oxide
TiO_2	titanium dioxide
TiTDMA	tetrakis(dimethylamido)titanium(IV)
TTA	triplet-triplet absorption
λ	wavelength
Zr^{4+}	zirconium ions
ZrO_2	zirconium dioxide

Chapter 1: Introduction

1.1. Overview.

The growing dependence on hydrocarbon-based energy around the world, especially in developing economies, cannot be sustained long-term. According to the Department of Energy (DOE), global energy consumption is expected to increase from 5.7×10^{20} J in 2012 to 8.1×10^{20} J in 2040.[1] Fossil fuels are predicted to make up 80% of this energy consumption, despite the continued depletion of our reserves. At current and predicted rates of consumption, fossil fuel reserves will not last through the next 1000 years.[2-4] Additionally, the burning of fossil fuels continues to create problems for the environment through the steady increase of global temperatures.

As global warming concerns rise, the race to develop viable fossil fuel alternatives is heating up. The global amount of carbon dioxide (CO_2) in the atmosphere eclipsed 400 ppm in 2015 and according to the National Oceanic and Atmospheric Administration (NOAA), the CO_2 levels in the atmosphere increased at a record pace for the second consecutive year in 2017.[5] The effects of global warming are increasingly visible. Rising sea levels, melting glaciers, and severe storms highlight the necessity for carbon-neutral energy sources to slow the rate of atmospheric CO_2 growth.

Solar energy is by far the most prominent carbon-neutral, renewable energy resource. Collecting sunlight from just 2% of the earth's surface for 8 hours using a solar energy conversion device with 12% efficiency would provide enough energy to power the globe for 2

weeks.[6] Current photovoltaic devices convert sunlight directly to electricity;[7-8] however, this presents a problem for periods of high power usage like nighttime and cloudy days. In order to shift our source of global power to the sun, we need to be able to appropriately store this solar energy for use at all times.

1.2. Artificial Photosynthesis.

Artificial photosynthesis implements a similar strategy to natural photosynthesis in plants, which uses sunlight to reduce CO_2 into sugar using water:

$$6CO_2 + 6H_2O + 48h\nu \rightarrow C_6H_{12}O_6 + 6O_2 \qquad (1.1)$$

In biological systems, such as photosystem II, an assembly of light-harvesting compounds (i.e. chromophores) work together to funnel light energy across the solar spectrum to reaction centers, where catalysis occurs.[9] Successful completion of the chemical reaction in equation 1.1 involves a complicated series of photon absorptions, electron transfer and catalytic events that has evolved over the course of billions of years.[10] Artificial photosynthesis looks to simplify the natural photosynthetic process to convert sunlight into carbon-based fuels.[7] One strategy for artificial photosynthesis is the dye-sensitized photoelectrosynthesis cell (DSPEC) (Figure 1.1).[11] In the DSPEC, two separate photoelectrodes are connected in tandem: a photoanode for water oxidation, and a photocathode for CO_2 reduction.

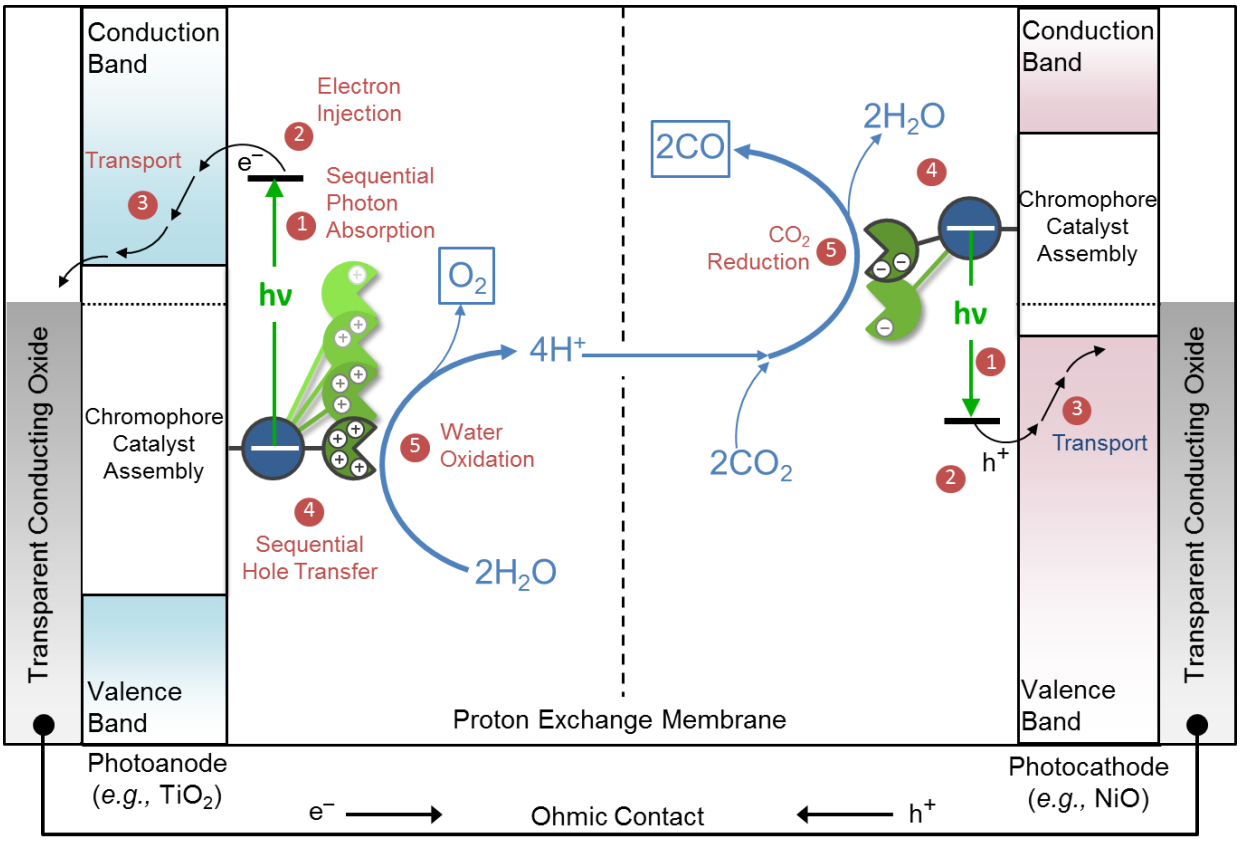

Figure 1.1. Schematic of the tandem dye-sensitized photoelectrosynthesis cell (DSPEC) for water oxidation (photoanode) and CO_2 reduction (photocathode). The events at the photoanode are (1) light absorption by the chromophore, (2) electron injection into the conduction band of the semiconductor, (3) transport of the electron through the semiconductor to the transparent conducting oxide (TCO) for transfer to the photocathode, (4) intra-assembly hole transfer from the chromophore to the catalyst, (5) repetition of steps 1-4 four times to catalytically oxidize water to oxygen and 4 protons (H^+) that assist in CO_2 reduction at the photocathode. At the photocathode, (1) light absorption by the chromophore is followed by (2) hole injection into the valence band of the semiconductor. The hole is (3) transported through the semiconductor to the TCO. (4) Intra-assembly electron transfer from the chromophore to the reduction catalyst occurs and (5) CO_2 reduction to CO occurs.

1.3. The Dye-Sensitized Photoelectrosynthesis Cell (DSPEC).

Each electrode in the DSPEC starts with a wide band-gap semiconductor transparent in the visible region of the solar spectrum, such as titanium dioxide (TiO_2, 3.2 eV),[6] and tin oxide (SnO_2, 3.6 eV).[12] The position of the conduction band (CB) of the n-type semiconductor (e.g. TiO_2, SnO_2) at the photoanode and valence band (VB) of the p-type semiconductor at the photocathode (e.g. NiO) must be sufficient to accept electrons or holes from photoexcited chromophores adsorbed to the surface (Figure 1.1, Step 2). The oxidized or reduced chromophore transfers an equivalent out to a catalyst (Figure 1.1, Step 4), resetting the chromophore to absorb another photon. These photoinduced electron transfer processes repeat multiple times on either side prior to catalysis. The bulk of this dissertation focuses on characterization of the photoanode, therefore, the following discussion focuses on the events occurring at the photoanode.

The photoinduced processes at the photoanode are illustrated as a series of four photoactivation steps in Figure 1.2. Each photoactivation step includes a light absorption event followed by electron injection into the semiconductor CB and oxidative equivalent transfer to the catalyst. The thermodynamic driving force and, thus, the rate, for oxidative equivalent transfer decreases with each subsequent photoactivation step. Additionally, changes at the activation site of the catalyst as it moves through the catalytic cycle are rate limiting, in particular, the O-O bond formation between the 3rd and 4th photoactivation steps. Deleterious charge recombination, or back electron transfer (BET), can occur between the injected electrons and the oxidized chromophore, or catalyst at any step in the process. BET becomes increasingly competitive at higher photoactivation steps, and as such, the first photoactivation step is the best characterized under open circuit conditions. Because the processes in the first step occur on the picosecond

time scale, we must utilize femtosecond transient absorption spectroscopy (fsTA) to fully realize these dynamics. **Chapter 2** details the fsTA setup used in these experiments including a home-built optical parametric amplifier (OPA) that generates a range of wavelengths for our excitation pulse.

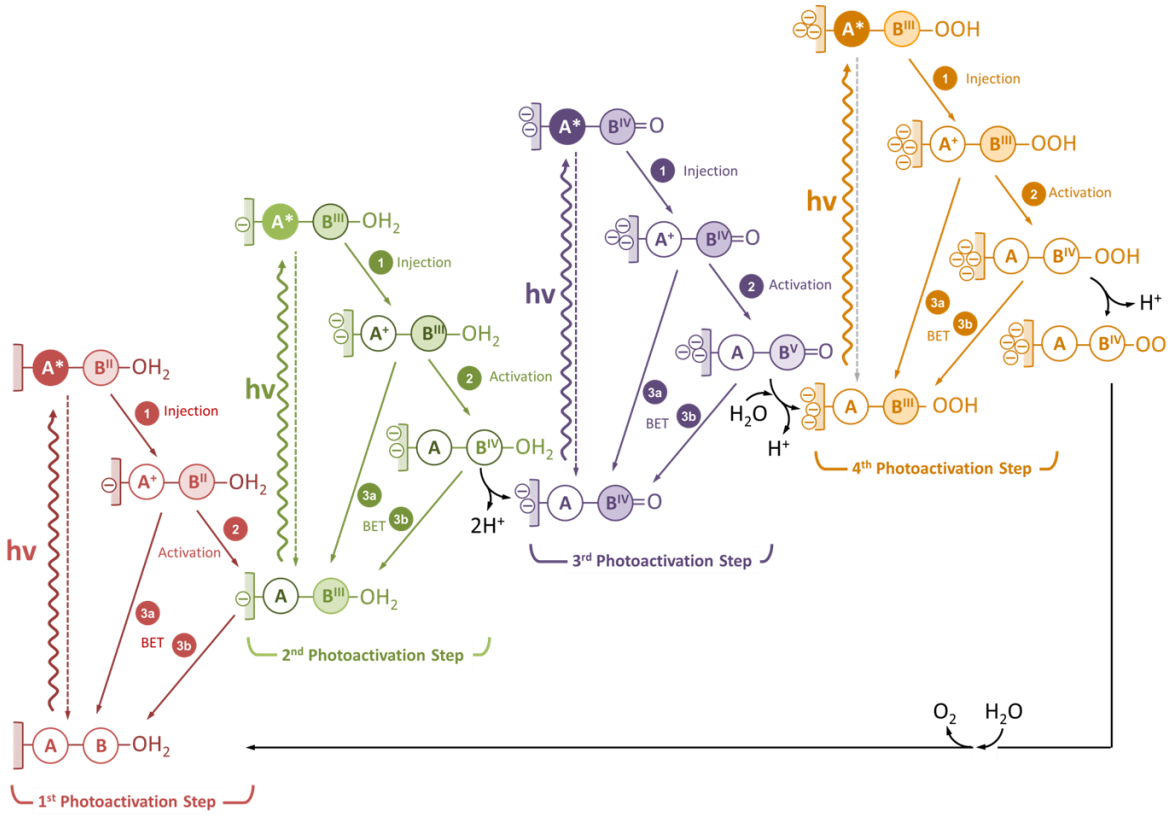

Figure 1.2. Illustration of the kinetic scheme of the four photoactivation steps involved in water oxidation at a DSPEC photoanode.

A well-studied chromophore that can act as the light absorber is a ruthenium tris(bipyridine) ($Ru^{II}(bpy)_3)^{2+}$) derivative, $[Ru^{II}(bpy)_2(4,4'\text{-}(PO_3H_2)_2bpy)]^{2+}$ (**RuP^{2+}**) (Figure 1.3B). The excited-state oxidation potential of **RuP^{2+}** ($E°'(Ru^{3+/2+*})$ = -0.52 V vs NHE)[13] is appropriately positioned to inject electrons into the CB of TiO_2 or SnO_2, which lie at -0.1 V vs. NHE and +0.3 V vs. NHE, respectively.[14] Excited-state electron injection from **RuP^{2+*}** (Figure 1.1, Step 2) can occur

via three pathways: direct, ultrafast, and picosecond. In a direct injection mechanism, the electron is photoexcited from the ground state directly into the CB of the semiconductor.[15]

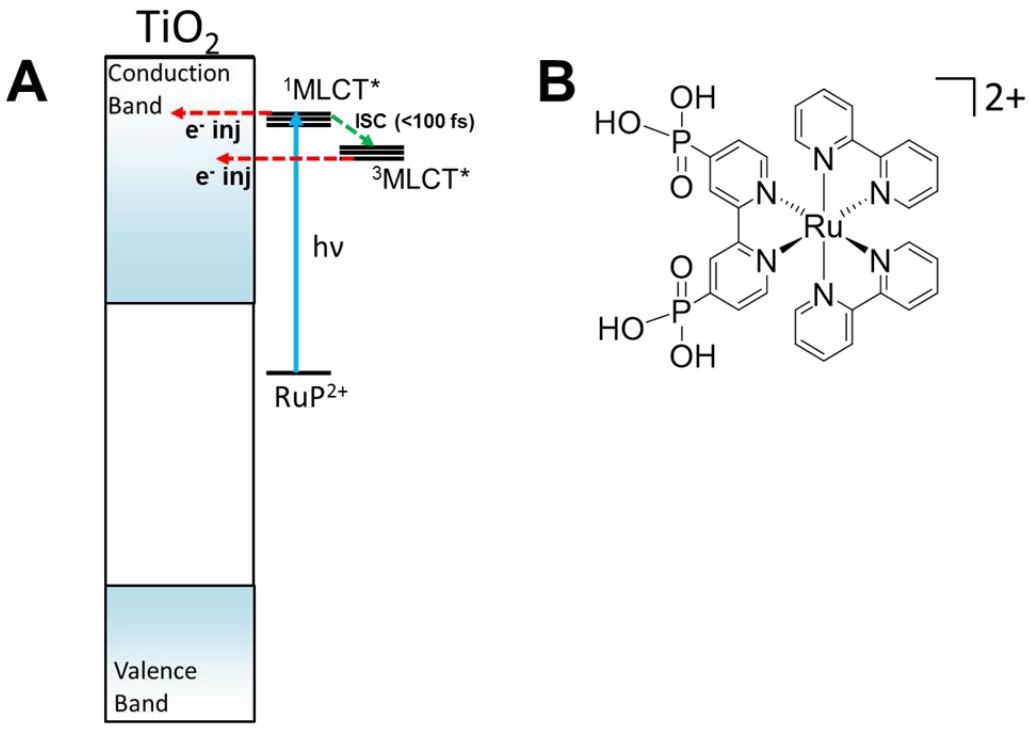

Figure 1.3. (A) Illustration of the ultrafast and picosecond injection processes from photoexcited **RuP^{2+}** (**RuP^{2+*}**) into the conduction band of TiO_2. (B) Chemical structure of $[Ru^{II}(bpy)_2(4,4'\text{-}(PO_3H_2)_2bpy)]^{2+}$ (**RuP^{2+}**).

Ultrafast and picosecond injection are step-wise mechanisms (Figure 1.3A), where photoexcitation of the **RuP^{2+}** creates a singlet metal-to-ligand charge transfer (^{1}MLCT) state. The ^{1}MLCT can inject into the CB or undergo rapid intersystem crossing (ISC) to a triplet MLCT state (^{3}MLCT) within ~100 fs. Electron injection on the picosecond time scale is competitive with vibrational relaxation through the ^{3}MLCT excited state manifold. The rate of electron injection depends on the overlap between the excited-state manifold and the density of

states of the semiconductor CB.[16] Injection from vibrationally "hot" ^{3}MLCT state occurs on the 10s ps time scale, while injection in conjunction with vibrational relaxation continues through the 100s ps time scale.

Oxidative equivalent (hole) transfer (Figure 1.1, Step 4) from the oxidized chromophore ($\mathbf{RuP^{3+}}$) to a water oxidation catalyst ($\mathbf{Ru_{cat}^{2+}}$) is fast and efficient. The first photoactivation step of three chromophore-catalyst assemblies were thoroughly characterized by the Papanikolas group, where chromophore and catalyst are attached via a peptide backbone, an alkyl bridge, and in a bilayer configuration via a zirconium (Zr^{4+}) bridge. The time scale for hole transfer is 380 ps,[17] 145 ps,[18] and 170 ps[19] for the peptide, alkyl, and bilayer configurations, respectively with 100% efficiency. Despite the assembly configuration, however, charge recombination between the oxidized catalyst and the injected electron is fast, where τ = 1 μs,[17] 6.7 μs,[18] 760 ns[19] for peptide, alkyl, and bilayer, respectively.

1.4. Core/Shell Advantage.

Synthetic strategies to extend the lifetime of the charge separated state between the injected electrons and oxidized surface species have had limited success.[17-21] Instead, efforts have turned to manipulating the semiconductor surface to physically separate the injected electrons and holes via an energetic barrier. In particular, a core/shell strategy demonstrates significant improvement in device performances over simple nanocrystalline films.[22-29] Core/shell films are constructed via atomic layer deposition (ALD), where a thin layer of a metal oxide is deposited on a mesoporous nanocrystalline film followed by dye sensitization. The core and shell are chosen based on the relative positions of their CB edges to allow excited state injection into the shell, followed by electron transfer to the core, but recombination from electrons in the core is slowed by a thermodynamic barrier introduced by the shell.[30-31] In SnO_2/TiO_2 core/shell films (Figure

1.4A), for example, the SnO_2 CB edge lies more positive than that of TiO_2, where electrons localized in the core must surmount a 0.4 eV barrier or tunnel through the shell to recombine with an oxidized chromophore or catalyst.[24-25]

Devices incorporating core/shell films perform significantly better as photoanodes than TiO_2 or SnO_2 alone; however, faradaic efficiencies and oxygen production in these devices remain low.[22-23] **Chapter 3** of this dissertation explores the interfacial dynamics of dye-sensitized SnO_2/TiO_2 core/shell films (SnO_2/TiO_2|**RuP**$^{2+}$) as deposited, i.e., an amorphous TiO_2 shell (*a*-TiO_2), and **Chapter 4** reveals the changes in these dynamics upon annealing the core/shell films, producing a nanocrystalline shell (*n*-TiO_2).

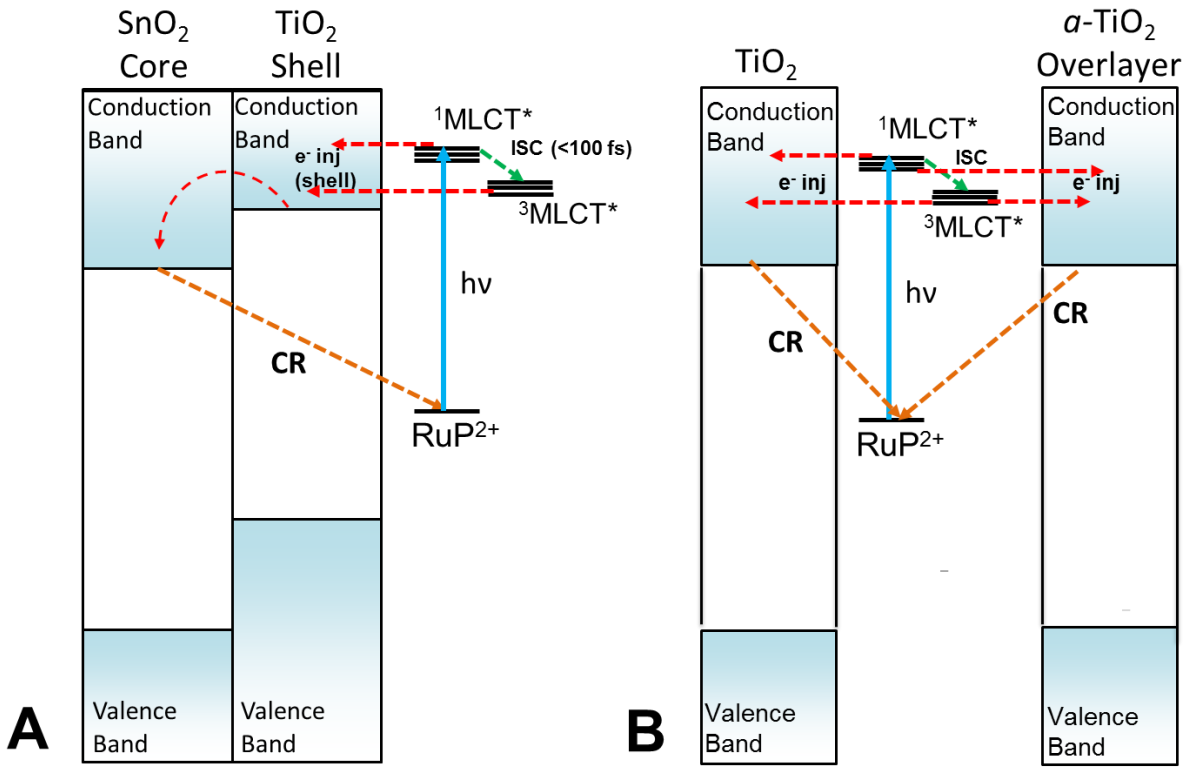

Figure 1.4. (A) Illustration of photoinduced processes occurring at the SnO_2/TiO_2|**RuP**$^{2+}$ interface. (B) Illustration of photoinduced processes occurring in "buried" photoanodes, where

RuP^{2+} is covered in ~2 nm of ALD TiO_2 (TiO_2|**RuP^{2+}**|*a*-TiO_2). ^{1}MLCT = singlet metal-to-ligand charge transfer state; ^{3}MLCT = triplet metal-to-ligand charge transfer state; ISC = intersystem crossing; e^- inj = electron injection; CR= charge recombination.

1.5. "Buried" Chromophores.

In addition to issues with fast recombination, surface instability of the adsorbed chromophores is a substantial problem in DSPECs, particularly in basic conditions where water oxidation is more efficient.[13] A thin layer of ALD TiO_2 protects the dye from desorption and degradation, enhancing surface stability both in the dark and under illumination. Thicker layers of ALD, completely burying the chromophore (~2 nm), allows for facile construction of chromophore-catalyst assemblies, where the catalyst is loaded onto the ALD surface and protected with a few extra layers of ALD.[32-33] The systematic effects of burying the chromophore on the surface has not been extensively studied. In **Chapter 5**, transient absorption spectroscopy is used to understand the effects of different overlayer thicknesses on the interfacial dynamics and its impact on DSPEC design.

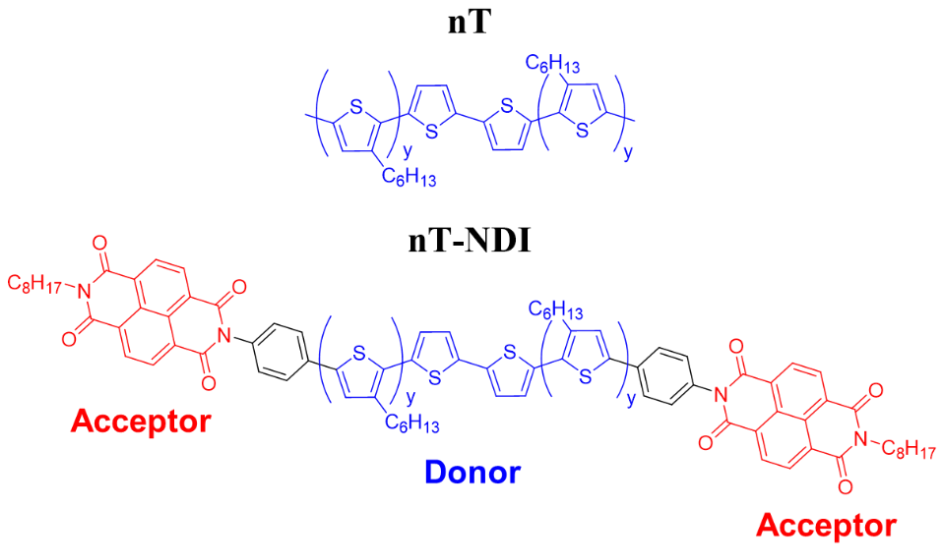

Figure 1.5. Thiophene (**nT**, top) and thiophene oligomer donors end-capped with naphthalene diimide acceptors (**nT-NDI**, bottom), where n = 2(y+1) and y = 1, 2, 3, 4, or 5.

1.6. Donor-Acceptor Oligomers.

Chapter 6 of this dissertation focuses on a different aspect of solar cell design: light-harvesting. Ruthenium chromophores absorb only a small portion of the solar spectrum, limiting the potential efficiencies of DSPECs and other solar energy devices. Polymers, such as poly(3-hexyl)thiophene (**pT**) have a significant amount of π-conjugation, which allows them to absorb a wider range of the solar spectrum.[34] These π-conjugated polymers are effective electron donors; however, the heterogeneity of polymer size and composition complicates quantifying rates and mechanisms of charge separation when incorporated into a donor-acceptor system. Synthesis of oligomers is controlled and precise making them powerful model systems for understanding larger-scale dynamics. Additionally, these oligomers are often integrated into molecular-wire like systems and utilized in solar energy conversion devices themselves.[35-36] The charge separation and recombination dynamics of thiophene oligomers (**nT**) end-capped with NDI

acceptor units (**nT-NDI**) as a function of length with 4, 6, 8, 10, and 12 (Figure 1.5) thiophene units were studied using transient absorption spectroscopy.

REFERENCES

1. Annual Energy Outlook. *U.S. Department of Energy* **2013,** *Washington, DC*.

2. Dresselhaus, M. S.; Thomas, I. L. Alternative energy technologies. *Nature* **2001,** *414* (6861), 332-337.

3. Lewis, N. S.; Nocera, D. G. Powering the planet: Chemical challenges in solar energy utilization. *Proc. Natl. Acad. Sci. U. S. A.* **2006,** *103* (43), 15729-15735.

4. Shafiee, S.; Topal, E. When will fossil fuel reserves be diminished? *Energ Policy* **2009,** *37* (1), 181-189.

5. Trends in Atmospheric Carbon Dioxide. *National Oceanic and Atmospheric Administration* **2018**.

6. Ashford, D. L.; Gish, M. K.; Vannucci, A. K.; Brennaman, M. K.; Templeton, J. L.; Papanikolas, J. M.; Meyer, T. J. Molecular Chromophore-Catalyst Assemblies for Solar Fuel Applications. *Chem. Rev.* **2015,** *115* (23), 13006-13049.

7. Concepcion, J. J.; House, R. L.; Papanikolas, J. M.; Meyer, T. J. Chemical Approaches to Artificial Photosynthesis. *Proc. Natl. Acad. Sci. U. S. A.* **2012,** *109* (39), 15560-15564.

8. O'Regan, B.; Gratzel, M. A low-cost, high-efficiency solar cell based on dye-sensitized colloidal TiO_2 films. *Nature* **1991,** *353*, 737-740.

9. Ferreira, K. N.; Iverson, T. M.; Maghlaoui, K.; Barber, J.; Iwata, S. Architecture of the photosynthetic oxygen-evolving center. *Science* **2004,** *303* (5665), 1831-1838.

10. Barber, J. Engine of life and big bang of evolution: a personal perspective. *Photosynth Res* **2004,** *80* (1-3), 137-+.

11. Brennaman, M. K.; Dillon, R. J.; Alibabaei, L.; Gish, M. K.; Dares, C. J.; Ashford, D. L.; House, R. L.; Meyer, G. J.; Papanikolas, J. M.; Meyer, T. J. Finding the Way to Solar Fuels with Dye-Sensitized Photoelectrosynthesis Cells. *J. Am. Chem. Soc.* **2016,** *138* (40), 13085-13102.

12. Ganose, A. M.; Scanlon, D. O. Band gap and work function tailoring of SnO2 for improved transparent conducting ability in photovoltaics. *J Mater Chem C* **2016,** *4* (7), 1467-1475.

13. Hanson, K.; Brennaman, M. K.; Ito, A.; Luo, H. L.; Song, W. J.; Parker, K. A.; Ghosh, R.; Norris, M. R.; Glasson, C. R. K.; Concepcion, J. J., et al. Structure-Property Relationships in Phosphonate-Derivatized, Ru^{II} Polypyridyl Dyes on Metal Oxide Surfaces in an Aqueous Environment. *J. Phys. Chem. C* **2012,** *116* (28), 14837-14847.

14. Knauf, R. R.; Brennaman, M. K.; Alibabaei, L.; Norris, M. R.; Dempsey, J. L. Revealing the Relationship between Semiconductor Electronic Structure and Electron Transfer Dynamics at Metal Oxide-Chromophore Interfaces. *J. Phys. Chem. C* **2013,** *117* (48), 25259-25268.

15. Miller, S. A.; West, B. A.; Curtis, A. C.; Papanikolas, J. M.; Moran, A. M. Communication: Uncovering molecule-TiO2 interactions with nonlinear spectroscopy. *J Chem Phys* **2011,** *135* (8).

16. Zigler, D. F.; Morseth, Z. A.; Wang, L.; Ashford, D. L.; Brennaman, M. K.; Grumstrup, E. M.; Brigham, E. C.; Gish, M. K.; Dillon, R. J.; Alibabaei, L., et al. Disentangling the Physical Processes Responsible for the Kinetic Complexity in Interfacial Electron Transfer of Excited Ru(II) Polypyridyl Dyes on TiO_2. *J. Am. Chem. Soc.* **2016,** *138* (13), 4426-4438.

17. Bettis, S. E.; Ryan, D. M.; Gish, M. K.; Alibabaei, L.; Meyer, T. J.; Waters, M. L.; Papanikolas, J. M. Photophysical Characterization of a Helical Peptide Chromophore-Water Oxidation Catalyst Assembly on a Semiconductor Surface using Ultrafast Spectroscopy. *J. Phys. Chem. C* **2014,** *118* (12), 6029-6037.

18. Wang, L.; Ashford, D. L.; Thompson, D. W.; Meyer, T. J.; Papanikolas, J. M. Watching Photoactivation in a Ru(II) Chromophore-Catalyst Assembly on TiO_2 by Ultrafast Spectroscopy. *J. Phys. Chem. C* **2013,** *117* (46), 24250-24258.

19. Bettis, S. E.; Hanson, K.; Wang, L.; Gish, M. K.; Concepcion, J. J.; Fang, Z.; Meyer, T. J.; Papanikolas, J. M. Photophysical Characterization of a Chromophore/Water Oxidation Catalyst Containing a Layer-by-Layer Assembly on Nanocrystalline TiO_2 using Ultrafast Spectroscopy. *J. Phys. Chem. A* **2014,** *118* (45), 10301-10308.

20. Ning, Z.; Fu, Y.; Tian, H. Improvement of Dye-Sensitized Solar Cells: What We Know and What We Need to Know. *Energy Envrion. Sci.* **2010,** *3* (9), 1170-1181.

21. Koumura, N.; Wang, Z. S.; Mori, S.; Miyashita, M.; Suzuki, E.; Hara, K. Alkyl-Functionalized Organic Dyes for Efficient Molecular Photovoltaics. *J. Am. Chem. Soc.* **2006,** *128* (44), 14256-14257.

22. Sherman, B. D.; Ashford, D. L.; Lapides, A. M.; Sheridan, M. V.; Wee, K. R.; Meyer, T. J. Light-Driven Water Splitting with a Molecular Electroassembly-Based Core/Shell Photoanode. *J. Phys. Chem. Lett.* **2015,** *6* (16), 3213-3217.

23. Alibabaei, L.; Sherman, B. D.; Norris, M. R.; Brennaman, M. K.; Meyer, T. J. Visible Photoelectrochemical Water Splitting into H_2 and O_2 in a Dye-Sensitized Photoelectrosynthesis Cell. *Proc. Natl. Acad. Sci. U. S. A.* **2015,** *112* (19), 5899-5902.

24. Knauf, R. R.; Kalanyan, B.; Parsons, G. N.; Dempsey, J. L. Charge Recombination Dynamics in Sensitized SnO_2/TiO_2 Core/Shell Photoanodes. *J. Phys. Chem. C* **2015,** *119* (51), 28353-28360.

25. Gish, M. K.; Lapides, A. M.; Brennaman, M. K.; Templeton, J. L.; Meyer, T. J.; Papanikolas, J. M. Ultrafast Recombination Dynamics in Dye-Sensitized SnO2/TiO2 Core/Shell Films. *J. Phys. Chem. Lett.* **2016,** *7* (24), 5297-5301.

26. Swierk, J. R.; McCool, N. S.; Nemes, C. T.; Mallouk, T. E.; Schmuttenmaer, C. A. Ultrafast Electron Injection Dynamics of Photoanodes for Water-Splitting Dye-Sensitized Photoelectrochemical Cells. *J. Phys. Chem. C* **2016,** *120* (11), 5940-5948.

27. McCool, N. S. S., J. R.; Nemes, C. T.; Schmuttenmaer, C. A.; Mallouk, T. E. Dynamics of Electron Injection in SnO_2/TiO_2 Core/Shell Electrodes for Water-Splitting Dye-Sensitized Photoelectrochemical Cells. *J. Phys. Chem. Lett.* **2016,** *7*, 2930-2934.

28. Kay, A.; Gratzel, M. Dye-Sensitized Core-Shell Nanocrystals: Improved Efficiency of Mesoporous Tin Oxide Electrodes Coated with a Thin Layer of an Insulating Oxide. *Chem. Mater.* **2002,** *14* (7), 2930-2935.

29. Karlsson, M.; Jogi, I.; Eriksson, S. K.; Rensmo, H.; Boman, M.; Boschloo, G.; Hagfeldt, A. Dye-Sensitized Solar Cells Employing a SnO_2-TiO_2 Core-shell Structure Made by Atomic Layer Deposition. *Chimia* **2013,** *67* (3), 142-148.

30. Palomares, E.; Clifford, J. N.; Haque, S. A.; Lutz, T.; Durrant, J. R. Control of Charge Recombination Dynamics in Dye Sensitized Solar Cells by the Use of Conformally Deposited Metal Oxide Blocking Layers. *J. Am. Chem. Soc.* **2003,** *125* (2), 475-482.

31. Palomares, E.; Clifford, J. N.; Haque, S. A.; Lutz, T.; Durrant, J. R. Slow Charge Recombination in Dye-Sensitised Solar Cells (DSSC) using Al_2O_3 Coated Nanoporous TiO_2 Films. *Chem. Commun.* **2002,** (14), 1464-1465.

32. Lapides, A. M.; Sherman, B. D.; Brennaman, M. K.; Dares, C. J.; Skinner, K. R.; Templeton, J. L.; Meyer, T. J. Synthesis, Characterization, and Water Oxidation by a Molecular Chromophore-Catalyst Assembly Prepared by Atomic Layer Deposition. The "Mummy" Strategy. *Chem. Sci.* **2015,** *6* (11), 6398-6406.

33. Tian, L.; Fohlinger, J.; Pati, P. B.; Zhang, Z. B.; Ling, J. Z.; Yang, W. X.; Johansson, M.; Kubart, T.; Sun, J. L.; Boschloo, G., et al. Ultrafast dye regeneration in a core-shell NiO-dye-TiO2 mesoporous film. *Phys. Chem. Chem. Phys.* **2018,** *20* (1), 36-40.

34. Roncali, J. Conjugated Poly(Thiophenes) - Synthesis, Functionalization, and Applications. *Chem. Rev.* **1992,** *92* (4), 711-738.

35. Wasielewski, M. R. Photoinduced Electron-Transfer in Supramolecular Systems for Artificial Photosynthesis. *Chem. Rev.* **1992,** *92* (3), 435-461.

36. Gilbert, M.; Albinsson, B. Photoinduced charge and energy transfer in molecular wires. *Chem Soc Rev* **2015,** *44* (4), 845-862.

Chapter 2: Instrumentation

2.1. Transient Absorption Description.

Transient absorption spectroscopy is a pump-probe technique that is used to follow the dynamics of a system on time scales ranging from femtoseconds through milliseconds. The bulk of the work in this dissertation utilizes a femtosecond transient absorption spectroscopy (fsTA) setup shown in Figure 2.1 and described previously.[1-3] Using this setup, we can monitor the photophysical phenomena of charge separation and recombination on surfaces and in solution from femtoseconds through 1.2 ns.

The pump and probe in this fsTA setup are derived from the same laser source: a 1 kHz Ti-Sapphire chirped-pulse amplifier (Clark-MXR, CPA-2001). The output of the CPA-2001 is 775 nm with a 150 fs pulse width, measured through autocorrelation (~240 fs FWHM). The layout of our experimental setup is illustrated in Figure 2.1. At the output, the beam is split by a 90:10 beamsplitter (BS), where 90% of the beam travels to the optical parametric amplifier (OPA, Section 2.2) to generate the pump pulse. The pump pulse is chopped at 500 Hz and sent through a half-wave ($\lambda/2$) plate and neutral density wheel to control the polarization and power, respectively.

The remaining 10% of the 775 nm output is used to generate the white light probe pulse and a small portion (5%) of this 10% is split off to monitor the autocorrelation width. To delay the probe in time relative to the pump pulse, the beam is sent through a computer-controlled mechanical delay stage. The 775 nm beam is focused into a translating CaF_2 window and

undergoes spectral broadening through supercontinuum generation. The white light probe extends from 325 nm through 750 nm and set to horizontal polarization. The pump polarization is set to magic angle (54.7°) relative to the probe pulse using the half-wave plate. Pump and probe beams are focused to ~150 μm spots and spatially overlapped at the sample. A fiber optic-coupled multichannel spectrometer with a CMOS sensor coupled detects the pulse-to-pulse changes in the white light probe before and after pump excitation as the delay stage moves from negative delays through 1.2 ns. The instrument response is ~150 fs with 0.1 mOD resolution.

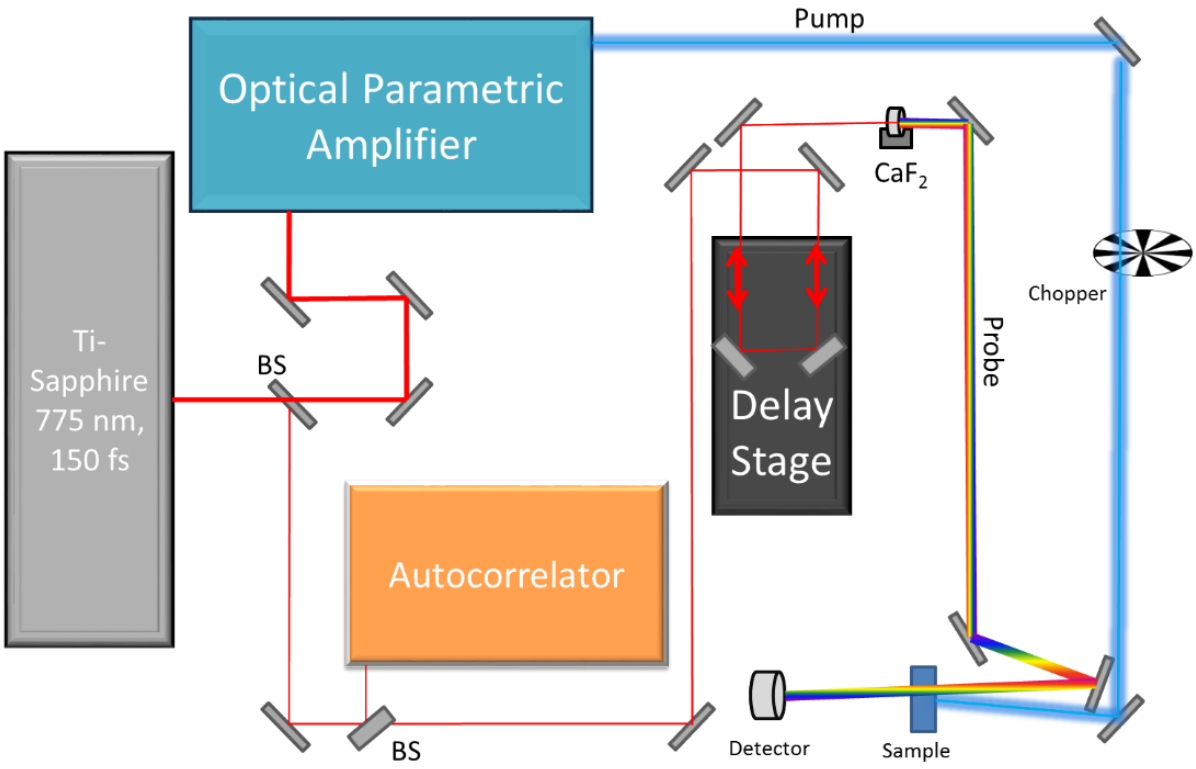

Figure 2.1. Simplified illustration of the femtosecond transient absorption experimental setup. BS = beamsplitter; CaF_2 = Calcium fluoride.

2.2. Optical Parametric Amplifier Description

In order to produce the visible pump wavelengths used in the fsTA experiments, the 775 nm output of our laser must be sent through a near-IR optical parametric amplifier (OPA) and one or two β-barium borate (BBO) crystals, depending on the desired wavelength. The OPA is a home-built system (Figure 2.3) based on a two crystal arrangement as described by Cerullo and De Silvestri.[1] The input pulse is sent through a 90:10 beamsplitter (BS1). The front reflection of BS1 (90% of the input beam) will be used as the amplifier beam in the second crystal for power-amplification. The unused portion is sent through another 90:10 beamsplitter (BS2) and used in the pre-amplifier pass.

Optical parametric amplification is a second-order nonlinear optical process that allows us to take our fixed CPA output at 775 nm and produce a tunable excitation pulse that is varied to meet our experimental needs. In our OPA, the 775 nm pulse is used as the high-powered, fixed frequency pump beam that transfers energy to a variable energy signal beam at lower powers. An even lower frequency idler beam is also generated to satisfy energy conservation laws, depending on the generated signal beam ($\hbar\omega_{pump} = \hbar\omega_{signal} + \hbar\omega_{idler}$, Figure 2.2). This process is similar to difference frequency generation (DFG) where interaction between two input beams creates a third lower frequency beam ($\hbar\omega_2 = \hbar\omega_3 - \hbar\omega_1$); however, in the DFG case, ω_3 and ω_1 are of similar intensities.[5]

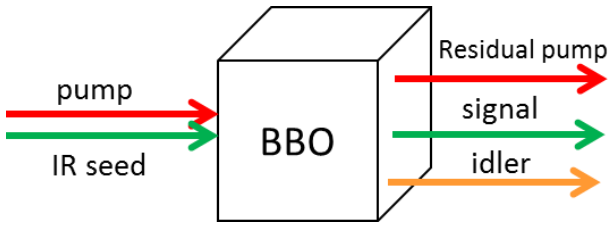

Figure 2.2. Illustration of optical parametric amplification.

Another requirement of successful amplification is satisfaction of the phase matching condition, where $\Delta k = k_{pump} + k_{signal} + k_{idler} = 0$. This ensures that the input waves are of the same phase along the propagation direction through the nonlinear crystal and maximizes the interaction between them. The phase matching can be tuned through changing crystal angles in the OPA to maximize amplification.

Prior to building the OPA shown in Figure 2.3, our experimental setup had a single-crystal arrangement where pre- and power- amplification steps occur within the same nonlinear crystal. This configuration complicated the alignment and tunability of the output wavelengths as the power output was very sensitive to the crystal angle. The two-crystal configuration in Figure 2.3 simplifies alignment and allows us to control the crystal angles separately. The crystal angles can be iterated to select the desired signal frequency in the pre-amplification pass and maximize power amplification in the second crystal (BBO2). The OPA displayed in Figure 2.3 expanded our wavelength range and significantly minimized alignment time.

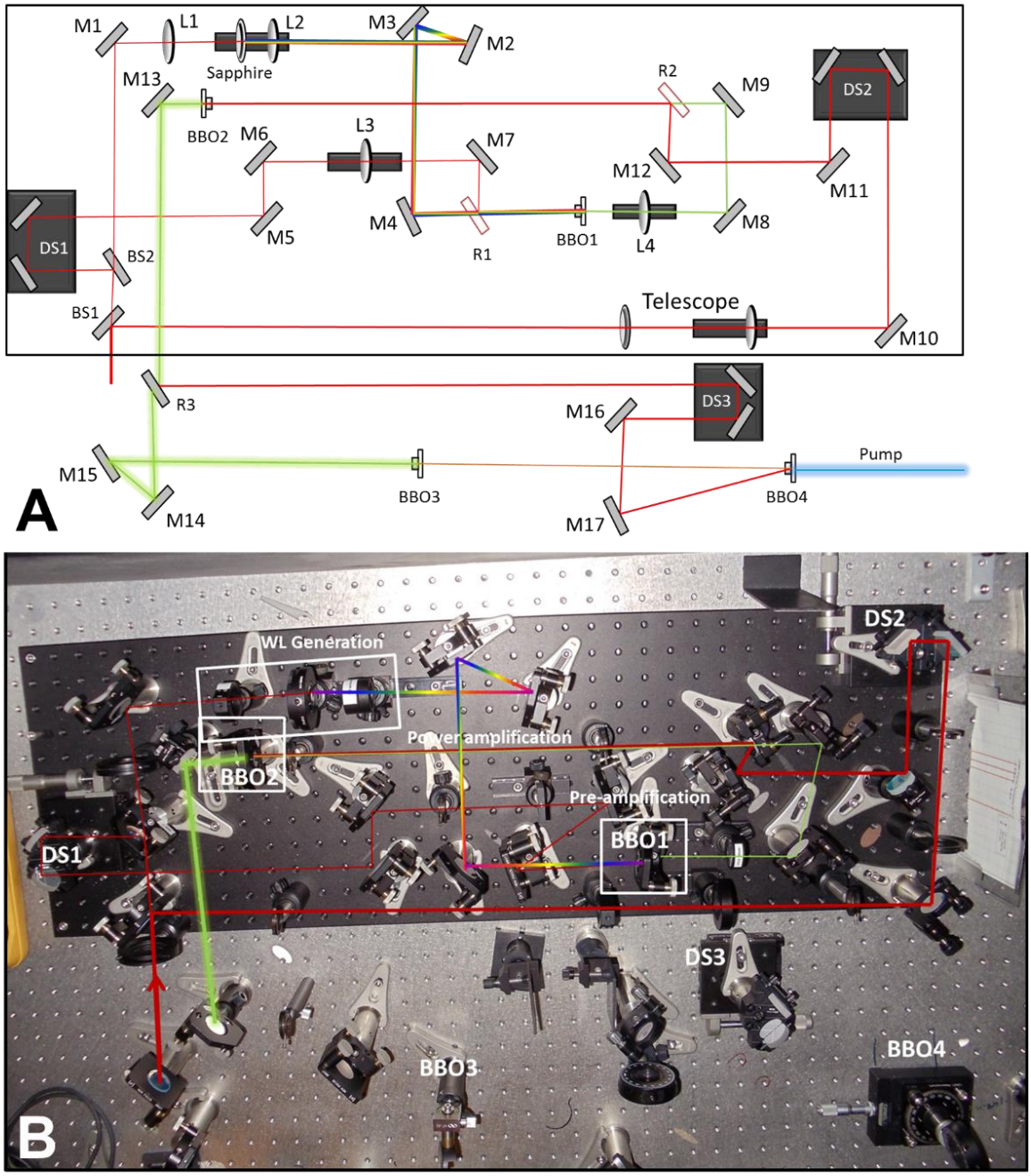

Figure 2.3. (A) Schematic of the home-built optical parametric amplifier. (B) Photograph of the home-built optical parametric amplifier with important components labeled. BS = beamsplitter; M = mirror; L = lens; R = 775 nm reflector; BBO = β-Barium Borate crystal; DS = delay stage; WL = white light.

2.2.1. Pre-Amplifier Pass.

The front reflection of BS2 (90% of the unused portion) is sent through an manual delay stage (DS1) and travels through M5 and M6 where it is focused through a 300 mm plano-convex lens on an optical rail to change the focus through BBO1. After this lens, the pump beam travels to M7 and reflects off of a 775 nm reflector (R1) into BBO1. The focus of this beam should be on the verge of generating continuum in BBO1. This works best when the beam reaches the focal point after BBO1. An iris before the lens attenuates the pulse power hitting the crystal.

The 10% of the pulse that passed through BS2 generates white light in a Sapphire window. The beam hits M1 and passes through a 75 mm plano-convex lens where it is focused into the Sapphire window and generates a white light (WL) continuum. The window is rotated and the beam is attenuated using an iris until this continuum is stable. This continuum passes through a 30 mm plano-convex achromatic lens and travels to M2, M3, and M4. After M4, the IR portion of the continuum passes through the 775 nm reflector to become the seed pulse. The IR seed and 775 nm pump pulse come together and travel collinearly into BBO1.

The temporal and spatial overlap is very important to producing the seed pulse for power amplification. Spatial overlap can be achieved visibly using M3 and M4 for the IR seed and M7 and R1 reflector to place these beams in the center of BBO1. The temporal overlap is adjusted using DS1. When this overlap is achieved, the lower intensity, lower frequency seed is amplified by the more intense, higher frequency pump beam. The amplified seed, known as the signal, is selected by the angle of the BBO1. The idler beam is generated due to energy conservation laws where $\omega_{idler}<\omega_{signal}<\omega_{pump}$. The efficiency of the pre-amplification pass is maximized by changing the focus of the pump/seed lenses and the iris attenuation of the pump pulse. When

maximum spatial and temporal overlap is achieved, we observe a flash of visible radiation due to the sum frequency mixing of the signal and pump beams.

2.2.2. Power Amplifier Pass.

After BBO1, the signal, idler and pump beams are collimated in a 775 nm plano-convex lens then guided through M8 and M9, where the signal and idler, the IR wavelengths, pass through another 775 nm reflector (R2). The unused pump is reflected into a beam dump. Simultaneously, the front reflection from BS1 is sent down a long path through a telescope to decrease and collimate the beam size, then reflected off M10 and into DS2. Here, the temporal overlap of this pump with the IR beams amplified in BBO1 can be maximized through BBO2. After DS2, the pump travels to M11 and M12 before meeting up with the pre-amplifier pass at the 2nd 775 nm reflector. The signal, idler, and pump beams travel collinearly through BBO2 where amplification of the signal and idler occurs. A similar flash appears in this pass that is maximized by adjusting spatial and temporal overlap.

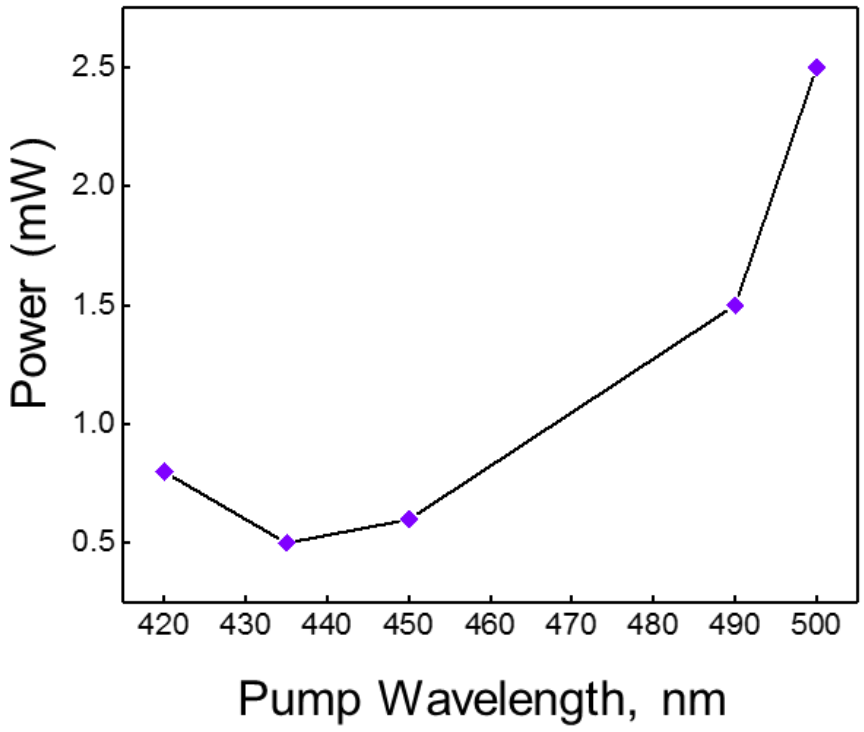

Figure 2.4. Maximum power (mW) for OPA-generated pump wavelengths.

2.2.3. fsTA Pump Generation.

To generate the visible pump pulse, the residual 775 nm is separated from the generated signal and idler pulses using a third 775 nm reflector (R3). The signal and idler pass through R3 and travel to BBO3 through M14 and M15. The residual 775 nm travels through DS3 and is directed into BBO4 via M17. Through changing crystal angles, and choosing beams to mix and match, we can create a variety of pump wavelengths ranging from 388 nm through 600 nm. A selection of wavelengths and their maximum powers are shown in Figure 2.3. To generate 388 nm, we simply frequency double the 775 nm output through second harmonic generation (SHG) in BBO4. For wavelengths, such as 420 nm, SHG of the idler (1800 nm to 900 nm) in BBO3 is mixed with residual 775 nm via sum frequency generation (SFG). In SFG, two pulse of different

frequencies are added together in a nonlinear crystal ($\hbar\omega_3 = \hbar\omega_1 + \hbar\omega_2$, Figure 2.5) in a process opposite that of DFG. For 490 nm, the signal output from the OPA (~1300 nm) is mixed with 775 nm in BBO4. We can also utilize the fourth harmonic of the idler to produce 450 nm in BBO4.

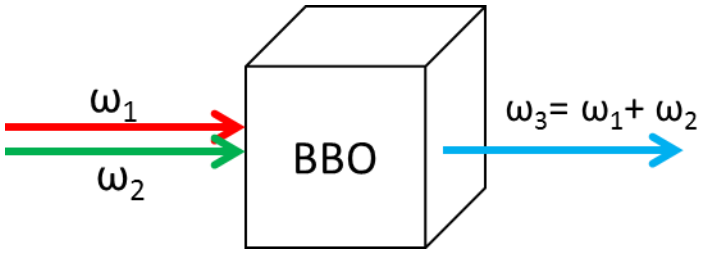

Figure 2.5. Illustration of Sum Frequency Generation in BBO4.

The excitation pulse tunability afforded through optical parametric amplification expands our capabilities to study the dynamics of a wide variety of systems from transition metal complexes to organic systems.

REFERENCES

1. Styers-Barnett, D. Ultrafast transient absorption spectroscopy investigations of excited state dynamics in SWNT/polymer composites and energy transfer between covalently appended components in $[Ru(dmb)^2(bpy\text{-}an)]^{2+}$. University of North Carolina, Chapel Hill, 2005.

2. Shaw, G. B. Dynamical evolution of the metal-to-ligand charge transfer excited states in polypyridyl Ru(II) and Os(II) complexes: an investigation by femtosecond transient absorption spectroscopy and polarization anisotropy. University of North Carolina, Chapel Hill, 2002.

3. Westlake, B. C. Ultrafast Investigation of Light-Driven Electron Proton Transfer in Intermolecular Model Systems. University of North Carolina, Chapel Hill, 2010.

4. Cerullo, G.; De Silvestri, S. Ultrafast Optical Parametric Amplifiers. *Rev. Sci. Instrum.* **2003**, *74* (1), 1-18.

5. Manzoni, C.; Cerullo, G. Design Criteria for Ultrafast Optical Parametric Amplifiers. *J. Opt.* 2016, *18* (10), 103501-103534.

Chapter 3: Ultrafast Recombination Dynamics in Dye-Sensitized SnO_2/TiO_2 Core/Shell Films

This chapter previously appeared as an article in the Journal of Physical Chemistry Letters. The original citation is: Gish, M. K.; Lapides, A. M.; Brennaman, M. K.; Templeton, J. L.; Meyer, T. J.; Papanikolas, J. M. *J. Phys Chem. Lett.* **2016**, *7*, 5297.

3.1. Introduction.

Dye-sensitized photoelectrosynthesis cells (DSPECs) combine the photon-harvesting and charge separation properties of dye-sensitized solar cells (DSSC) with molecular catalysis to convert sunlight into chemical fuels. Central to the DSPEC operation is a photoanode that consists of a molecular chromophore/catalyst assembly adsorbed onto a mesoporous metal oxide (MO_x) film. Together, these functional elements act to absorb solar photons, separate charge and use the photogenerated redox equivalents to drive the catalytic cycle for water oxidation through four separate photoactivation steps.[1-2] In the first photoactivation step, the photoexcited chromophore injects an electron into the conduction band (CB) of the semiconductor, and the newly formed oxidative equivalent is transferred to the catalyst, returning the chromophore to its ground state. While this initial step is fast, occurring within a few hundred picoseconds,[3-5] the latter steps, which include the O-O bond formation, take place on time scales ranging from microseconds to milliseconds.[2] These slow reaction steps place significant demands on the chromophore-semiconductor interface to maintain a long-lived charge separated state (CSS) between the oxidized dye and reduced semiconductor. Commonly used metal oxides (e.g. TiO_2, SnO_2) functionalized with Ru(II) dyes exhibit CSS lifetimes (~μs) adequate for efficient DSSC

operation,[6] but far too short to achieve water oxidation with catalysts whose turn-over frequencies are less than 10^3 s^{-1}.[2]

There are several strategies available to extend CSS lifetimes. Molecular-based approaches have shown modest success in increasing the lifetime of the CSS by moving the oxidative equivalent away from the surface.[7-10] However, the greatest improvements have been realized thus far with core/shell heterostructures.[11-16] For example, recombination is delayed significantly at the surfaces of SnO_2/TiO_2 core/shell nanoparticles formed by encasing a mesoporous SnO_2 film with a conformal shell of amorphous TiO_2 (*a*-TiO_2). The conduction band alignment between the two oxides in the resulting heterostructure serves to localize the injected electrons within the core material. Recombination of electrons in the core with oxidized dyes bound to the shell must occur by either surmounting the 0.4 eV energetic barrier introduced by the shell, or by tunneling through it. The resulting CSS state decays primarily by a tunneling mechanism, and exhibits lifetimes that approach a 1000-fold improvement over TiO_2 or SnO_2 alone.[17] Even though recombination is significantly slowed, DSPEC device efficiencies remain low.[15, 18]

We report here the interfacial electron transfer dynamics of nanocrystalline SnO_2/*a*-TiO_2 core/shell films sensitized with $[Ru^{II}(2,2'\text{-bpy})_2(4,4'\text{-}(PO_3H_2)_2\text{bpy})]^{2+}$ (**RuP**, Figure 3.1C, bpy = bipyridine). Our transient absorption experiments reveal that electron injection into the *a*-TiO_2 shell is fast (10s-100s ps), indicating that the poor device efficiencies are not the result of slow injection. Instead, kinetics measurements performed on time scales ranging from ps to ms suggest that the low efficiencies stem from a rapid recombination process involving the *a*-TiO_2 shell. A substantial fraction of the photoinjected electrons (~60%) recombine within a few hundred picoseconds after photoexcitation (τ~220 ps), presumably from sites near the oxidized

chromophore. The remaining electrons pass through the *a*-TiO_2 shell into the SnO_2 core, exhibiting recombination times that extend into the millisecond time regime.

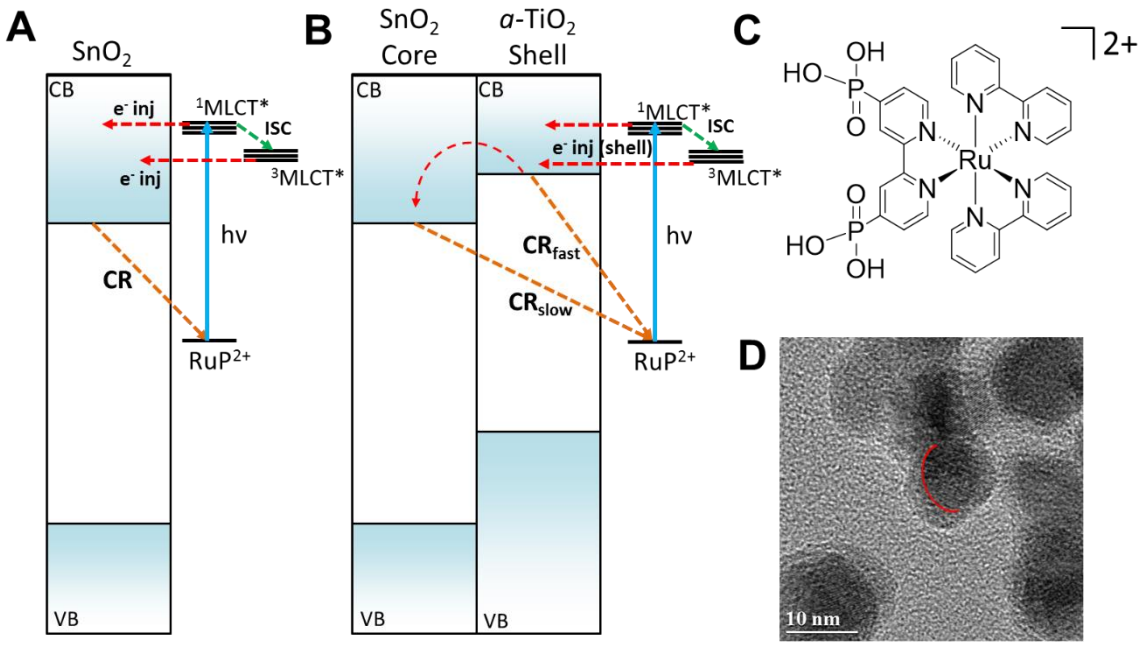

Figure 3.1. (A) Illustration of a band diagram describing the photoinduced processes for SnO_2|**RuP.** (B) Illustration of a band diagram describing the photoinduced processes for a core/shell photoanode (SnO_2/*a*-TiO_2|**RuP**). (C) Chemical structure of $[Ru^{II}(2,2'\text{-bpy})_2(4,4'\text{-}(PO_3H_2)_2bpy)]^{2+}$ (**RuP**). (D) TEM image of core/shell configuration of SnO_2/*a*-TiO_2 (1.3 nm). The interface between SnO_2 and *a*-TiO_2 is highlighted in red. CR = Charge Recombination; CB = Conduction Band; VB = Valence Band; ISC = Intersystem Crossing; MLCT = Metal-to-Ligand Charge Transfer; e^- inj = electron injection.

The SnO_2/*a*-TiO_2 films were obtained by growing a thin, conformal TiO_2 shell via atomic layer deposition (ALD) on top of 2 μm thick mesoporous SnO_2 (15-20 nm diameter particles) films through a series of successive reaction cycles of tetrakis(dimethylamido) titanium (TiTDMA) and H_2O. Shell thickness (Δ) was controlled by the number of ALD reaction cycles and varied between 1.3-2.3 nm. Transmission electron microscopy (TEM) confirmed the presence of a nanocrystalline SnO_2 core and a conformal *a*-TiO_2 shell (Figure 1D). The films were dye-loaded by immersion in a methanol solution (~1 mM dye) followed by soaking in pure methanol to remove unadsorbed dyes. Prior to transient absorption experiments, the films were submerged in 0.1 M $HClO_4$ aqueous solution and degassed with argon for 45 minutes. Under the acidic conditions, the phosphonate linkage to the metal oxide surface is stable and no detectable desorbed **RuP** dye is observed in the solution by UV/Vis spectroscopy following the transient experiments.

Transient absorption measurements were performed on time scales ranging from femtoseconds to milliseconds using a combination of instruments[3-4, 19] that access three different time regimes: 0-1 ns, 500 ps-400 μs, and 10 ns-10 ms. Femtosecond measurements utilized a 1 kHz Ti:sapphire chirped pulse amplifier (Clark-MXR CPA-2001) and optical parametric amplifier (OPA) with a broad-band white-light continuum probe. Measurements on the picosecond to microsecond time scale were accomplished using the same pump pulse as the femtosecond instrument, but the probe pulse was formed by continuum generation in a diode-laser-pumped, photonic crystal fiber and electronically delayed relative to the pump pulse. Access to millisecond time scales was achieved using a transient absorption apparatus based on a Q-switched nanosecond Nd:YAG and optical parametric oscillator (OPO) with a continuous arc-lamp probe. The energies of the excitation pulse in each instrument were adjusted to 1 mJ/cm^2.

Orientation effects were avoided by using a magic angle polarization configuration in the femtosecond instrument and depolarized probe light in ns-ms measurements.

3.2. Experimental Methods.

3.2.1. Materials and Molecular Synthesis.

Deionized water was further purified using a Milli-Q Ultrapure water purification system. Perchloric acid (99.999%) was purchased from Sigma-Aldrich and used as received. Nanoparticle films of tin oxide (SnO_2) were constructed according to literature procedures. [18,20] Thin shells of titanium dioxide (*a*-TiO_2) were deposited on SnO_2 using atomic layer deposition (ALD). The molecular chromophore, $[Ru^{II}(bpy)_2(4,4'\text{-}(PO_3H_2)_2bpy)]^{2+}[Cl]_2$ (**RuP**), was synthesized according to a literature procedure.[21-22] Dye-sensitization of electrodes for transient absorption spectroscopy were made by soaking the nanoparticle films in a methanol solution of **RuP** (~1 mM) in the dark overnight (~14 hours). After the soak period, the electrodes were rinsed with methanol and dried under a stream of air. The electrodes were stored in the dark.

3.2.2. Atomic Layer Deposition.

Atomic layer deposition (ALD) was performed using a Cambridge NanoTech Savannah S200 ALD system located in the Chapel Hill Analytical and Nanofabrication Lab (CHANL) cleanroom. The reaction chamber was set to 150 °C. The cylinder containing the TiO_2 precursor, tetrakis(dimethylamido)titanium(IV) (TiTDMA), was heated at 75 °C. The reaction chamber and the precursor cylinder were both heated at temperature for a minimum of 1 hour prior to use. Samples were added to the reaction chamber such that the nanoparticle film was near the center of the chamber and in-line with the precursor inlet and outlet ports. Samples were placed under dynamic vacuum with a continuous nitrogen purge (99.999%, further purified using an Entegris GateKeeper Inert Gas Purifier) at temperature (150 °C) for a minimum of 10 minutes prior to

deposition. Deposition was performed in “exposure mode” in which the chamber containing precursor is isolated from vacuum. For a typical deposition cycle, TiTDMA was pulsed for 2 seconds, isolated in the chamber for 20 seconds, and purged from the chamber for 60 seconds. Water was introduced under identical conditions except a 20-ms pulse was used. One cycle consisted of TiTDMA followed by water, and the number of cycles was used to control the thickness of the deposited layer. Thickness of the deposited oxide layer was quantified by performing ellipsometry (J. A. Woollam Variable Angle Spectroscopic Ellipsometer; located in CHANL) on a piece of planar, witness Si present in the reactor during ALD on the nanoparticle films.

3.2.3. UV-Visible Absorption.

UV-Visible absorption spectra were collected using a UV-Visible-NIR absorption spectrophotometer (Agilent Technologies, model 8453A) operated with tungsten and deuterium lamps lit. Air was used as the baseline and samples were placed perpendicular to the beam path. An integration time of 0.5 s was used.

3.2.4. Sample Preparation for TA.

Samples for transient absorption were prepared by submerging films into 0.1 M $HClO_4$ aqueous solutions in 10 mm path length cuvettes at a 45° angle. The cuvette was fitted with an O-ring seal and Kontes valve inlet to purge the sample with argon for at least 45 min prior to TA measurements.

3.2.5. Femtosecond Transient Absorption.

Femtosecond transient absorption (fsTA) measurements were taken in a pump-probe configuration using a 1 kHz Ti:Sapphire, chirped pulse amplifier (Clark-MXR CPA-2001). The 425 nm pump pulse was produced through sum-frequency generation of a portion of the 775 nm

regenerative amplifier output and the 940 nm frequency doubled output of a home-built Optical Parametric Amplifier (OPA). The 480 nm pump pulse was generated using the same OPA through mixing 775 nm and the generated signal (~1200 nm) beam. The pump beam was chopped at 500 Hz and a power of 100 nJ/pulse was used. The white light probe has a spectral range of 340-800 nm and is generated by focusing a portion of the 775 nm output into a CaF_2 window that was continuously translating. The probe polarization is set to horizontal and the pump is set to ~54.7° (magic angle) relative to the probe. A computer-controlled optical delay line was used to delay the probe pulse relative to the pump. Pump and probe beams were focused to ~150 μm and spatially overlapped at the sample. Pulse-to-pulse changes in the probe beam via pump excitation were collected using a fiber optic-coupled multichannel spectrometer with a CMOS sensor. The sample is raster scanned throughout the experiment. The instrument response is ~250 fs and the sensitivity of the detector is 0.1 mOD.

3.2.6. Nanosecond-Microsecond Transient Absorption (1 nsec-400 μs).

Nanosecond pump-probe transient absorption measurements were taken with the same pump pulse as fsTA. The probe pulse was created through continuum generation in a diode-laser pumped photonic crystal fiber and electronically delayed relative to the pump pulse with a 500 ps time resolution.

3.2.7. Nanosecond-Millisecond Transient Absorption (10 ns-10 ms).

Transient absorption measurements from 10 ns to 10 ms were carried out by using an Edinburgh Instruments, Inc., model LP920 laser flash photolysis instrument. Nanosecond laser pulses were provided by a pulsed Nd:YAG (5-7 ns FWHM; Spectra-Physics model Quanta-Ray LAB-170-10) / OPO (VersaScan-MB) laser combination tuned to 1 mJ, 480 nm laser pulses at 1 Hz. Experiment timing was PC-controlled via Edinburgh software (L900). The white light

output of a 450W Xe lamp was focused, passed through two 380 nm, long pass color filters, and overlapped with the laser pulse within the photoanode films. Once through the sample, the probe beam passed through a color filter to reject laser scatter into a monochromator (bandwidth < 5 nm), and was detected by a Hamamatsu R928 photomultiplier tube (PMT) in a non-cooled housing. The instrument response was found to be ~10 ns FWHM. Kinetic data were the result of averaging 25-200 sequences of pump, probe, and pump-probe. Transient data were analyzed using Origin Pro 2015 (OriginLab, Inc.), or L900 v7 (Edinburgh, Inc.) software. Data were collected at room temperature (22 ± 2 °C).

3.2.8. Overlaying Kinetics from Different TA Measurements.

Comparing of transient absorption results collected using ns and fs laser pulse was made possible by performing transient absorption measurements at the same photon excitation flux. Repeated experiments demonstrated the reproducibility of the kinetic measurements from each experimental setup. Kinetic traces were normalized to the same time points for each instrument and smoothed using a 3-pt moving average.

3.3. Results and Discussion.

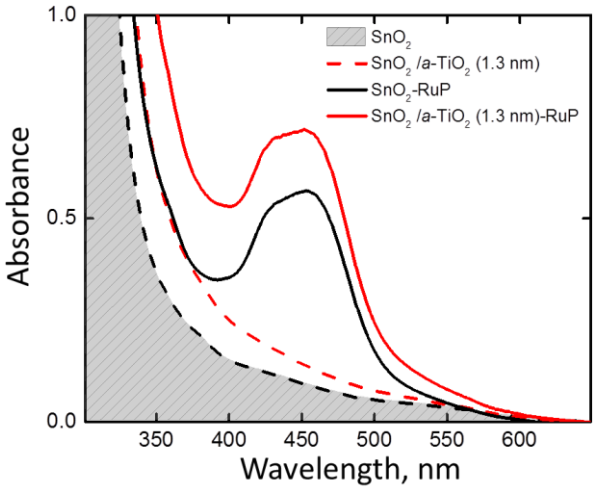

Figure 3.2. UV-Visible Absorption Spectra of bare films of SnO_2, SnO_2/a-TiO_2 (1.3 nm), and dye-sensitized slides SnO_2|**RuP** and SnO_2/a-TiO_2 (1.3 nm)|**RuP** in deaerated 0.1 M $HClO_4$ (aq).

Although Figure 3.1 depicts the *a*-TiO_2 shell grown by ALD as having well-defined band structure, this is most likely an over-simplification. Steady state absorption spectra of the bare SnO_2 and SnO_2/*a*-TiO_2 films suggest that, unlike nanocrystalline TiO_2, which is transparent for λ>400 nm, the *a*-TiO_2 layer has a low energy absorption out to ~500 nm (Fig. 3.2). This absorption is likely the result of a large defect density in the *a*-TiO_2 layer that gives rise to localized states within the band gap.[23]

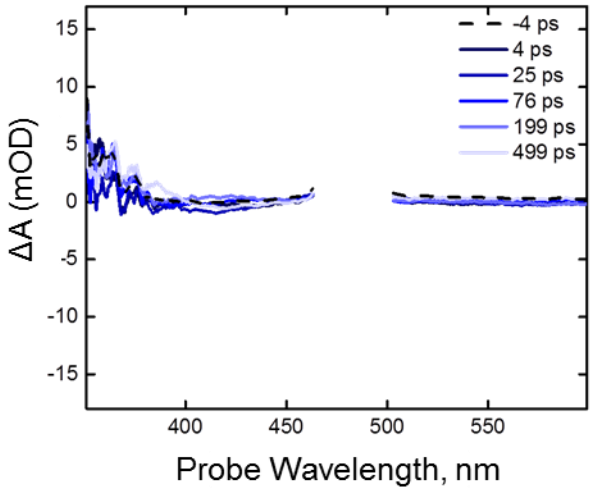

Figure 3.3. fsTA spectra of bare SnO_2/*a*-TiO_2(1.3 nm) in deaerated 0.1 M $HClO_4$ (aq) excited at 480 nm (100 nJ/pulse).

Photoexcitation of the **RuP** complex between 400-500 nm promotes an electron from the Ru center to one of the polypyridyl ligands, forming a metal-to-ligand charge transfer (MLCT) state. The SnO_2|**RuP** films were excited at 425 nm, near the MLCT absorption maximum. The SnO_2/*a*-TiO_2|**RuP** films, on the other hand, were excited at 480 nm to minimize direct excitation of the *a*-TiO_2 shell. Transient absorption experiments on undyed SnO_2/*a*-TiO_2 films photoexcited at 480 nm do not exhibit transient spectral features (Fig. 3.3), implying that band-gap excitation of the *a*-TiO_2 shell does not contribute to the TA spectra of the sensitized films. Furthermore, photoexcitation of SnO_2|**RuP** at 425 nm and 480 nm show no differences in the transient absorption spectra, or kinetics, indicating the excited state dynamics are insensitive to the choice of excitation wavelength (Fig. 3.4).

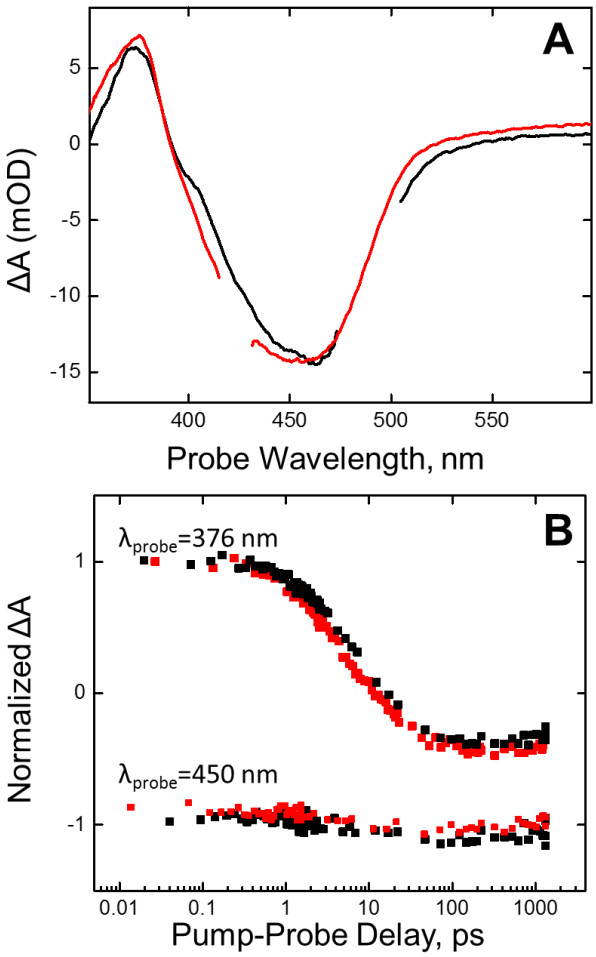

Figure 3.4. (A) Transient absorption spectra of SnO_2|**RuP** in deaerated 0.1 M $HClO_4$ (aq) 1 ps after excitation at 425 nm (red) and 480 nm (black) (100 nJ/pulse) (B) Normalized transient absorption kinetics of SnO_2|**RuP** for ESA (λ_{probe} = 376 nm) and GSB (λ_{probe} = 450 nm) in deaerated 0.1 M $HClO_4$ (aq) excited at 425 nm (red traces) 480 nm (black traces) (100 nJ/pulse).

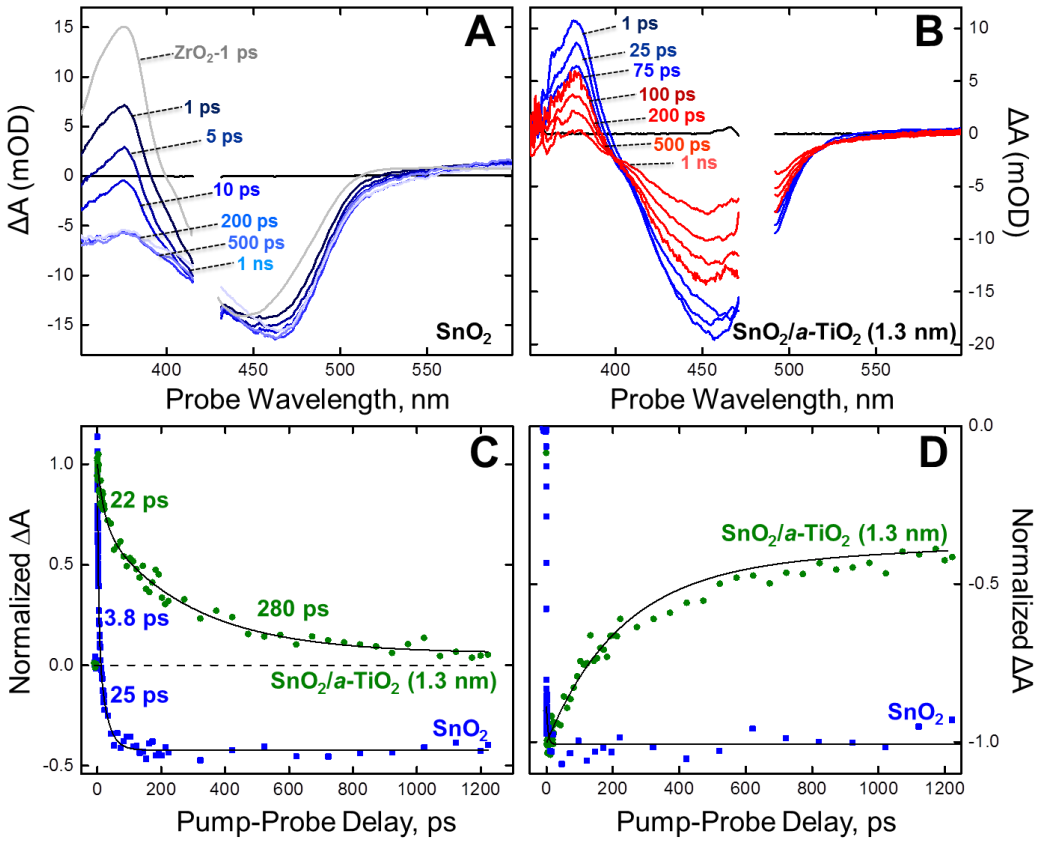

Figure 3.5. (A) Transient absorption spectra of SnO_2|**RuP** in deaerated 0.1 $HClO_4$ (aq) at 1 ps (dark blue), 5 ps, 10 ps, 200 ps, 500 ps, 1 ns (light blue) after 425 nm laser excitation. The spectrum in grey is the 1 ps transient absorption spectrum of ZrO_2|**RuP** after 425 nm excitation and is scaled to the GSB of the SnO_2|**RuP** at 1 ps. (B) Transient absorption spectra of SnO_2/*a*-TiO_2 (1.3 nm)|**RuP** in deaerated 0.1 $HClO_4$ (aq) at 1 ps, 25 ps, 75 ps, 100 ps, 200 ps, 500 ps, 1 ns after 480 nm excitation with spectra ≤ 75 ps in blue and ≥ 100 ps in red. (C) Normalized transient absorption kinetics for SnO_2|**RuP** (blue) and SnO_2/*a*-TiO_2 (1.3 nm)|**RuP** (green) at 376 nm. Biexponential fits are shown as solid lines with results in Table 1. (D) Normalized transient absorption kinetics for SnO_2|**RuP** (blue) at 450 nm and SnO_2/*a*-TiO_2 (1.3 nm)|**RuP** (green) at 430 nm. Fits are shown as solid lines.

The transient absorption spectra of **RuP** on SnO_2 at early times are similar to those observed for many Ru(II) dyes exhibiting the characteristic excited state absorption (ESA) in the near UV that arises from a π-π* transition on the reduced ligand (Fig. 3.5A).[24] Decay of this excited state feature without loss of the ground state bleach (GSB) amplitude is a signature of electron injection.[2-5, 24] A qualitative estimation of the injection efficiency can be made from analysis of the relative amplitudes of the transient spectral features. Based on intensities of the ESA on SnO_2 compared to ZrO_2 (Fig. 3.5A, grey), where no charge injection occurs (Fig. 3.6), we estimate that ~35% of the **RuP*** undergo electron injection within the instrument response. Furthermore, the complete disappearance of this band (Fig. 5A), along with kinetic analysis of the decay (Fig. 3.5C, blue), indicate injection from the remaining 65% of the **RuP*** occurs on multiple time scales (τ_1=3.8 ps, τ_2=25 ps) with nearly unit efficiency. These time scales are consistent with previous observations from similar Ru dyes on SnO_2,[25-29] and about a factor of two shorter than on TiO_2.[24]

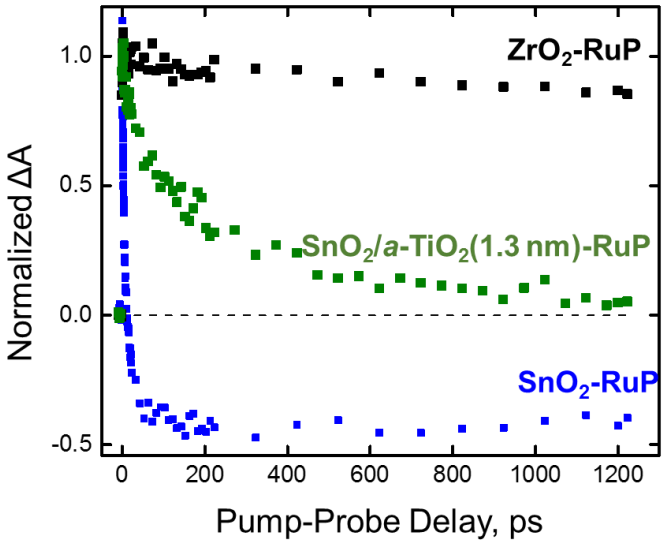

Figure 3.6. Normalized transient absorption kinetics of ZrO_2|**RuP** (black), SnO_2/*a*-TiO_2(1.3 nm)|**RuP** (green), and SnO_2|**RuP** (blue) (λ_{probe} = 376 nm) in deaerated 0.1 M $HClO_4$ (aq) excited at 480 nm a (100 nJ/pulse).

The spectral evolution following femtosecond excitation of **RuP** on the core/shell heterostructures is notably different from the SnO_2 case (Fig 3.5B). We do observe both the ESA and GSB for **RuP** adsorbed onto core/shell particles (Δ=1.3 nm), and during the first 75 ps, the ESA decays with no loss of the GSB (Fig. 3.5B, blue spectra), similar to SnO_2|**RuP**. However, for longer pump-probe delays, the GSB decays together with the ESA (Fig. 3.5B, red spectra), in contrast to what is observed on SnO_2. Kinetic analysis shows that the ESA is lost with both fast (τ=22 ps) and slow (τ=280 ps) time components (Fig 3.5C). We attribute the fast component to electron injection into the *a*-TiO_2 shell, consistent with observations made via time-resolved terahertz spectroscopy (TRTS).[30-31] Electron injection rates are independent of shell thickness (Eq. 3.1, Table 3.1) suggesting that the electron is injected into the *a*-TiO_2 shell and does not tunnel through the shell to the SnO_2 core.

$$y = Offset + A_1 e^{-x/\tau_1} + A_2 e^{-x/\tau_2} \quad (3.1)$$

Table 3.1. Results of biexponential fits for loss of ESA (λ_{probe} = 376 nm).

	Offset	**A_1**	**A_2**	**τ_1, ps**	**τ_2, ps**
SnO_2	-0.4	59%	41%	3.8	25
SnO_2/*a*-TiO_2 (1.3 nm)	-0.06	32%	67%	22	280
SnO_2/*a*-TiO_2 (1.8 nm)	-0.008	40%	60%	28	299
SnO_2/*a*-TiO_2 (2.0 nm)	0.08	36%	64%	23	249
SnO_2/*a*-TiO_2 (2.3 nm)	-0.07	55%	45%	18	312

The slower component coincides with a rapid decay component of the GSB (τ=220 ps) that represents ~60% loss of the total GSB signal amplitude (Fig. 3.5D). The ultrafast decay of both the GSB and ESA features is unique to the core/shell system and is not observed in SnO_2|**RuP** or TiO_2|**RuP**. The ~220 ps time constant is much shorter than the lifetime of the MLCT state (τ ~ 450 ns),[2-5, 24] indicating that this decay component is not the result of excited state relaxation. A similar ultrafast recombination component (τ = 218 ps) is observed for ALD grown TiO_2 on ZrO_2 (i.e. ZrO_2/*a*-TiO_2|**RuP**), where the injected electrons must remain in the shell (Fig. 3.7). We note that while both SnO_2/*a*-TiO_2 and ZrO_2/*a*-TiO_2 exhibit the same fast time components, the ultrafast recombination in the ZrO_2 case represents just 30% of the total decay, suggesting that the microscopic structure, and perhaps defect density, of the TiO_2 grown by ALD is affected by the underlying substrate (e.g. SnO_2 vs ZrO_2). The amplitude and time constants associated with this fast recombination process are independent of shell thickness (Fig. 3.8A), implying that it involves localized states in the *a*-TiO_2 layer near the oxidized dye. Based on the similarity in time scales for the loss of the ESA and GSB, we attribute this kinetic component to slow injection into the shell followed by rapid interfacial electron transfer to reform the Ru(II) ground state. The fast time scale (220-280 ps) suggests this process involves either the injected electron (i.e. geminate recombination), or occurs through non-geminate electron transfer from filled mid gap states that result from the high defect density of the amorphous TiO_2 shell.[23] Regardless of

its origin, the presence of this ultrafast loss pathway underscores the functional differences between ALD-grown TiO_2 shells and nanocrystalline TiO_2 in DSSC and DSPEC devices.

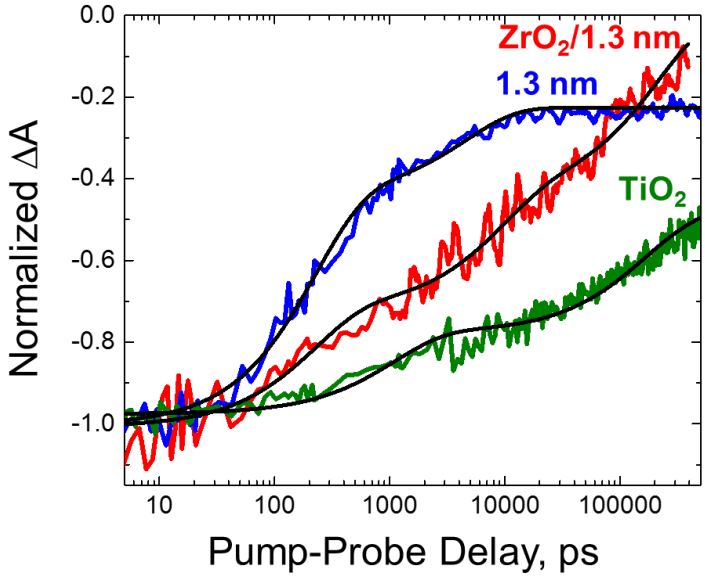

Figure 3.7. Normalized transient absorption kinetics of SnO_2/*a*-TiO_2(1.3 nm)|**RuP** (blue), ZrO_2/*a*-TiO_2(1.3 nm)|**RuP** (red), TiO_2|**RuP** (green) (λ_{probe} = 430 nm) in deaerated 0.1 M $HClO_4$ (aq) excited at 480 nm.

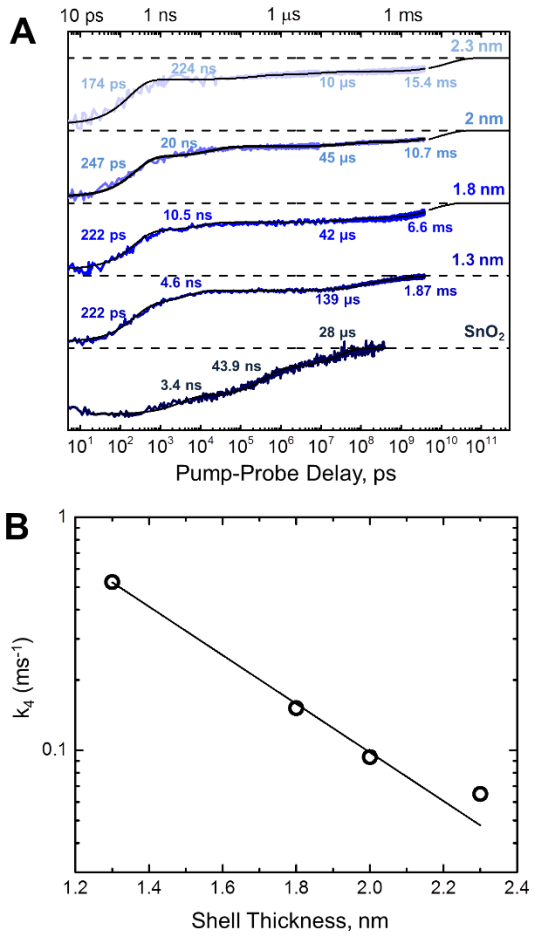

Figure 3.8. (A) Transient absorption kinetics over 10 decades of time for SnO_2|**RuP** (darker blue), SnO_2/*a*-TiO_2 (1.3 nm)|**RuP** (dark blue), SnO_2/*a*-TiO_2 (1.8 nm)|**RuP** (blue), SnO_2/*a*-TiO_2 (2.0 nm)|**RuP** (light blue) and SnO_2/*a*-TiO_2 (2.3 nm)|**RuP** (lighter blue) at a probe wavelength of 430 nm. Kinetic traces have been offset for clarity. Each transient is fit to a quad-exponential, which are shown as black solid lines. Fits have been extended to illustrate the complete decay of the signal to zero intensity. The fit extension is to demonstrate the amount of signal left at our last observation point and is not meant to imply that there is no other physical process occurring beyond our observation window. Amplitudes and time constants are summarized in Table 3.2. (B) Plot of the slowest time component ($k_4 = 1/\tau_4$) vs thickness of the *a*-TiO_2 shell.

$$y = A_1 e^{-x/\tau_1} + A_2 e^{-x/\tau_2} + A_3 e^{-x/\tau_3} + A_4 e^{-x/\tau_4} \quad (3.2)$$

Table 3.2. Results of multiexponential fits for GSB recovery (λ_{probe} = 430 nm).

	A_1	A_2	A_3	A_4	τ_1	τ_2	τ_3	τ_4
SnO_2	27%	42%	30%		3.4 ns	44 ns	28 μs	
SnO_2/*a*-TiO_2 (1.3 nm)	56%	22%	14%	8%	222 ps	4.6 ns	139 μs	1.87 ms
SnO_2/*a*-TiO_2 (1.8 nm)	57%	13%	6%	24%	222 ps	10.5 ns	42 μs	6.6 ms
SnO_2/*a*-TiO_2 (2.0 nm)	60%	15%	7%	18%	247 ps	20 ns	45 μs	10.7 ms
SnO_2/*a*-TiO_2 (2.3 nm)	67%	7%	5%	21%	174 ps	225 ns	10 μs	15.4 ms
ZrO_2/*a*-TiO_2 (1.3 nm)	29%	28%	43%		218 ps	8.9 ns	213 ns	

The oxidized chromophores remaining at 1 ns recombine with injected electrons on multiple timescales, ranging from a few nanoseconds to milliseconds (Fig. 3.8A).The ns-μs time constants are similar to those observed in other metal oxides[32] and likely corresponds to a transport-limited mechanism in which the injected electron hops from one discrete site in the *a*-TiO_2 shell to another before recombination with the oxidized dye. The presence of both the ultrafast and slower ns-μs recombination times suggest significant spatial variation in the quality of the *a*-TiO_2 layer. Regions with a high defect density give rise to the ps recombination, while other portions of the layer have a quality that is comparable to nanocrystalline TiO_2, resulting in the ns-μs recombination. The longest time component exceeds that observed on either SnO_2 or TiO_2 by two orders of magnitude (τ = 1.87-15.4 ms).[2, 32] This rate exponentially decreases with increasing shell thickness (Fig. 3.8B), suggesting that this millisecond component corresponds to tunneling recombination between electrons residing in the SnO_2 core and oxidized dyes at the shell surface.[17, 33]

3.4. Conclusions.

The interfacial dynamics of a series of dye-sensitized SnO_2/TiO_2 core/shell films with varying shell thickness were investigated from femtoseconds through milliseconds. Electron injection from the chromophore into the TiO_2 shell occurs within a few picoseconds after photoexcitation. Loss of the oxidized dye through recombination occurs across time scales spanning 10 decades of time. The majority (60%) of charge recombination events occur shortly after injection with a time constant of 220 ps, while a small fraction ($\leq$ 20%) persists for milliseconds. The lifetime of long-lived CSSs depends exponentially on shell thickness, suggesting that the injected electrons reside in the SnO_2 core and must tunnel through the TiO_2 shell to recombine with oxidized dyes.

The formation of a CSS with a millisecond lifetime is sufficient for water oxidation, and in this respect the core/shell architecture is successful. However, the fraction of oxidized chromophores persisting into the millisecond time regime is only about 20%. The loss of over 60% of the oxidized chromophores within the first nanosecond may be the origin of the low water oxidation efficiencies observed in DSPEC devices even with core/shell photoanodes.

REFERENCES

1. Concepcion, J. J.; House, R. L.; Papanikolas, J. M.; Meyer, T. J. Chemical Approaches to Artificial Photosynthesis. Proc. Natl. Acad. Sci. U. S. A. 2012, 109 (39), 15560-15564.

2. Ashford, D. L.; Gish, M. K.; Vannucci, A. K.; Brennaman, M. K.; Templeton, J. L.; Papanikolas, J. M.; Meyer, T. J. Molecular Chromophore-Catalyst Assemblies for Solar Fuel Applications. Chem. Rev. 2015, 115 (23), 13006-13049.

3. Bettis, S. E.; Hanson, K.; Wang, L.; Gish, M. K.; Concepcion, J. J.; Fang, Z.; Meyer, T. J.; Papanikolas, J. M. Photophysical Characterization of a Chromophore/Water Oxidation Catalyst Containing a Layer-by-Layer Assembly on Nanocrystalline TiO2 using Ultrafast Spectroscopy. J. Phys. Chem. A 2014, 118 (45), 10301-10308.

4. Bettis, S. E.; Ryan, D. M.; Gish, M. K.; Alibabaei, L.; Meyer, T. J.; Waters, M. L.; Papanikolas, J. M. Photophysical Characterization of a Helical Peptide Chromophore-Water Oxidation Catalyst Assembly on a Semiconductor Surface using Ultrafast Spectroscopy. J. Phys. Chem. C 2014, 118 (12), 6029-6037.

5. Wang, L.; Ashford, D. L.; Thompson, D. W.; Meyer, T. J.; Papanikolas, J. M. Watching Photoactivation in a Ru(II) Chromophore-Catalyst Assembly on TiO2 by Ultrafast Spectroscopy. J. Phys. Chem. C 2013, 117 (46), 24250-24258.

6. Ardo, S.; Meyer, G. J. Photodriven Heterogeneous Charge Transfer with Transition-Metal Compounds Anchored to TiO2 Semiconductor Surfaces. Chem Soc Rev 2009, 38 (1), 115-164.

7. Wilger, D. J.; Bettis, S. E.; Materese, C. K.; Minakova, M.; Papoian, G. A.; Papanikolas, J. M.; Waters, M. L. Tunable Energy Transfer Rates via Control of Primary, Secondary, and Tertiary Structure of a Coiled Coil Peptide Scaffold. Inorg. Chem. 2012, 51 (21), 11324-11338.

8. Springer, J. W.; Parkes-Loach, P. S.; Reddy, K. R.; Krayer, M.; Jiao, J. Y.; Lee, G. M.; Niedzwiedzki, D. M.; Harris, M. A.; Kirmaier, C.; Bocian, D. F., et al. Biohybrid Photosynthetic Antenna Complexes for Enhanced Light-Harvesting. J. Am. Chem. Soc. 2012, 134 (10), 4589-4599.

9. Trammell, S. A.; Moss, J. A.; Yang, J. C.; Nakhle, B. M.; Slate, C. A.; Odobel, F.; Sykora, M.; Erickson, B. W.; Meyer, T. J. Sensitization of TiO2 by Phosphonate-Derivatized Proline Assemblies. Inorg. Chem. 1999, 38 (16), 3665-3669.

10. Ma, D.; Bettis, S. E.; Hanson, K.; Minakova, M.; Alibabaei, L.; Fondrie, W.; Ryan, D. M.; Papoian, G. A.; Meyer, T. J.; Waters, M. L., et al. Interfacial Energy Conversion in Ru(II) Polypyridyl-Derivatized Oligoproline Assemblies on TiO2. J. Am. Chem. Soc. 2013, 135 (14), 5250-5253.

11. Palomares, E.; Clifford, J. N.; Haque, S. A.; Lutz, T.; Durrant, J. R. Control of Charge Recombination Dynamics in Dye Sensitized Solar Cells by the Use of Conformally Deposited Metal Oxide Blocking Layers. J. Am. Chem. Soc. 2003, 125 (2), 475-482.

12. Palomares, E.; Clifford, J. N.; Haque, S. A.; Lutz, T.; Durrant, J. R. Slow Charge Recombination in Dye-Sensitised Solar Cells (DSSC) using Al2O3 Coated Nanoporous TiO2 Films. Chem. Commun. 2002, (14), 1464-1465.

13. Kapilashrami, M.; Zhang, Y. F.; Liu, Y. S.; Hagfeldt, A.; Guo, J. H. Probing the Optical Property and Electronic Structure of TiO2 Nanomaterials for Renewable Energy Applications. Chem. Rev. 2014, 114 (19), 9662-9707.

14. Alibabaei, L.; Brennaman, M. K.; Norris, M. R.; Kalanyan, B.; Song, W. J.; Losego, M. D.; Concepcion, J. J.; Binstead, R. A.; Parsons, G. N.; Meyer, T. J. Solar Water Splitting in a Molecular Photoelectrochemical Cell. Proc. Natl. Acad. Sci. U. S. A. 2013, 110 (50), 20008-20013.

15. Alibabaei, L.; Sherman, B. D.; Norris, M. R.; Brennaman, M. K.; Meyer, T. J. Visible Photoelectrochemical Water Splitting into H2 and O2 in a Dye-Sensitized Photoelectrosynthesis Cell. Proc. Natl. Acad. Sci. U. S. A. 2015, 112 (19), 5899-5902.

16. Karlsson, M.; Jogi, I.; Eriksson, S. K.; Rensmo, H.; Boman, M.; Boschloo, G.; Hagfeldt, A. Dye-Sensitized Solar Cells Employing a SnO2-TiO2 Core-shell Structure Made by Atomic Layer Deposition. Chimia 2013, 67 (3), 142-148.

17. Knauf, R. R.; Kalanyan, B.; Parsons, G. N.; Dempsey, J. L. Charge Recombination Dynamics in Sensitized SnO2/TiO2 Core/Shell Photoanodes. J. Phys. Chem. C 2015, 119 (51), 28353-28360.

18. Sherman, B. D.; Ashford, D. L.; Lapides, A. M.; Sheridan, M. V.; Wee, K. R.; Meyer, T. J. Light-Driven Water Splitting with a Molecular Electroassembly-Based Core/Shell Photoanode. J. Phys. Chem. Lett. 2015, 6 (16), 3213-3217.

19. Hanson, K.; Brennaman, M. K.; Ito, A.; Luo, H. L.; Song, W. J.; Parker, K. A.; Ghosh, R.; Norris, M. R.; Glasson, C. R. K.; Concepcion, J. J., et al. Structure-Property Relationships in Phosphonate-Derivatized, RuII Polypyridyl Dyes on Metal Oxide Surfaces in an Aqueous Environment. J. Phys. Chem. C 2012, 116 (28), 14837-14847.

20. Green, A. N. M.; Palomares, E.; Haque, S. A.; Kroon, J. M.; Durrant, J. R. Charge Transport Versus Recombination in Dye-Sensitized Solar Cells Employing Nanocrystalline TiO2 and SnO2 Films. J. Phys. Chem. B 2005, 109 (25), 12525-12533.

21. Norris, M. R.; Concepcion, J. J.; Glasson, C. R. K.; Fang, Z.; Lapides, A. M.; Ashford, D. L.; Templeton, J. L.; Meyer, T. J. Synthesis of Phosphonic Acid Derivatized Bipyridine Ligands and Their Ruthenium Complexes. Inorg. Chem. 2013, 52 (21), 12492-12501.

22. Lapides, A. M.; Ashford, D. L.; Hanson, K.; Torelli, D. A.; Templeton, J. L.; Meyer, T. J. Stabilization of a Ruthenium(II) Polypyridyl Dye on Nanocrystalline TiO2 by an Electropolymerized Overlayer. J. Am. Chem. Soc. 2013, 135 (41), 15450-15458.

23. Hu, S.; Shaner, M. R.; Beardslee, J. A.; Lichterman, M.; Brunschwig, B. S.; Lewis, N. S. Amorphous TiO2 Coatings Stabilize Si, GaAs, and GaP Photoanodes for Efficient Water Oxidation. Science 2014, 344 (6187), 1005-1009.

24. Zigler, D. F.; Morseth, Z. A.; Wang, L.; Ashford, D. L.; Brennaman, M. K.; Grumstrup, E. M.; Brigham, E. C.; Gish, M. K.; Dillon, R. J.; Alibabaei, L., et al. Disentangling the Physical Processes Responsible for the Kinetic Complexity in Interfacial Electron Transfer of Excited Ru(II) Polypyridyl Dyes on TiO2. J. Am. Chem. Soc. 2016, 138 (13), 4426-4438.

25. Ai, X.; Anderson, N. A.; Guo, J. C.; Lian, T. Q. Electron Injection Dynamics of Ru Polypyridyl Complexes on SnO2 Nanocrystalline Thin Films. J. Phys. Chem. B 2005, 109 (15), 7088-7094.

26. Benko, G.; Myllyperkio, P.; Pan, J.; Yartsev, A. P.; Sundstrom, V. Photoinduced Electron Injection from Ru(dcbpy)2(NCS)2 to SnO2 and TiO2 Nanocrystalline Films. J. Am. Chem. Soc. 2003, 125 (5), 1118-1119.

27. Bauer, C.; Boschloo, G.; Mukhtar, E.; Hagfeldt, A. Ultrafast Studies of Electron Injection in Ru Dye Sensitized SnO2 Nanocrystalline Thin Film. Int. J. Photoenergy 2002, 4 (1), 17-20.

28. Tiwana, P.; Docampo, P.; Johnston, M. B.; Snaith, H. J.; Herz, L. M. Electron Mobility and Injection Dynamics in Mesoporous ZnO, SnO2, and TiO2 Films Used in Dye-Sensitized Solar Cells. ACS Nano 2011, 5 (6), 5158-5166.

29. She, C. X.; Guo, J. C.; Irle, S.; Morokuma, K.; Mohler, D. L.; Zabri, H.; Odobel, F.; Youm, K. T.; Liu, F.; Hupp, J. T., et al. Comparison of Interfacial Electron Transfer through Carboxylate and Phosphonate Anchoring Groups. J. Phys. Chem. A 2007, 111 (29), 6832-6842.

30. Swierk, J. R.; McCool, N. S.; Nemes, C. T.; Mallouk, T. E.; Schmuttenmaer, C. A. Ultrafast Electron Injection Dynamics of Photoanodes for Water-Splitting Dye-Sensitized Photoelectrochemical Cells. J. Phys. Chem. C 2016, 120 (11), 5940-5948.

31. McCool, N. S. S., J. R.; Nemes, C. T.; Schmuttenmaer, C. A.; Mallouk, T. E. Dynamics of Electron Injection in SnO2/TiO2 Core/Shell Electrodes for Water-Splitting Dye-Sensitized Photoelectrochemical Cells. J. Phys. Chem. Lett. 2016, 7, 2930-2934.

32. Knauf, R. R.; Brennaman, M. K.; Alibabaei, L.; Norris, M. R.; Dempsey, J. L. Revealing the Relationship between Semiconductor Electronic Structure and Electron Transfer Dynamics at Metal Oxide-Chromophore Interfaces. J. Phys. Chem. C 2013, 117 (48), 25259-25268.

33. Prasittichai, C.; Avila, J. R.; Farha, O. K.; Hupp, J. T. Systematic Modulation of Quantum (Electron) Tunneling Behavior by Atomic Layer Deposition on Nanoparticulate SnO2 and TiO2 Photoanodes. J. Am. Chem. Soc. 2013, 135 (44), 16328-16331.

Chapter 4: Effects of Annealing on Ultrafast Recombination Dynamics of Dye-Sensitized SnO_2/TiO_2 Core/Shell Films

4.1. Introduction.

The need to develop a method of storing solar energy to replace fossil fuels is becoming increasingly important. Dye-sensitized photoelectrosynthesis cells (DSPECs) utilize artificial photosynthesis to perform light-induced water oxidation catalysis at a photoanode, and CO_2 reduction catalysis at a photocathode to produce storable, carbon-based "solar fuels."[1-2] At the photoanode, a molecular chromophore-catalyst assembly is adsorbed to a metal oxide semiconductor, like SnO_2 or TiO_2. Photon absorption by the chromophore leads to electron injection into the conduction band of the metal oxide, followed by hole transfer out to the catalyst. This process must repeat four times for appreciable water oxidation catalysis to occur. Unfortunately, under open circuit conditions, charge recombination between the injected electron and oxidized species on the surface is too fast, despite assembly configurations.[2-5] Recently, a core/shell strategy for prolonging the lifetime of the charge separated state has shown considerable improvement over nanocrystalline films alone.[6-10] Understanding the fundamental dynamics at the interface of these core/shell films is essential to the continued development of DSPEC devices.

To construct core/shell films, a thin layer of a metal oxide semiconductor is deposited via atomic layer deposition (ALD) onto an existing nanocrystalline metal oxide film. Core/shell films utilize mismatched conduction band edges to funnel injected electrons to a lower energy

core, where they must tunnel through the shell to reach the oxidized species on the surface, thereby increasing the lifetime of the charge separated state.[11-12] In SnO_2/TiO_2 core/shell films, the SnO_2 conduction band is 0.4 V positive of that of TiO_2, allowing for a cascading mechanism of electron injection into the TiO_2 shell, followed by electron transfer into the core. As described in the previous chapter, transient absorption experiments on unannealed SnO_2/TiO_2 core/shell films sensitized with a ruthenium dye ($[Ru^{II}(bpy)_2(4,4'\text{-}(PO_3H_2)_2bpy)]^{2+}$, **RuP)**, where the TiO_2 is used as deposited and is, therefore, amorphous (*a*-TiO_2), revealed a deleterious recombination pathway on the picosecond time scale not present in the nanocrystalline TiO_2 or SnO_2 cases (Figure 4.1). It was hypothesized that defect states in the amorphous shell contributed to this loss and, therefore, could potentially be removed upon annealing, i.e. transforming the shell to nanocrystalline (*n*-TiO_2).[11]

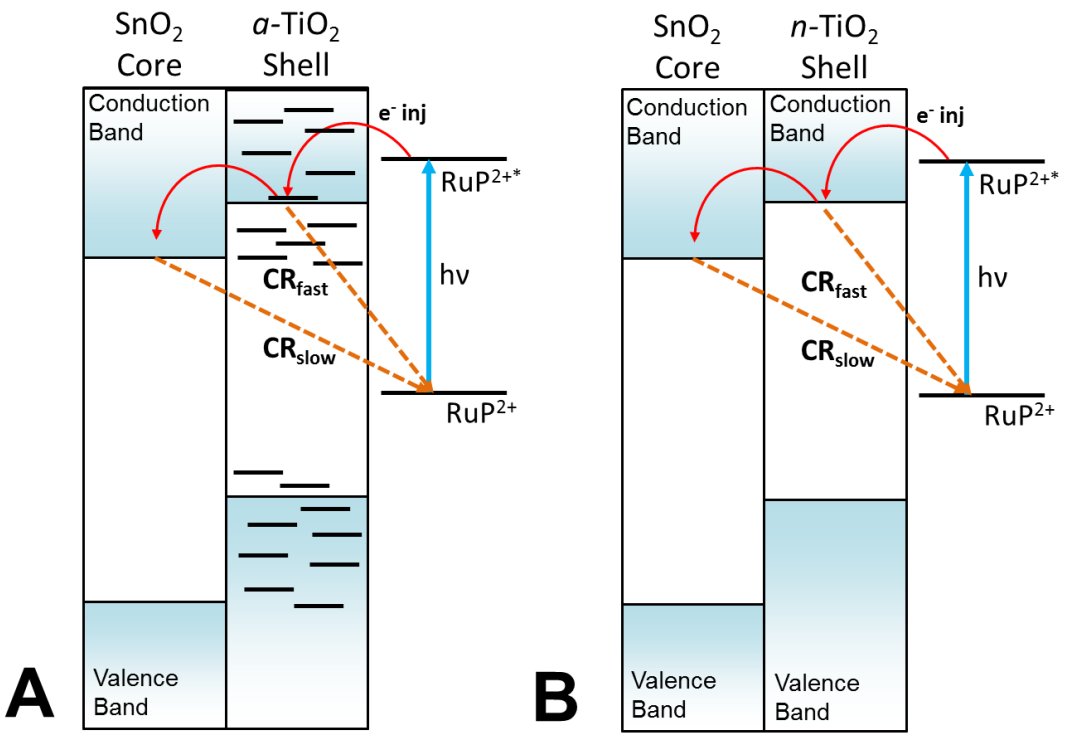

Figure 4.1. (A) Illustration of a band diagram describing photoinduced processes for an amorphous core/shell film (SnO_2/*a*-TiO_2|**RuP**). The hypothesized discrete shell states are shown as black lines. (B) Illustration of a band diagram describing the photoinduced processes of an annealed core/shell film (SnO_2/*n*-TiO_2|**RuP**). CR = Charge Recombination; e^- inj = electron injection.

Herein, we describe the interfacial dynamics of a dye-sensitized SnO_2/TiO_2 film with an amorphous shell (SnO_2/*a*-TiO_2|**RuP**) and upon annealing (SnO_2/*n*-TiO_2|**RuP**) using transient absorption spectroscopy. Time scales for electron injection and picosecond recombination are the same whether the shell is amorphous or nanocrystalline; however, the magnitude of these changes differ significantly. In the amorphous case, rapid recombination from the *a*-TiO_2 shell occurs in ~50% of charge separated states, where upon annealing, this fraction drops to 30% with the *n*-TiO_2 shell. While this decrease is beneficial for DSPEC device performance, when we

extend the time window through μs, we observe faster overall recombination in the SnO_2/*n*-TiO_2|**RuP** films (τ~310 μs) compared to SnO_2/*a*-TiO_2|**RuP** (τ~900 μs).

4.2. Experimental Methods.

4.2.1. Materials and Molecular Synthesis.

Deionized water was further purified using a Milli-Q water purification system. Perchloric acid (99.999%) was purchased from Sigma-Aldrich and used as received. Nanoparticle films of tin oxide (SnO_2) and zirconium oxide (ZrO_2) were constructed according to published procedures.[6, 13] Thin shells of titanium dioxide (TiO_2) were deposited using atomic layer deposition (ALD) and used as deposited (*a*-TiO_2) or after annealing (*n*-TiO_2). $[Ru^{II}(bpy)_2(4,4'\text{-}(PO_3H_2)_2bpy)]^{2+}[Cl]_2$ (**RuP**) was synthesized according to literature procedures[14-15] and dissolved in methanol (~1 mM) for electrode sensitization. Unannealed and annealed films were dye-loaded for transient absorption spectroscopy by soaking the films in the **RuP** methanol solution overnight (~14 hours). To remove unadsorbed dye, films were rinsed with methanol and dried under a stream of air. These films were stored in the dark.

4.2.2. Atomic Layer Deposition.

Atomic layer deposition (ALD) was performed using a Cambridge NanoTech Savannah S200 ALD system located in the Chapel Hill Analytical and Nanofabrication Lab (CHANL) cleanroom. The reaction chamber was set to 150 °C. The cylinder containing the TiO_2 precursor, tetrakis(dimethylamido)titanium(IV) (TiTDMA), was heated at 75 °C. The reaction chamber and the precursor cylinder were both heated at temperature for a minimum of 1 hour prior to use. Samples were added to the reaction chamber such that the nanoparticle film was near the center of the chamber and in-line with the precursor inlet and outlet ports. Samples were placed under dynamic vacuum with a continuous nitrogen purge (99.999%, further purified using an Entegris

GateKeeper Inert Gas Purifier) at temperature (150 °C) for a minimum of 10 minutes prior to deposition. Deposition was performed in "exposure mode" in which the chamber containing precursor is isolated from vacuum. For a typical deposition cycle, TiTDMA was pulsed for 2 seconds, isolated in the chamber for 20 seconds, and purged from the chamber for 60 seconds. Water was introduced under identical conditions except a 20-ms pulse was used. One cycle consisted of TiTDMA followed by water, and the number of cycles was used to control the thickness of the deposited layer. Thickness of the deposited oxide layer was quantified by performing ellipsometry (J. A. Woollam Variable Angle Spectroscopic Ellipsometer; located in CHANL) on a piece of planar, witness Si present in the reactor during ALD on the nanoparticle films. Annealed core/shell films were annealed under ambient conditions at 450°C for 30 minutes with a 45 minute ramp to temperature and left to cool for multiple hours.

4.2.3. Sample Preparation for Transient Absorption.

Samples for transient absorption were placed in 10 mm path length cuvettes at a 45° angle filled with 0.1 M $HClO_4$ aqueous solution. The cuvette was fitted with an O-ring seal and Kontes valve inlet to purge the sample with argon for at least 45 minutes prior to TA measurements to prevent effects from oxygen.

4.2.4. UV-Visible Absorption.

UV-Visible absorption spectra were collected using a UV-Visible-NIR absorption spectrophotometer (Agilent Technologies, model 8453A) operated with tungsten and deuterium lamps lit. Air was used as the baseline and samples were placed perpendicular to the beam path. An integration time of 0.5 s was used.

4.2.5. Femtosecond Transient Absorption.

Femtosecond transient absorption (fsTA) measurements were performed in a pump-probe configuration using a 1 kHz Ti:Sapphire, chirped pulse amplifier (Clark-MXR CPA-2001). The CPA output is 775 nm with a ~150 fs pulse width. The 480 nm pump pulse was created through sum-frequency generation of a portion of the 775 nm regenerative amplifier output and a generated signal (~1200 nm) output beam from a home-built optical parametric amplifier (OPA). The pump beam was chopped at 500 Hz and a power of 100 nJ/pulse was used. The white light probe (λ = 340-800 nm) is generated through super continuum generation by focusing a portion of the 775 nm output into a CaF_2 window that is continuously translating. The probe polarization is set to horizontal and the pump is set to ~54.7° (magic angle) relative to the probe. A computer-controlled optical delay line was used to delay the probe pulse relative to the pump. Pump and probe beams were focused to ~150 μm and spatially overlapped at the sample. Pulse-to-pulse changes in the probe beam through pump excitation were collected using a fiber optic-coupled multichannel spectrometer with a CMOS sensor. The sample is raster scanned throughout the experiment. The instrument response is ~250 fs and the sensitivity of the detector is 0.1 mOD.

4.2.6. Nanosecond-Microsecond Transient Absorption (1 ns-400 μs)

Nanosecond-microsecond transient absorption measurements were taken using the same pump pulse as fsTA, while the probe pulse was generated through continuum generation in a diode-laser pumped photonic crystal fiber. Pump-probe delay was electronically controlled with a time resolution of 500 ps.

4.2.7. Overlaying Kinetics from Different TA Measurements.

Transient absorption measurements with different ranges of pump-probe delay were taken with the same photon flux and kinetic traces were normalized to the same time points for each instrument. Repeated experiments demonstrated the reproducibility of the kinetic measurements.

4.3. Results and Discussion.

Photoexcitation of **RuP** creates a singlet metal-to-ligand charge transfer state (^{1}MLCT) that undergoes rapid (< 100 fs) intersystem crossing to a triplet MLCT state (^{3}MLCT). The ^{3}MLCT manifests in the transient absorption spectrum as a ground state bleach (GSB) around 460 nm and an excited state absorption (ESA) around 380 nm corresponding to π-π* transitions on the bipyridine radical anion ($bpy^{\bullet-}$).[16] The excited state lifetime of surface-bound **RuP** is on the order of hundreds of nanoseconds, as measured on ZrO_2,[2] where electron injection cannot occur. On SnO_2|**RuP**, the ESA decays rapidly, while the GSB amplitude is maintained. This behavior is a signature of electron injection into the SnO_2 CB.

The loss of the ESA is biexponential and describes the electron injection dynamics. Electron injection rates depend on the overlap between the density of states in the semiconductor conduction band and the excited state manifold of the chromophore.[16] Vibrational cooling of the ^{3}MLCT competes with injection leading to this biexponential behavior in the $bpy^{\bullet-}$ loss at 380 nm. As described in Chapter 3,[11] the time scale for electron injection SnO_2|**RuP** is 3.8 ps and 25 ps. In the previous study, the unannealed core/shell films behaved unexpectedly, where the decay in the ESA (τ = 22 ps, 280 ps) is accompanied by a decay in the GSB (τ = 220 ps) independent of shell thickness. The lack of thickness dependence indicates the electron injection is occurring into the *a*-TiO_2 shell, rather than tunneling through the shell. Likewise, the loss of the GSB is occurring from the shell, though the exact mechanism is still unclear. The transient absorption

spectra of SnO_2/*a*-TiO_2 (0.87 nm)|**RuP** presented in Figure 4.2A display similar kinetics where the ESA decays with time constants of 28.1 ps and 311 ps (Table 4.1) and 49% of the GSB decays in 207 ps (Table 4.2).

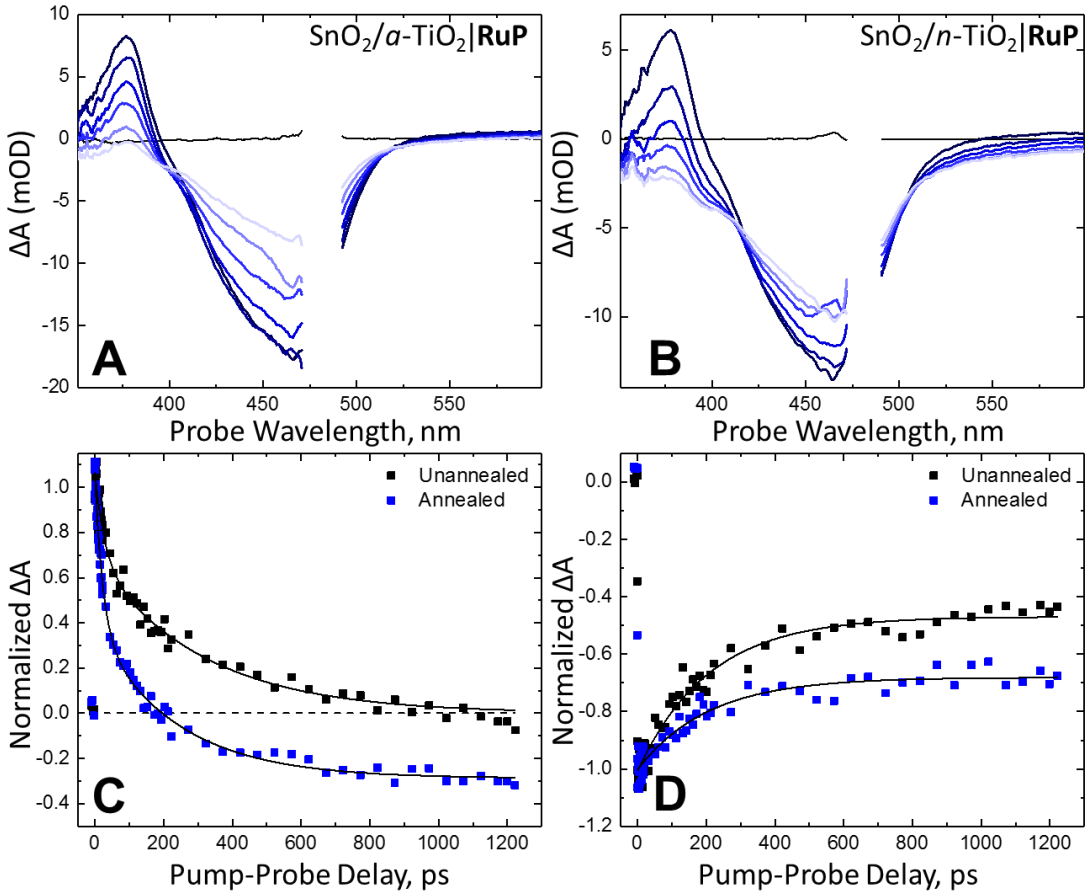

Figure 4.2. (A) Transient absorption spectra of SnO_2/*a*-TiO_2(0.87 nm)|**RuP** and (B) SnO_2/*n*-TiO_2|**RuP** after 490 nm (100 nJ/pulse) photoexcitation in 0.1 M $HClO_4$ (aq) at pump-probe delays of -6 ps (black), 1 ps (dark blue), 25 ps, 75 ps, 200 ps, 500 ps, and 1100 ps (light blue). (C) Normalized transient absorption kinetics for SnO_2/*a*-TiO_2(0.87 nm)|**RuP** (black) and SnO_2/*n*-TiO_2(0.87 nm)|**RuP** (blue) at 380 nm. Biexponential fits are shown as solid lines with results in Table 4.1. (D) Normalized transient absorption kinetics for SnO_2/*a*-TiO_2(0.87 nm)|**RuP** (black) and SnO_2/*n*-TiO_2(0.87 nm)|**RuP** (blue) at 450 nm. Fits are shown as solid lines.

Annealing these films to change the shell from amorphous (*a*-TiO_2) to nanocrystalline (*n*-TiO_2) minimizes some of the amplitude loss in the GSB. Interestingly, the loss of the ESA occurs with a fast (τ_1 = 23.3 ps) and slow (τ_2 = 237 ps) component, on the same time scale as the unannealed film. Similarly, the GSB decays with a time constant of 206 ps. The differences between amorphous and annealed SnO_2/TiO_2 films lie in the magnitude of the amplitude changes of the ESA and GSB. In particular, we observe an increase in the loss of the ESA and a decrease in loss of the GSB from 49% in SnO_2/*a*-TiO_2(0.87 nm)|**RuP** to 31% in SnO_2/*n*-TiO_2(0.87 nm)|**RuP**. It is difficult to determine if the increase in the loss of the ESA is due to an increased injection yield or simply from the decrease in GSB loss, as these two bands are related by the spectrum of the oxidized chromophore (**RuP**$^{3+}$), and they decay together as recombination occurs.[16]

$$y = Offset + A_1 e^{-x/\tau_1} + A_2 e^{-x/\tau_2} \quad (4.1)$$

Table 4.1. Results of biexponential fit (eq. 4.1) to ESA loss (λ_{probe} = 380 nm).

	SnO_2/*a*-TiO_2|**RuP**	SnO_2/*n*-TiO_2|**RuP**	ZrO_2/*a*-TiO_2|**RuP**	ZrO_2/*n*-TiO_2|**RuP**
Offset	0%	17.5%	18%	20%
A_1	35%	42%	36%	38%
τ_1	28.1 ps	23.3 ps	18.2 ps	15.4 ps
A_2	65%	40.5%	46%	42%
τ_2	311 ps	237 ps	188 ps	170 ps

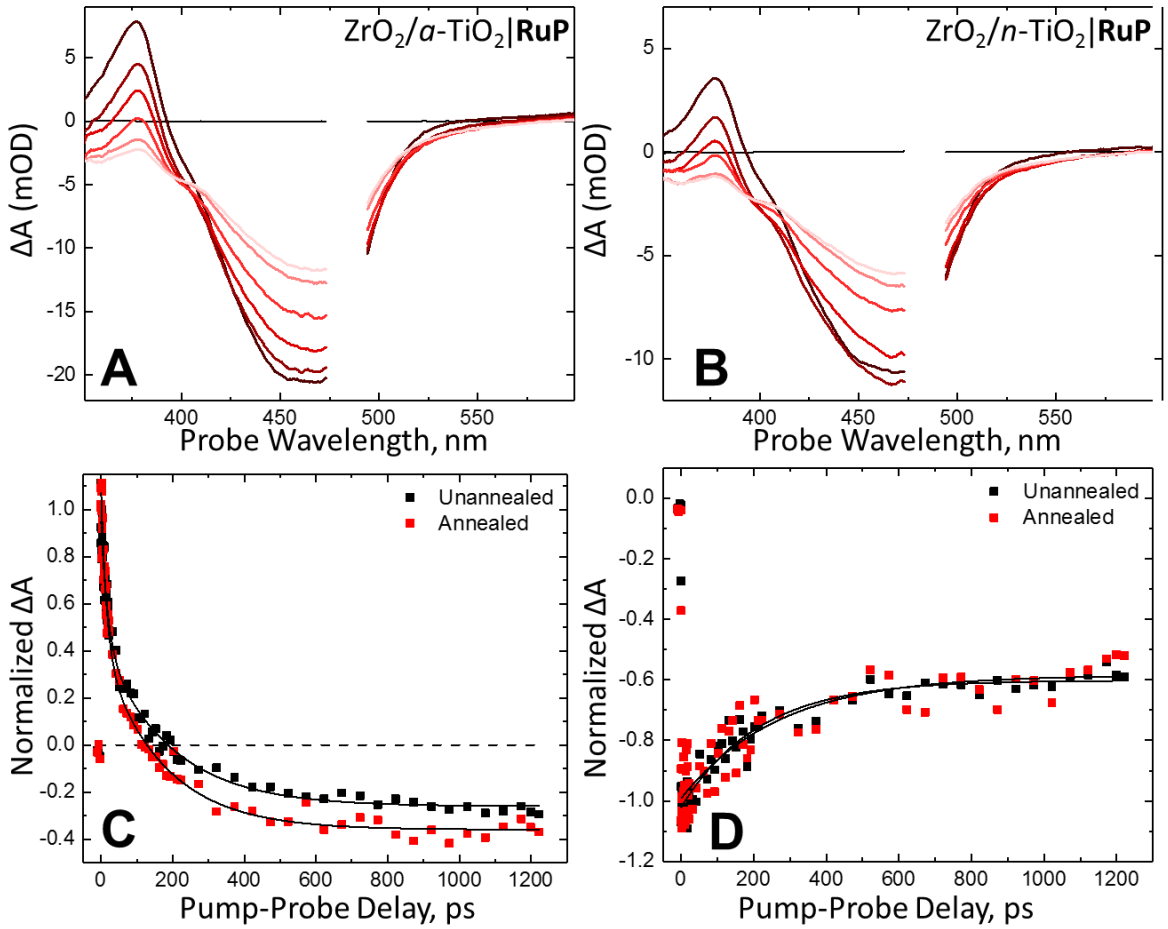

Figure 4.3. (A) Transient absorption spectra of ZrO_2/*a*-TiO_2(0.87 nm)|**RuP** and (B) ZrO_2/*n*-TiO_2|**RuP** after 490 nm (100 nJ/pulse) photoexcitation in 0.1 M $HClO_4$ (aq) at pump-probe delays of -6 ps (black), 1 ps (dark red), 25 ps, 75 ps, 200 ps, 500 ps, and 1100 ps (light red). (C) Normalized transient absorption kinetics for ZrO_2/*a*-TiO_2(0.87 nm)|**RuP** (black) and ZrO_2/*n*-TiO_2(0.87 nm)|**RuP** (red) at 380 nm. Biexponential fits are shown as solid lines with results in Table 4.1. (D) Normalized transient absorption kinetics for ZrO_2/*a*-TiO_2(0.87 nm)|**RuP** (black) and ZrO_2/*n*-TiO_2(0.87 nm)|**RuP** (red) at 450 nm. Fits are shown as solid lines.

The ZrO_2/TiO_2|**RuP** films exhibit the same ESA at 380 nm and GSB at 460 nm characteristic of the **RuP** excited state. On ZrO_2|**RuP**, where electron injection cannot occur, no significant decay in the transient absorption spectra within 1 ns is observed, so the dynamics observed in the ZrO_2/TiO_2 core/shell films are from interactions with the TiO_2 shell only. The $bpy^{\bullet-}$ bands in unannealed (ZrO_2/*a*-TiO_2(0.87 nm)|**RuP**) and annealed (ZrO_2/*n*-TiO_2(0.87 nm)|**RuP**) films undergo a biphasic decay with time constants of 18.2 ps and 188 ps, and 15.4 ps and 170 ps, respectively (Table 4.1). The difference in time scale between ZrO_2/*a*-TiO_2 and ZrO_2/*n*-TiO_2 is insignificant, and though the magnitude of the ESA decay is slightly larger in the annealed films, it is minor compared to the large disparity in that of the SnO_2/TiO_2 films. The GSB decay for the ZrO_2/TiO_2 core/shell films (Figure 4.3) show no change after annealing with a 50% loss with time constants of ~250 ps (Table 4.2).

To get the full picture of the GSB recovery, we must expand our time window from picoseconds through 100s of microseconds. Figure 4.4 displays the full GSB decay of SnO_2/*a*-TiO_2(0.87 nm)|**RuP** (black) and SnO_2/*n*-TiO_2(0.87 nm)|**RuP**. These kinetics are complex and multiexponential, requiring four exponential components for SnO_2/TiO_2 films and three for ZrO_2/TiO_2 films (Table 4.2). The unannealed SnO_2/*a*-TiO_2(0.87 nm)|**RuP** film exhibits behavior similar to those described in Chapter 3 of this dissertation, where there is an ultrafast decay (τ_1 = 207 ps) representing a 50% loss of the CSS and a small portion of extremely long-lived CSSs (τ_4 = 900 μs). The time constant for the long-lived CSSs in the unannealed films, including SnO_2/*a*-TiO_2(0.87 nm)|**RuP** is exponentially dependent on shell thickness, indicating that the electron is tunneling through the *a*-TiO_2 shell from the SnO_2 core to recombine with the oxidized chromophore.[11-12, 17] Once annealed, SnO_2/*n*-TiO_2(0.87 nm)|**RuP**, the portion of ultrafast decay

decreases from 50% to 30%; however, the longest lifetime measured is 311 μs, almost three times faster than the unannealed film.

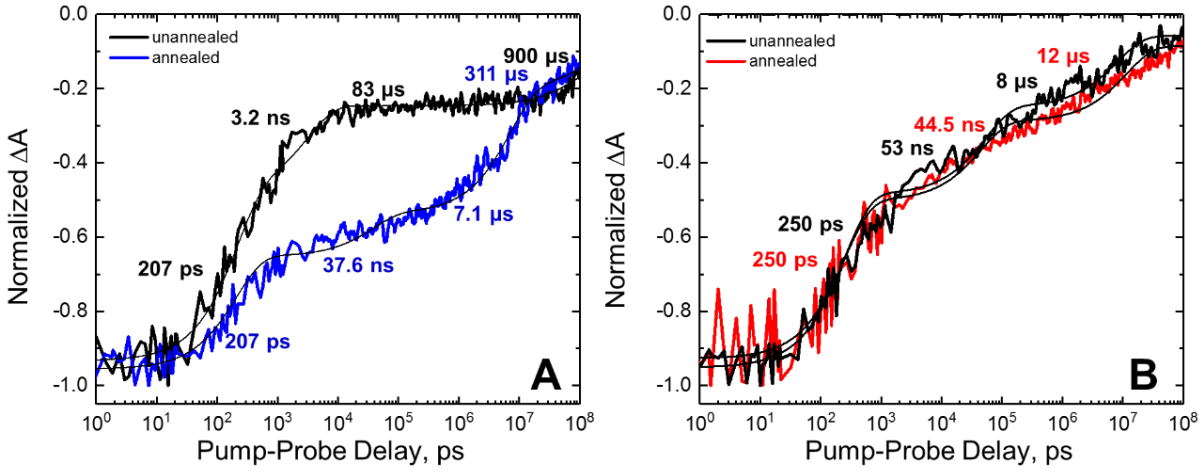

Figure 4.4. (A) Transient absorption kinetics of SnO_2/*a*-TiO_2(0.87 nm)|**RuP** (black) and SnO_2/*n*-TiO_2(0.87 nm)|**RuP** (blue) at a probe wavelength of 450 nm. Each transient is fit to a quad-exponential (Eq. 4.2), shown as black solid lines. Amplitudes and time constants are summarized in Table 4.2. (B) Transient absorption kinetics of ZrO_2/*a*-TiO_2(0.87 nm)|**RuP** (black) and ZrO_2/*n*-TiO_2(0.87 nm)|**RuP** (red) at a probe wavelength of 450 nm. Each transient is fit to a tri-exponential function (Eq 4.3), shown as black solid lines. Amplitudes and time constants are summarized in Table 4.2.

The GSB of **RuP** on the ZrO_2/TiO_2 films decay a lot faster than SnO_2/TiO_2 with time constants of 250 ps, 53 ns and 8 μs, and 250 ps, 44.5 ns, and 12 μs on ZrO_2/*a*-TiO_2(0.87 nm)|**RuP** and ZrO_2/*n*-TiO_2(0.87 nm)|**RuP**, respectively (Table 4.2). In both amorphous and nanocrystalline ZrO_2/TiO_2 cases, 50% of the decay occurs within 1 ns, while the rest gradually return back to baseline on the nanosecond/microsecond time scale. This is expected as electrons will not inject into the ZrO_2 core, speeding up the GSB recovery dynamics.

$$y = A_1 e^{-x/\tau_1} + A_2 e^{-x/\tau_2} + A_3 e^{-x/\tau_3} + A_4 e^{-x/\tau_4} \quad (4.2)$$

$$y = A_1 e^{-x/\tau_1} + A_2 e^{-x/\tau_2} + A_3 e^{-x/\tau_3} \quad (4.3)$$

Table 4.2. Results of multiexponential fits for GSB recovery at λ_{probe} = 450 nm.

	SnO_2/*a*-TiO_2|**RuP**	SnO_2/*n*-TiO_2|**RuP**	ZrO_2/*a*-TiO_2|**RuP**	ZrO_2/*n*-TiO_2|**RuP**
A_1	49%	31%	51%	50%
τ_1	207 ps	207 ps	250 ps	250 ps
A_2	25%	13%	26%	25%
τ_2	3.2 ns	37.6 ns	53 ns	44.5 ns
A_3	10%	35%	23%	25%
τ_3	83 μs	7.1 μs	8 μs	12 μs
A_4	16%	21%		
τ_4	900 μs	311 μs		

The stark contrast between the GSB decay kinetics of SnO_2/*a*-TiO_2(0.87 nm)|**RuP** and SnO_2/*n*-TiO_2(0.87 nm)|**RuP** is indicative of a change in the TiO_2 shell upon annealing. The ultrafast recombination component, though still present, is diminished in the annealed film. This suggests that the annealing process rids the TiO_2 shell of some of the states that are responsible for this ultrafast loss of oxidized chromophores. While the smaller percentage of ultrafast recombination is an advantage for annealed films, that gain is counteracted by τ_4, which is three times faster in SnO_2/*n*-TiO_2(0.87 nm)|**RuP** than the amorphous film.

As deposited, the amorphous TiO_2 shell is likely a compilation of discrete empty and filled states, rather than a typical band structure found in a nanocrystalline film. These discrete states have varying energies with evidence for filled states in the "mid-gap" region in the *a*-TiO_2 film capable of transporting holes.[18] The mechanism of ultrafast recombination in SnO_2/*a*-TiO_2(0.87 nm)|**RuP** may be geminate or non-geminate in nature.[11] In a geminate mechanism, the injected

electron recombines with the oxidized chromophore it originated from, while in a non-geminate case, the oxidized chromophore is reduced by filled mid-gap states in the *a*-TiO_2 shell. Ultrafast recombination in the annealed core/shell film, SnO_2/*n*-TiO_2(0.87 nm)|**RuP**, is diminished, but not completely eradicated. This suggests a transformation from discrete states in *a*-TiO_2 to a more band-type structure in *n*-TiO_2; however, some of these discrete trap states are likely still present in *n*-TiO_2 as observed by the loss in the GSB.

The major loss in the lifetime of the long-lived charge separated state in SnO_2/*n*-TiO_2(0.87 nm)|**RuP** compared to SnO_2/*a*-TiO_2(0.87 nm)|**RuP** is also an effect of annealing. The longest lifetime of SnO_2/*a*-TiO_2(0.87 nm)|**RuP** is consistent with tunneling from the SnO_2 core through the TiO_2 shell as it follows the exponential dependence of τ_4 on thickness established in Chapter 3. The faster τ_4 observed for SnO_2/*n*-TiO_2(0.87 nm)|**RuP** suggests a possible change in the barrier height introduced by the shell, or a change in the interface between core and shell. Knauf and coworkers observed a loss in the thickness dependence of recombination upon annealing in dye-sensitized SnO_2/TiO_2 core/shell films.[12] The lack of thickness dependence implies a loss of the tunneling efficacy observed in the unannealed, amorphous films. It is possible that states at the interface of the core and shell may be affected through annealing via mixing or delamination. Evidence for mixing of states in SnO_2/TiO_2 core/shell films have been observed electrochemically.[19]

On ZrO_2/TiO_2 core/shell films, where the shell dynamics are isolated, the recombination dynamics are not significantly affected upon annealing. This suggests that the underlying substrate may dictate how the ALD TiO_2 deposits on the surface. The size of the nanoparticles and pores in the nanocrystalline film may cause the TiO_2 to grow in a way that is not significantly affected when annealed. It may also suggest that annealing in the SnO_2/TiO_2 films

does electronically alter the states at the interface. If the changes were isolated in the TiO_2 film, we would expect to see similar changes on ZrO_2/TiO_2 upon annealing, as well.

4.4. Conclusions

The interfacial dynamics of dye-sensitized SnO_2/TiO_2 and ZrO_2/TiO_2 core/shell films were investigated as deposited (amorphous) and after annealing (nanocrystalline) using transient absorption spectroscopy. Annealing the SnO_2/TiO_2 lessens the contribution of ultrafast recombination compared to an amorphous TiO_2 shell; however, the longest lifetime is 3x longer in the amorphous core/shell case. This suggests that annealing the film changes fundamental properties of the core/shell films, though, it is difficult to tell if the core and shell states are mixing or if delamination is occurring and communication is diminished. The changes in behavior also indicate a shift from discrete states in the amorphous shell to a more band-like nanocrystalline structure in the annealed films. To determine the origin of these changes, structural, and electrochemical characterization must be performed. A temperature dependence, where the films are annealed at different temperatures, might be useful in characterizing the nature of the interaction between core and shell.

REFERENCES

1. Brennaman, M. K.; Dillon, R. J.; Alibabaei, L.; Gish, M. K.; Dares, C. J.; Ashford, D. L.; House, R. L.; Meyer, G. J.; Papanikolas, J. M.; Meyer, T. J. Finding the Way to Solar Fuels with Dye-Sensitized Photoelectrosynthesis Cells. *J. Am. Chem. Soc.* **2016,** *138* (40), 13085-13102.

2. Ashford, D. L.; Gish, M. K.; Vannucci, A. K.; Brennaman, M. K.; Templeton, J. L.; Papanikolas, J. M.; Meyer, T. J. Molecular Chromophore-Catalyst Assemblies for Solar Fuel Applications. *Chem. Rev.* **2015,** *115* (23), 13006-13049.

3. Bettis, S. E.; Hanson, K.; Wang, L.; Gish, M. K.; Concepcion, J. J.; Fang, Z.; Meyer, T. J.; Papanikolas, J. M. Photophysical Characterization of a Chromophore/Water Oxidation Catalyst Containing a Layer-by-Layer Assembly on Nanocrystalline TiO_2 using Ultrafast Spectroscopy. *J. Phys. Chem. A* **2014,** *118* (45), 10301-10308.

4. Bettis, S. E.; Ryan, D. M.; Gish, M. K.; Alibabaei, L.; Meyer, T. J.; Waters, M. L.; Papanikolas, J. M. Photophysical Characterization of a Helical Peptide Chromophore-Water Oxidation Catalyst Assembly on a Semiconductor Surface using Ultrafast Spectroscopy. *J. Phys. Chem. C* **2014,** *118* (12), 6029-6037.

5. Wang, L.; Ashford, D. L.; Thompson, D. W.; Meyer, T. J.; Papanikolas, J. M. Watching Photoactivation in a Ru(II) Chromophore-Catalyst Assembly on TiO_2 by Ultrafast Spectroscopy. *J. Phys. Chem. C* **2013,** *117* (46), 24250-24258.

6. Sherman, B. D.; Ashford, D. L.; Lapides, A. M.; Sheridan, M. V.; Wee, K. R.; Meyer, T. J. Light-Driven Water Splitting with a Molecular Electroassembly-Based Core/Shell Photoanode. *J. Phys. Chem. Lett.* **2015,** *6* (16), 3213-3217.

7. Alibabaei, L.; Brennaman, M. K.; Norris, M. R.; Kalanyan, B.; Song, W. J.; Losego, M. D.; Concepcion, J. J.; Binstead, R. A.; Parsons, G. N.; Meyer, T. J. Solar Water Splitting in a Molecular Photoelectrochemical Cell. *Proc. Natl. Acad. Sci. U. S. A.* **2013,** *110* (50), 20008-20013.

8. Alibabaei, L.; Sherman, B. D.; Norris, M. R.; Brennaman, M. K.; Meyer, T. J. Visible Photoelectrochemical Water Splitting into H_2 and O_2 in a Dye-Sensitized Photoelectrosynthesis Cell. *Proc. Natl. Acad. Sci. U. S. A.* **2015,** *112* (19), 5899-5902.

9. Karlsson, M.; Jogi, I.; Eriksson, S. K.; Rensmo, H.; Boman, M.; Boschloo, G.; Hagfeldt, A. Dye-Sensitized Solar Cells Employing a SnO_2-TiO_2 Core-shell Structure Made by Atomic Layer Deposition. *Chimia* **2013,** *67* (3), 142-148.

10. Kay, A.; Gratzel, M. Dye-Sensitized Core-Shell Nanocrystals: Improved Efficiency of Mesoporous Tin Oxide Electrodes Coated with a Thin Layer of an Insulating Oxide. *Chem. Mater.* **2002,** *14* (7), 2930-2935.

11. Gish, M. K.; Lapides, A. M.; Brennaman, M. K.; Templeton, J. L.; Meyer, T. J.; Papanikolas, J. M. Ultrafast Recombination Dynamics in Dye-Sensitized SnO2/TiO2 Core/Shell Films. *J. Phys. Chem. Lett.* **2016,** *7* (24), 5297-5301.

12. Knauf, R. R.; Kalanyan, B.; Parsons, G. N.; Dempsey, J. L. Charge Recombination Dynamics in Sensitized SnO_2/TiO_2 Core/Shell Photoanodes. *J. Phys. Chem. C* **2015,** *119* (51), 28353-28360.

13. Green, A. N. M.; Palomares, E.; Haque, S. A.; Kroon, J. M.; Durrant, J. R. Charge Transport Versus Recombination in Dye-Sensitized Solar Cells Employing Nanocrystalline TiO_2 and SnO_2 Films. *J. Phys. Chem. B* **2005,** *109* (25), 12525-12533.

14. Norris, M. R.; Concepcion, J. J.; Glasson, C. R. K.; Fang, Z.; Lapides, A. M.; Ashford, D. L.; Templeton, J. L.; Meyer, T. J. Synthesis of Phosphonic Acid Derivatized Bipyridine Ligands and Their Ruthenium Complexes. *Inorg. Chem.* **2013,** *52* (21), 12492-12501.

15. Lapides, A. M.; Ashford, D. L.; Hanson, K.; Torelli, D. A.; Templeton, J. L.; Meyer, T. J. Stabilization of a Ruthenium(II) Polypyridyl Dye on Nanocrystalline TiO_2 by an Electropolymerized Overlayer. *J. Am. Chem. Soc.* **2013,** *135* (41), 15450-15458.

16. Zigler, D. F.; Morseth, Z. A.; Wang, L.; Ashford, D. L.; Brennaman, M. K.; Grumstrup, E. M.; Brigham, E. C.; Gish, M. K.; Dillon, R. J.; Alibabaei, L., et al. Disentangling the Physical Processes Responsible for the Kinetic Complexity in Interfacial Electron Transfer of Excited Ru(II) Polypyridyl Dyes on TiO_2. *J. Am. Chem. Soc.* **2016,** *138* (13), 4426-4438.

17. Prasittichai, C.; Avila, J. R.; Farha, O. K.; Hupp, J. T. Systematic Modulation of Quantum (Electron) Tunneling Behavior by Atomic Layer Deposition on Nanoparticulate SnO_2 and TiO_2 Photoanodes. *J. Am. Chem. Soc.* **2013,** *135* (44), 16328-16331.

18. Hu, S.; Shaner, M. R.; Beardslee, J. A.; Lichterman, M.; Brunschwig, B. S.; Lewis, N. S. Amorphous TiO_2 Coatings Stabilize Si, GaAs, and GaP Photoanodes for Efficient Water Oxidation. *Science* **2014,** *344* (6187), 1005-1009.

19. James, E. M.; Barr, T. J.; Meyer, G. J. Evidence for an Electronic State at the Interface between the SnO_2 Core and the TiO_2 Shell in Mesoporous SnO_2/TiO_2 Thin Films. *ACS Appl. Energy Mater.* **2018,** *1* (2), 859-867.

Chapter 5: Evidence for a Time-Resolved Stark Effect in "Buried" Dye-Sensitized Photoanodes

This chapter presents work for a manuscript in preparation with co-authors M. Kyle Brennaman, Alexander M. Lapides, Joseph L. Templeton, Thomas J. Meyer, and John M. Papanikolas.

5.1. Introduction.

Dye-sensitized photoelectrosynthesis cells (DSPECs) incorporate light-harvesting dyes, molecular catalysts, and a wide band gap metal oxide semiconductor working together in concert to convert sunlight into "solar fuels" from H_2O and CO_2.[1-3] At a DSPEC photoanode, where water oxidation occurs, chromophores are typically surface-bound to a metal oxide, such as titanium dioxide (TiO_2), through phosphonate ($–PO_3H_2$)[4] or carboxylate (–COOH) linkages.[5] Photon absorption by the chromophore leads to electron injection into the conduction band (CB) of the semiconductor, followed by hole transfer out to the catalyst. The photoactivation process is repeated four times to build up the required equivalents to drive water oxidation. The complexity of the overall process requires molecules that are stable on the surface under illumination that have the ability to form long-lived charge separated states (CSS) between the electrons in the CB and the oxidized species on the surface.[2]

Chromophore-catalyst assemblies have been synthesized with covalent bonds prior to attachment,[6-10] or created on the surface through co-loading,[11-12] layer-by-layer,[13-15] or electropolymerization[16-17] techniques. The high demands placed on these molecules in repetitive light absorption and electron transfer events lead to significant issues with surface stability and degradation, particularly, under aqueous conditions at higher pH where the rate of water

oxidation is enhanced by added bases.[18-19] Under these conditions, even with robust surface binding groups such as carboxylates or phosphonates, the linkages are readily hydrolyzed under basic conditions leading to desorption from semiconductor surfaces.[19] One strategy to combat surface instability is deposition of a protective, metal oxide overlayer, such as aluminum oxide (Al_2O_3) or TiO_2, following dye adsorption, by atomic layer deposition (ALD).[20]

Thin ALD overlayers have been shown to significantly increase stabilities for surface-bound chromophores under illumination and at high pH.[2] ALD has also been used to create and stabilize non-bonding chromophore-catalyst assemblies (Figure 5.1A) in which long-range electronic coupling provides a basis for integrating electronic interactions and pathways for multiple electron transfers.[20] In this strategy, surface-bound chromophores are embedded or "buried" in ~1-2 nm of an amorphous metal oxide layer by ALD followed by surface-binding of the catalyst to the deposited overlayer with the catalyst further stabilized by addition of a few monolayers of metal oxide. In earlier experiments, these highly stabilized, "mummy" assemblies have been shown to provide high degrees of surface stability through multiple oxidation states based on electrochemical measurements.[20] Nonetheless, little is known about the effects of these overlayers on fundamental interfacial dynamics between the metal oxide, chromophore, and overlayer under open circuit conditions.

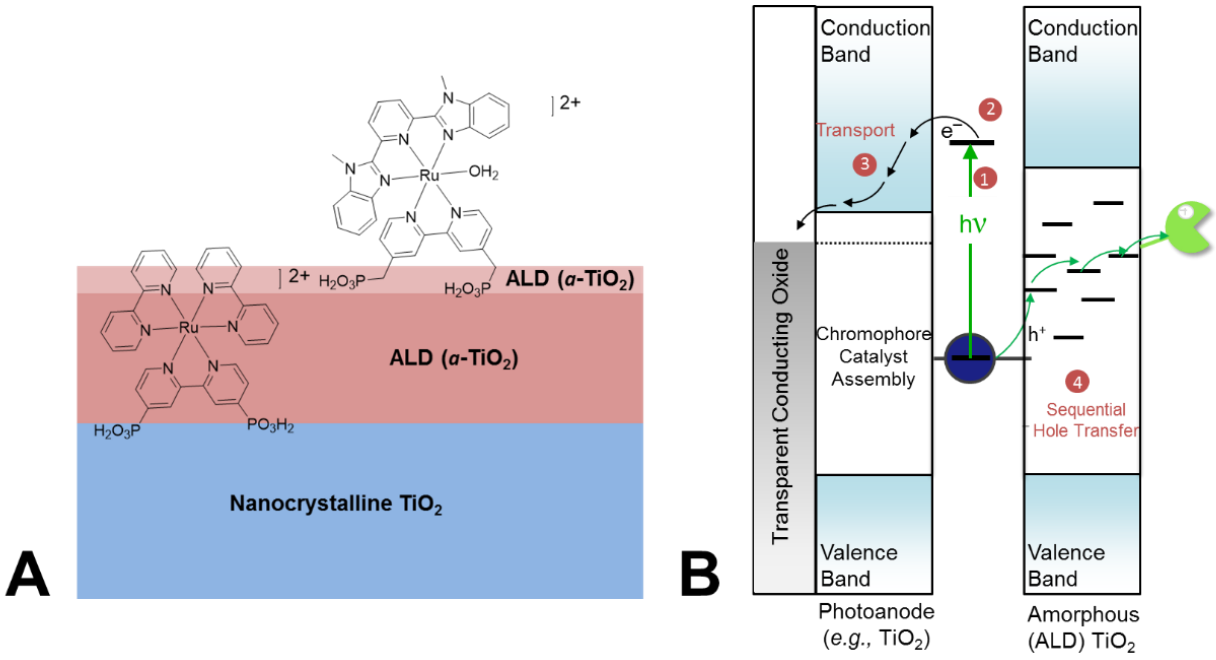

Figure 5.1. (A) A crosswise view of a "mummy" assembly with $[Ru^{II}(bpy)_2(4,4'\text{-}(PO_3H_2)_2bpy)]^{2+}$ (**RuP^{2+}**) surface-bound to a nanocrystalline TiO_2 film, protected with a-TiO_2 deposited by ALD. The water oxidation catalyst, $[Ru^{II}$(2,6-bis(1-methyl-1H-benzo[d]imidazole-2-yl)pyridine)(4,4'-dpcbpy)$(OH_2)]^{2+}$, **Ru$_{cat}$**, was loaded on the *a*-TiO_2 overlayer and protected with a thin layer of *a*-TiO_2 deposited by ALD. (B) Schematic energy level diagram illustrating relative energy levels in the *a*-TiO_2 overlayers in a DSPEC "mummy" chromophore-catalyst assembly, where step (1) is photoexcitation, (2) is electron (e^-) injection into the CB of TiO_2, (3) is transport through TiO_2 to a transparent conducting oxide (TCO), and (4) is sequential hole (h^+) transfer to the *a*-TiO_2, transporting the oxidative equivalent to the catalyst.

Here, we focus on the effects of an amorphous TiO_2 (*a*-TiO_2) overlayer on the model chromophore, **RuP^{2+}** ($[Ru^{II}(bpy)_2(4,4'\text{-}(PO_3H_2)_2bpy)]^{2+}$), adsorbed to a nanocrystalline metal oxide semiconductor. The *a*-TiO_2 film was prepared from the precursor tetrakis(dimethyl)titanium (TiTDMA) with hole conductivity properties in the resulting oxide that, if properly exploited in DSPEC applications, could assist in the catalytic process (Figure

5.1B).[21] In the hypothesized mechanism (Figure 5.1B, eq. 5.1-5.4), excitation of the chromophore, $\mathbf{RuP^{2+}}$ (Eq. 5.1) on the surface, gives the metal-to-ligand charge transfer (MLCT) excited state ($\mathbf{RuP^{2+}}$*).[22] The excited state undergoes electron injection (Eq. 5.2) into the CB of TiO_2, followed by sequential hole transfer through defect states in the *a*-TiO_2 overlayer (Eq. 5.3) to the external catalyst ($\mathbf{Ru_{cat}^{2+}}$) with the latter bound to *a*-TiO_2 (Eq. 5.4). In catalytic cycles, the chromophore is returned to its ground state, resetting it for a following photoactivation step:

$$TiO_2|\mathbf{RuP^{2+}}|a\text{-}TiO_2|\mathbf{Ru_{cat}^{2+}} + h\nu \rightarrow TiO_2|\mathbf{RuP^{2+*}}|a\text{-}TiO_2|\mathbf{Ru_{cat}^{2+}} \quad (5.1)$$

$$TiO_2|\mathbf{RuP^{2+*}}|a\text{-}TiO_2|\mathbf{Ru_{cat}^{2+}} \rightarrow TiO_2(e^-)|\mathbf{RuP^{3+}}|a\text{-}TiO_2|\mathbf{Ru_{cat}^{2+}} \quad (5.2)$$

$$TiO_2(e^-)|\mathbf{RuP^{3+}}|a\text{-}TiO_2|\mathbf{Ru_{cat}^{2+}} \rightarrow TiO_2(e^-)|\mathbf{RuP^{2+}}|a\text{-}TiO_2(h^+)|\mathbf{Ru_{cat}^{2+}} \quad (5.3)$$

$$TiO_2(e^-)|\mathbf{RuP^{2+}}|a\text{-}TiO_2(h^+)|\mathbf{Ru_{cat}^{2+}} \rightarrow TiO_2(e^-)|\mathbf{RuP^{2+}}|a\text{-}TiO_2|\mathbf{Ru_{cat}^{3+}} \quad (5.4)$$

In exploiting these properties for DSPEC applications, the influence of local dynamics on the properties of the final assemblies play an important role. We report the effect of varying cycles the *a*-TiO_2 overlayer (xc-*a*-TiO_2) on injection by the surface-bound chromophore and subsequent recombination using ultrafast transient absorption spectroscopy. In this study, we explore photophysical dynamics on both TiO_2 (TiO_2|**RuP**|xc-*a*-TiO_2) and ZrO_2 (ZrO_2|**RuP**|xc-*a*-TiO_2) as the underlying nanocrystalline films (Figure 5.2). ZrO_2 is commonly used as a control in studies of photoanodes because its CB energy lies sufficiently high to avoid appreciable electron injection from $\mathbf{RuP^{2+*}}$.[22] The *a*-TiO_2 overlayer in Figure 5.2 is drawn with fully realized conduction and valence bands although the amorphous nature of *a*-TiO_2 suggests that it is more likely a collection of localized states with a defect density throughout its "band gap." As such, it is important to note that electron injection into the *a*-TiO_2 overlayer is energetically feasible.[23]

With ZrO_2 as the electrode, it is possible to isolate and probe the interaction between $\mathbf{RuP^{2+*}}$ and the *a*-TiO_2 overlayer.

The specific processes of interest for transient absorption measurements on $TiO_2|\mathbf{RuP}|$xc-*a*-TiO_2 are:

$$TiO_2|\mathbf{RuP^{2+}}|a\text{-}TiO_2 + h\nu \rightarrow TiO_2|\mathbf{RuP^{2+*}}|a\text{-}TiO_2 \quad (5.5)$$

$$TiO_2|\mathbf{RuP^{2+*}}|a\text{-}TiO_2 \rightarrow TiO_2(e^-)|\mathbf{RuP^{3+}}|a\text{-}TiO_2 \quad (5.6)$$

$$TiO_2(e^-)|\mathbf{RuP^{3+}}|a\text{-}TiO_2 \rightarrow TiO_2(e^-)|\mathbf{RuP^{2+}}|a\text{-}TiO_2(h^+) \quad (5.7)$$

In $ZrO_2|\mathbf{RuP}|$xc-*a*-TiO_2, there is no interaction with the underlying nanocrystalline film resulting in these processes:

$$ZrO_2|\mathbf{RuP^{2+}}|a\text{-}TiO_2 + h\nu \rightarrow ZrO_2|\mathbf{RuP^{2+*}}|a\text{-}TiO_2 \quad (5.8)$$

$$ZrO_2|\mathbf{RuP^{2+*}}|a\text{-}TiO_2 \rightarrow ZrO_2|\mathbf{RuP^{3+}}|a\text{-}TiO_2\,(e^-) \quad (5.9)$$

$$ZrO_2|\mathbf{RuP^{3+}}|a\text{-}TiO_2\,(e^-) \rightarrow ZrO_2|\mathbf{RuP^{2+}}|a\text{-}TiO_2\,(e^-\text{-}h^+) \quad (5.10)$$

With the electron and hole localized in the *a*-TiO_2 overlayer in $ZrO_2|\mathbf{RuP^{2+}}|a$-$TiO_2$, an electric field forms around the re-reduced $\mathbf{RuP^{2+}}$ resulting in a Stark effect. The hole conductivity behavior of *a*-TiO_2 has been observed electrochemically,[21] but the mechanism for the appearance of these holes is still debated. Here, we describe the effect of the *a*-TiO_2 overlayers on interfacial dynamics for the light-harvesting chromophore, $\mathbf{RuP^{2+}}$, surface-bound to both TiO_2 and ZrO_2, and describe a the mechanism for photo-generated hole production in these overlayers.

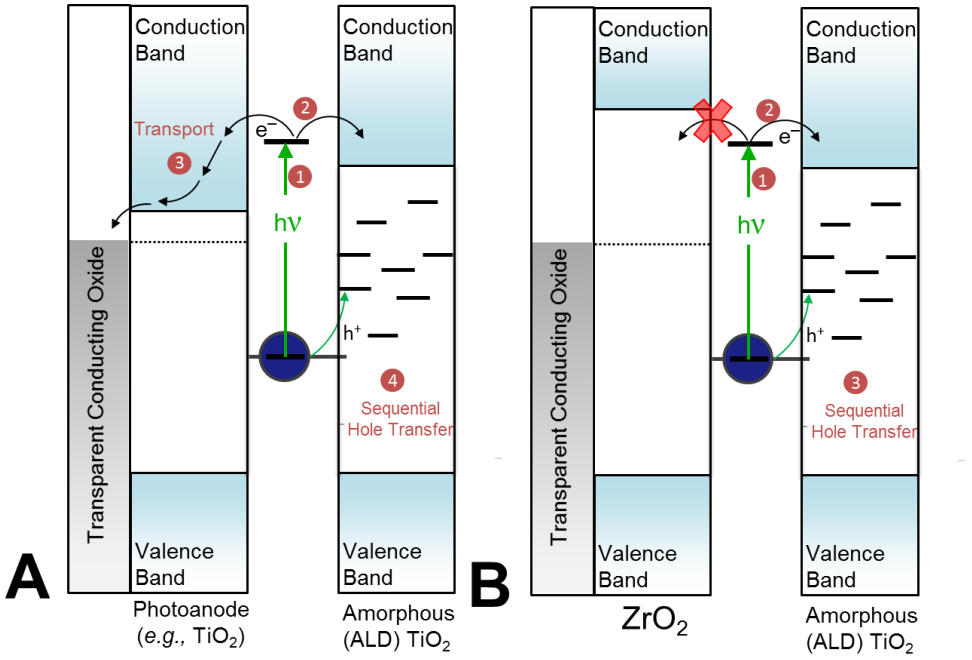

Figure 5.2. (A) Illustration of the photon initiated excitation and competitive injection processes in TiO_2|**RuP^{2+}**|xc-*a*-TiO_2. (B) Illustration of photon initiated processes in ZrO_2|**RuP^{2+}**|xc-*a*-TiO_2 without electron injection into ZrO_2.

5.2. Experimental Methods.

5.2.1. Materials and Molecular Synthesis.

The chromophore ($[Ru^{II}(bpy)_2(4,4'\text{-}(PO_3H_2)_2bpy)](Cl)_2$: **RuP^{2+}**) was synthesized by previously reported procedures,[4] as were ZrO_2[24] and TiO_2[25] nanoparticle films. Nanoparticle films were soaked in a 1 mM solution of **RuP^{2+}** dissolved in methanol in the dark overnight then soaked in methanol to remove any aggregate dyes and dried under a stream of air. Thin overlayers of titanium dioxide (*a*-TiO_2) were deposited on dyed TiO_2 and ZrO_2 films with atomic layer deposition (ALD).

5.2.2. Atomic Layer Deposition.

Atomic layer deposition (ALD) was performed by using a Cambridge NanoTech Savannah ALD system located in the Chapel Hill Analytical and Nanofabrication Lab (CHANL) cleanroom. The TiO_2 precursor (tetrakis(dimethylamido)titanium(IV) (TiTDMA)) cylinder was heated at 75°C, while the reaction chamber was set to 150°C. The chamber and cylinder were heated at temperature for at least 1 hour prior to deposition. The dyed and undyed nanoparticle films were added to the center of the reaction chamber, in line with the precursor inlet and outlet ports. The samples were placed under dynamic vacuum with continuous nitrogen purge (99.999%, further purified using an Entegris GateKeeper Inert Gas Purifier) at temperature (150°C) for at least 10 minutes prior to deposition. Deposition was performed with the chamber containing precursor isolated from vacuum ("exposure mode"). TiTDMA was pulsed for 2 seconds, isolated in the chamber for 20 seconds, purged from the chamber for 60 seconds. Water was pulsed for 20 ms, isolated for 20 seconds and purged for 60 seconds. A number of cycles were used to control the thickness of the deposited layer, where one cycle of TiTDMA was followed by water. A piece of planar, witness Si present in the reactor during ALD was used to determine the thickness of the deposited TiO_2 layer through performing ellipsometry on an Angle Spectroscopic Ellipsometer.

5.2.3. Sample Prep for Transient Absorption.

Prior to transient absorption, films were submerged in 0.1 M HClO4 aqueous solutions in a 10 mm path cuvette at a 45° angle. The cuvette was fitted with an O-ring seal and Kontes valve inlet to purge the sample with argon for at least 45 min prior to TA measurements to prevent effects from the presence of oxygen.

5.2.4. UV-Visible Absorption Spectroscopy.

UV-Visible absorption spectra were collected by using a UV-Visible-NIR absorption spectrophotometer (Agilent Technologies, model 8453A) operated with tungsten and deuterium lamps. The baseline as the absorption spectrum of air. Absorption spectra of electrodes were collected by placing samples perpendicular to the beam path. The integration time was 0.5 s.

5.2.5. Femtosecond Transient Absorption Spectroscopy.

Femtosecond transient absorption spectra were collected in a pump-probe configuration with a 1 kHz Ti:Sapphire chirped pulse amplifier (Clark-MXR CPA-2001). The 388 nm pump pulse was generated via second harmonic generation of the 775 nm regenerative amplifier output. Alternatively, 490 nm pump pulses were generated via sum frequency generation of a portion of the 775 nm output and the signal (~1200 nm) generated from a home-built optical parametric amplifier (OPA). The white-light probe (340-800 nm) is created by focusing a portion of the 775 nm output into a translating CaF_2 window. The probe polarization is set to horizontal and the pump, chopped at 500 Hz, was set to magic angle (~54.7°). The probe was delayed relative to the pump by a computer-controlled optical delay line. Pump and probe beams were focused to ~150 μm and spatially overlapped at the sample. White light difference spectra were collected by using a fiber optic-coupled multichannel spectrometer with a CMOS sensor. The sample was translated throughout the experiment by raster-scanning to ensure full relaxation between excitation pulses. The instrument response is ~250 fs FWHM with a detector sensitivity of 0.1 mOD.

5.2.6. Nanosecond-Microsecond Transient Absorption.

Nanosecond pump-probe transient absorption were taken with the same pump pulse as femtosecond transient absorption. Continuum generation in a diode-laser pumped photonic crystal fiber from Ultrafast Systems created the white light probe pulse. The probe is

electronically delayed relative to the probe pulse with a 500 ps time resolution and the maximum time delay is 400 μs.

5.2.7. Steady State Illumination Experiments.

Steady-state illumination experiments were conducted using a photostability apparatus previously reported.[19] Briefly, a Cary 50 UV-Vis spectrometer was outfitted with a Thorlabs LED (M455L3) to allow for collection of absorption spectra before, during and following illumination. UV-Vis absorption spectra of ZrO_2|**RuP^{2+}**|40c-*a*-TiO_2 in 0.1 M $HClO_4$ were taken at 20 second intervals under 455 nm (475 mW/cm^2) steady-state illumination. The baseline was the absorption spectrum of the electrode in the dark, before illumination.

5.2.8. Transflectance Measurements.

Transflectance measurements were performed using a Cary 5000 UV-Vis-NIR absorption spectrophotometer outfitted with an external diffuse reflectance accessory with clip-style, center-mount insert and small-spot kit. The system was operated in double-beam mode with all measurements, including the 100% baselines, recorded with uncalibrated PTFE reference plates installed at the reference and reflectance ports. The zero-level baseline was established by removing the PTFE plate from the reflectance port. Contributions from the metal-oxide-coated FTO electrode were subtracted from transflectance values recorded for electrodes derivatized with **RuP^{2+}**. Measurements were each the result of three scans averaged.

5.3. Results and Discussion.

5.3.1. Ground State Absorption Spectra.

Ground state absorption profiles of nanocrystalline TiO_2 are shown in Figure 5.3. Nanocrystalline TiO_2 is transparent in the visible with a sharp absorption onset at ~380 nm corresponding to the CB energy. TiO_2|40c-*a*-TiO_2, where deposition of 40 cycles (40c)

corresponds to 2 nm of *a*-TiO_2, has a low energy absorption feature through ~500 nm.[23] Simultaneous appearance of a sharp feature at ~400 nm suggests an increase in the number of transitions at varying energies due to filled defect states within the band gap. Adsorption of **RuP^{2+}** on the TiO_2 surface results in a broad metal-to-ligand charge transfer (MLCT) band centered ~460 nm. With increasing cycles of the *a*-TiO_2 overlayer, with 10 cycles and 20 cycles corresponding to 0.4 nm and 1 nm respectively, the **RuP^{2+}** absorption slightly red shifts and broadens on the red edge due to the overlayer presence. ZrO_2 films exhibit a similar behavior with a larger red shift in the **RuP^{2+}** absorption maximum as the overlayer is increased. To avoid direct excitation of the *a*-TiO_2 overlayer, and to selectively excite **RuP^{2+}**, a pump wavelength of 490 nm was used for transient absorption experiments.

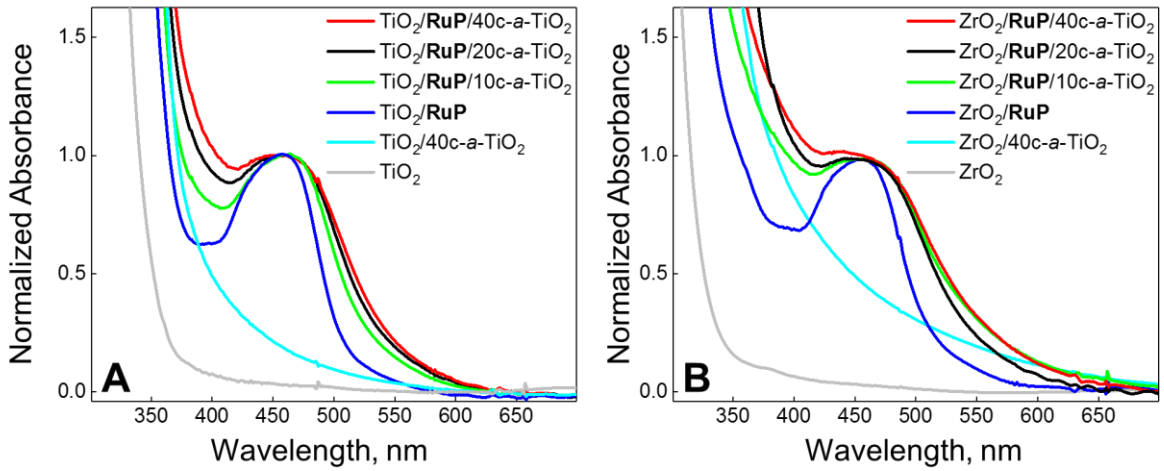

Figure 5.3. Normalized ground-state absorption spectra of: (A) TiO_2 (grey), TiO_2|40c-*a*-TiO_2 (light blue), TiO_2|**RuP^{2+}** (blue), TiO_2|**RuP^{2+}**|10c-*a*-TiO_2 (green), TiO_2|**RuP^{2+}**|20c-*a*-TiO_2 (black), TiO_2|**RuP^{2+}**|40c-*a*-TiO_2 (red) and **B**. ZrO_2 (grey), ZrO_2|40c-*a*-TiO_2 (light blue), ZrO_2|**RuP^{2+}** (blue), ZrO_2|**RuP^{2+}**|10c-*a*-TiO_2 (green), ZrO_2|**RuP^{2+}**|20c-*a*-TiO_2 (black), ZrO_2|**RuP^{2+}**|40c-*a*-TiO_2 (red) in degassed 0.1 M $HClO_4$ (aq).

5.3.2. Excited State Decay vs. Electron Injection.

Visible excitation of the dye, $\mathbf{RuP^{2+}}$, creates an MLCT excited state ($\mathbf{RuP^{2+*}}$) (Figure 5.4). The transient absorption spectrum of ZrO_2|$\mathbf{RuP^{2+*}}$ (Figure 5.4A), following 490 nm excitation, includes features characteristic of the MLCT excited state with a ground state bleach (GSB) at 460 nm, and excited state absorptions (ESA) corresponding to π-π* transitions in the near-UV at 380 nm, and at λ > 500 nm due to a low intensity dπ-dπ*absorption at Ru(II). No charge injection occurs in ZrO_2|$\mathbf{RuP^{2+*}}$ with the excited state decaying on the order of hundreds of nanoseconds.[19]

The initial transient absorption spectrum for TiO_2|$\mathbf{RuP^{2+*}}$ is similar to ZrO_2|$\mathbf{RuP^{2+*}}$ at early times (Figure 5.4B). As pump-probe delay increases, the initial excited state decays rapidly without loss of the GSB amplitude, consistent with electron injection to give $TiO_2(e^-)$|$\mathbf{RuP^{3+}}$ with injection complete by 1.2 ns (Figure 5.4B, dark red).[22-23] Following injection, back electron transfer occurs to give $\mathbf{RuP^{2+}}$ on a time scale of microseconds.[26]

$$y = Offset + A_1 e^{-x/\tau_1} + A_2 e^{-x/\tau_2} \qquad (5.11)$$

Table 5.1. Results of fit (eq. 5.11) to decay traces at 380 nm for TiO_2|**RuP**|xc-*a*-TiO_2.

TiO_2	**No ALD (0c)**	**5c**	**10c**	**20c**	**40c**
Offset	32%	22%	21%	10%	14%
A_1	44%	28%	36%	18%	35%
τ_1, ps	12.8	0.95	2.7	1.2	1.8
A_2	24%	50%	43%	72%	51%
τ_2, ps	137	102	70	19	25

We can qualitatively estimate the injection efficiency through analysis of the relative amplitudes of features in the transient spectra.[22] Based on variations in amplitude differences at

380 nm in the $bpy^{\bullet-}$ ESA of $\mathbf{RuP^{2+*}}$ on ZrO_2 and TiO_2, we estimate that around ~45% of the injection events in TiO_2 occur within 2 ps following photoexcitation with slower injection responsible for the remaining 55% of the excited state.. On the picosecond timescale, loss of the excited state is biexponential with time constants of 12.8 ps and 137 ps (Table 5.1).

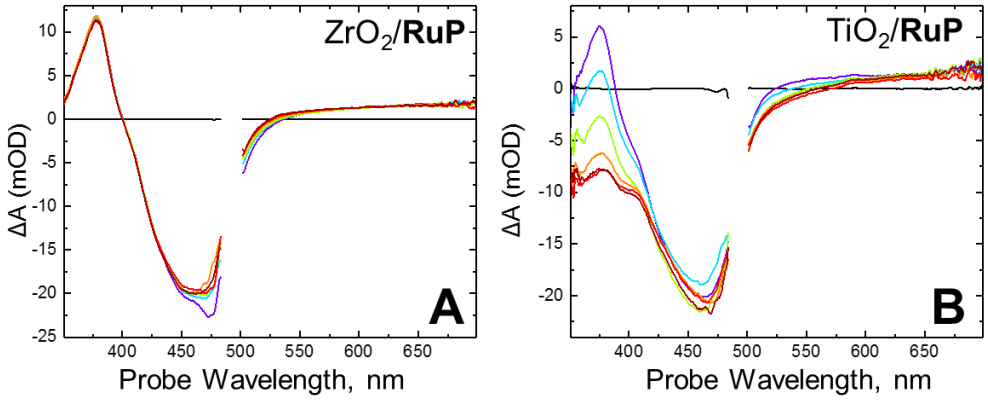

Figure 5.4. Transient absorption spectra of (A) ZrO_2|$\mathbf{RuP^{2+}}$and (B) TiO_2|$\mathbf{RuP^{2+}}$, following 490 nm excitation (100 nJ/pulse) in degassed 0.1 M $HClO_4$ (aq) at probe delays of -6 (black), 2 (purple), 10 (blue), 50 (green), 200 (orange), 500 (red), and 1200 (dark red) ps.

Control experiments on ZrO_2|40c-*a*-TiO_2 and TiO_2|40c-*a*-TiO_2 with no added dye excited at 388 nm were used to explore possible contributions to the spectrum from the *a*-TiO_2 overlayer (Figure 5.5). From the ground state absorption spectrum in Figure 5.3, excitation at 388 nm selectively excites the *a*-TiO_2 overlayer without excitation of the nanocrystalline films. Excitation of the *a*-TiO_2 layer results in a broad absorption throughout the visible with evidence for a collection of discrete states. The overall absorption manifold decays in 100s of picoseconds in ZrO_2|40c-*a*-TiO_2 and persists for over 1 nanosecond in the TiO_2|40c-*a*-TiO_2 case. The appearance of the absorption manifold is consistent with a broadly-based series of transitions in the near UV. Upon excitation, they result in the formation of transient, intermediate states that

are able to inject into the nanocrystalline TiO_2 creating a CSS that is not thermodynamically feasible in ZrO_2|40c-*a*-TiO_2. This suggests that the broad absorption is due to holes in the mid-gap region in the *a*-TiO_2 films. It is important to note that 490 nm excitation of these undyed films does not induce any absorption changes in this region.[23]

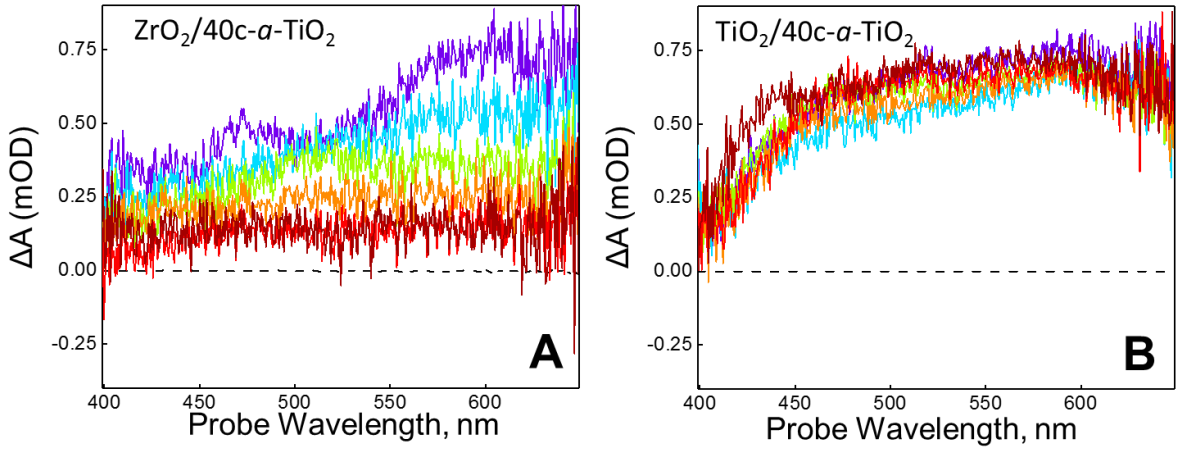

Figure 5.5. Transient absorption spectra of (A) ZrO_2|40c-*a*-TiO_2 and (B) TiO_2|40c-*a*-TiO_2 films photoexcited at 388 nm (400 nJ/pulse) in degassed 0.1 M $HClO_4$ (aq) at pump-probe delays of 1 (purple), 15 (blue), 50 (green), 125 (orange), 400 (red), 1100 (dark red) ps.

5.3.3. Charge Separation Dynamics of TiO_2|RuP^{2+}|*a*-TiO_2.

As observed by transient absorption spectral changes, addition of *a*-TiO_2 overlayers on films of TiO_2|**RuP**$^{2+}$ changes their photophysical behavior (Figure 5.6). With 5 cycles (0.2 nm) of *a*-TiO_2 (TiO_2|**RuP**$^{2+}$|5c-*a*-TiO_2), the same **RuP**$^{2+}$ excited state features appear but the ground state bleach decays on the picosecond time scale. The decay kinetics for TiO_2|**RuP**$^{2+}$|5c-*a*-TiO_2 at 380 nm (Table 5.1) are biexponential with rapid (τ_1 = 0.95 ps) and slow (τ_2 = 102 ps) components, which are slightly faster than TiO_2|**RuP**$^{2+}$ alone. This trend continues as more cycles of *a*-TiO_2 are added, where the ESA decay of TiO_2|**RuP**$^{2+}$|40c-*a*-TiO_2 has time components of 1.8 ps and

25 ps. A faster injection rate is expected in these systems, as the *a*-TiO_2 overlayer introduces additional acceptor states for the **RuP**$^{2+}$ to inject into, consistent with observations from a systematic study of injection into TiO_2 with varying Ru(II) dyes.[22]

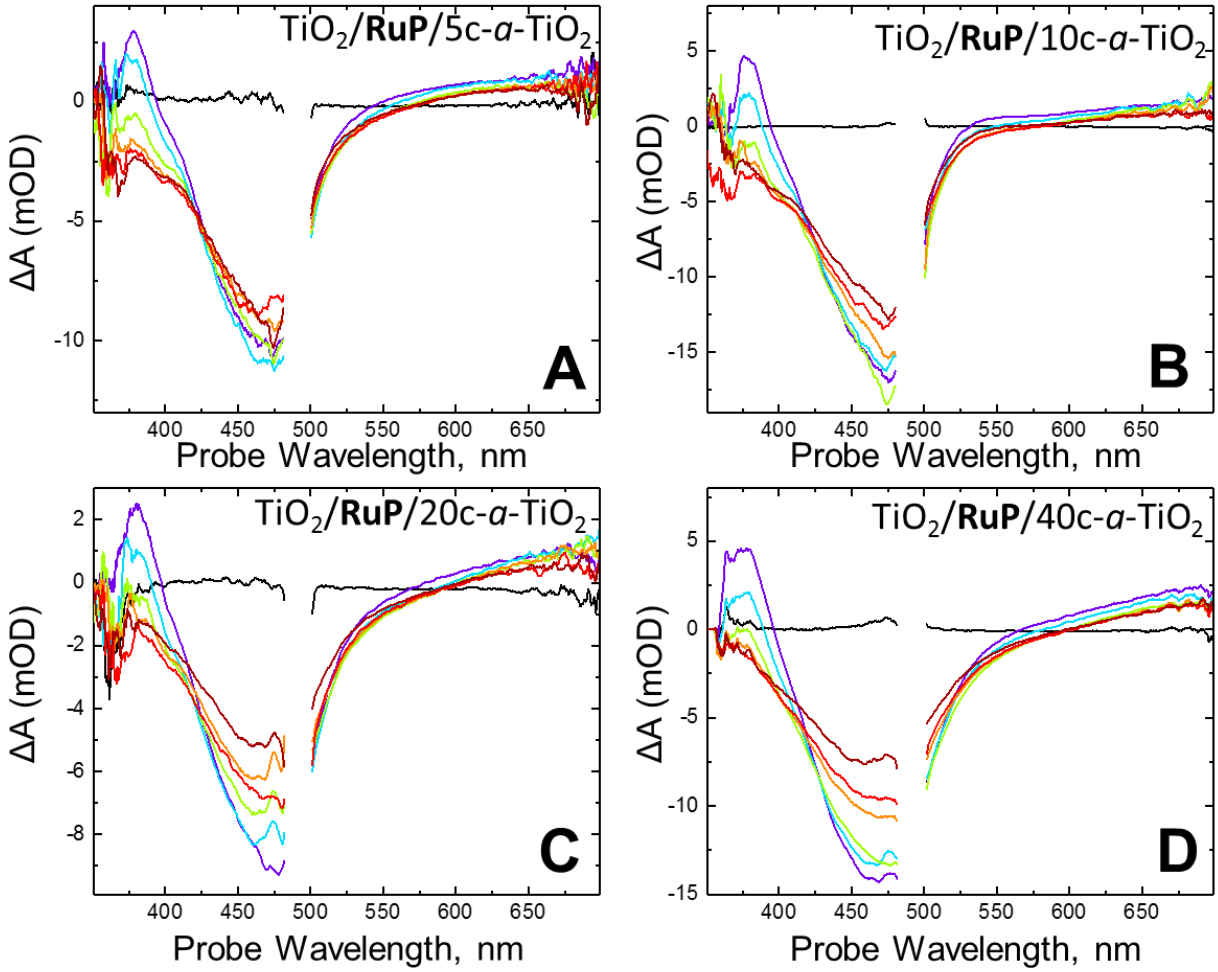

Figure 5.6. Transient absorption spectra of (A) TiO_2|**RuP**$^{2+}$|5c-*a*-TiO_2, (B) TiO_2|**RuP**$^{2+}$|10c-*a*-TiO_2 (C) TiO_2|**RuP**$^{2+}$|20c-*a*-TiO_2 and (D) TiO_2|**RuP**$^{2+}$|40c-*a*-TiO_2 in 0.1 M $HClO_4$ (aq) photoexcited at 490 nm (100 nJ/pulse) at pump-probe delays -6 (black), 2 (purple), 10 (blue), 50 (green), 200 (orange), 500 (red), 1200 (dark red) ps.

Compared to TiO_2|**RuP**$^{2+}$, determination of the qualitative injection yield is more difficult because the loss of the GSB amplitude manifests in the near-UV, as the oxidized chromophore **RuP**$^{3+}$ is lost. The decay of the GSB, monitored at 460 nm, in TiO_2|**RuP**$^{2+}$|5c-TiO_2 is exponential with a lifetime of 215 ps (Table 5.2). The change in amplitude in the overall TA signal represents a loss of ~30% of the oxidized chromophores. The origin of this loss is likely due to reduction of the oxidized chromophores from filled defect states in the *a*-TiO_2 shell (Eq.5.7, $TiO_2(e^-)$|**RuP**$^{3+}$|*a*-TiO_2 → $TiO_2(e^-)$|**RuP**$^{2+}$|*a*-$TiO_2(h^+)$). The injected electrons may still be in the nanocrystalline TiO_2; however, because we are monitoring the transient absorption signal from just the chromophore, it is difficult to pinpoint the exact location of the injected electrons. This type of recombination is non-geminate as the electron reducing **RuP**$^{3+}$ is not the same electron that has been injected into the CB of either the TiO_2 or *a*-TiO_2 overlayer.

$$y = Offset + A_1 e^{-x/\tau_1} \qquad (5.12)$$

Table 5.2. Exponential fit (eq. 5.12) of GSB decay kinetics (λ_{probe} = 460 nm) for TiO_2/**RuP**/xc-*a*-TiO_2.

TiO_2	**5c**	**10c**	**20c**	**40c**
Offset	77%	70%	56%	50%
A_1	23%	30%	44%	50%
τ_1, ps	215	305	208	175

With increasing *a*-TiO_2 overlayer thickness, the magnitude of the GSB loss increases from 30% in TiO_2|**RuP**$^{2+}$|5c-*a*-TiO_2 to 50% in TiO_2|**RuP**$^{2+}$|40c-*a*-TiO_2. The time scale for this loss is independent of overlayer thickness at ~250 ps (Table 5.2). The film thickness result is consistent with observations made earlier on ultrafast recombination on SnO_2/*a*-TiO_2 films,[23] where the *a*-TiO_2 was deposited as a shell on a nanocrystalline core with **RuP**$^{2+}$ adsorbed to the *a*-TiO_2 shell surface.

Additionally, there is a broad absorption in the red for TiO_2|**RuP^{2+}**|20c-*a*-TiO_2 and TiO_2|**RuP^{2+}**|40c-*a*-TiO_2, similar to the absorption observed for TiO_2|40c-*a*-TiO_2 (Figure 5.5B). The band shape is distinctly different from characteristic Ru(II) absorptions, and likely arises from holes in the *a*-TiO_2 overlayer, consistent with reduction of oxidized chromophores occurring through filled defect states in the overlayer.

5.3.4. Charge Separation Dynamics of ZrO_2|**RuP^{2+}**|*a*-TiO_2.

The transient absorption spectra of ZrO_2|**RuP^{2+}**|5c-*a*-TiO_2 after 490 nm photoexcitation is shown in Figure 5.7A. Both the bpy$^{\bullet-}$ ESA and the GSB decay on the picosecond time scale suggesting a mechanism other than excited state decay is occurring. The spectral features for ZrO_2|**RuP^{2+}**|10c-*a*-TiO_2 include a growth of a positive signal in the red, and a shift in the bleach from 460 nm to 475 nm. This red shift is progressive, increasing with overlayer thickness, and reaches ~50 nm in ZrO_2|**RuP^{2+}**|40c-*a*-TiO_2. This red shift is not present for the analogous TiO_2 film.

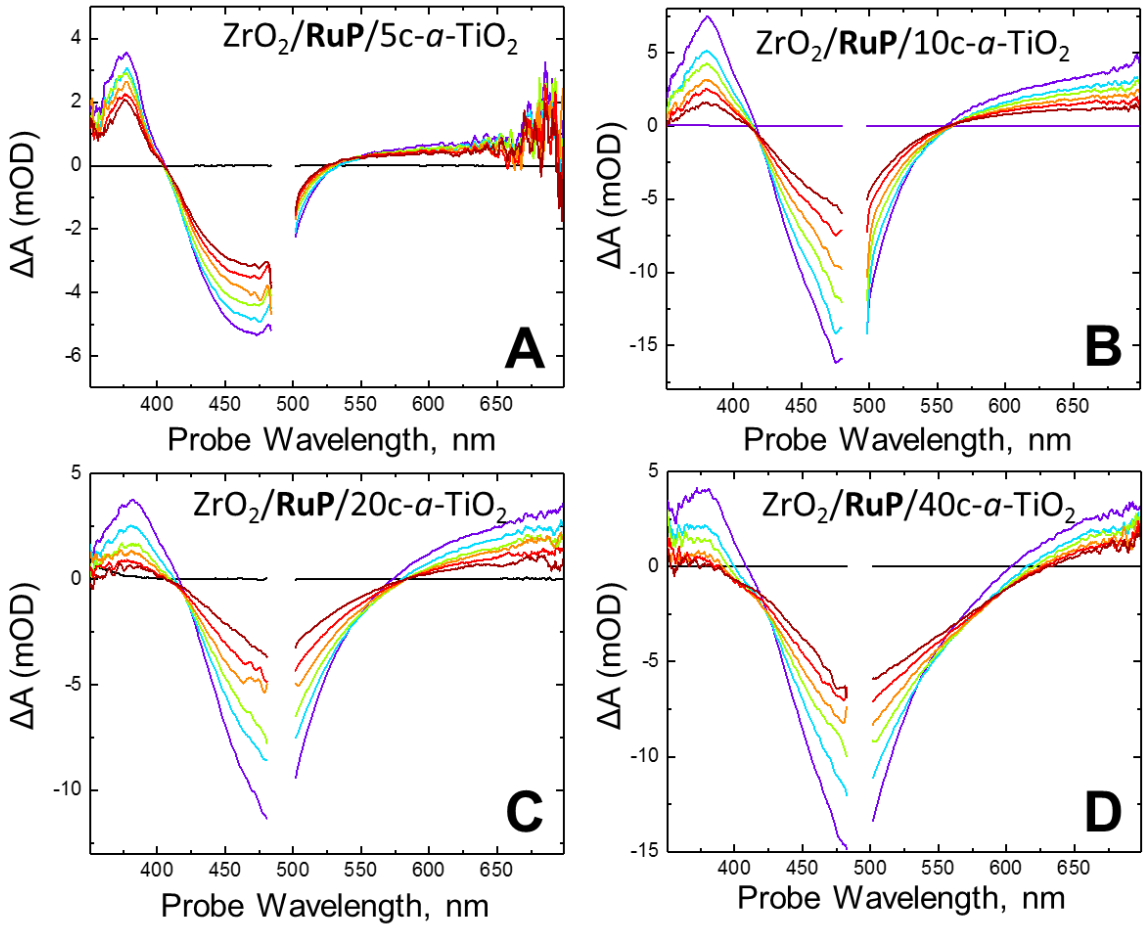

Figure 5.7. Transient absorption spectra of (A) ZrO_2|**RuP**$^{2+}$|5c-*a*-TiO_2, (B) ZrO_2|**RuP**$^{2+}$|10c-*a*-TiO_2, (C) ZrO_2|**RuP**$^{2+}$|20c-*a*-TiO_2, (D) ZrO_2|**RuP**$^{2+}$|40c-*a*-TiO_2 photoexcited at 490 nm (100 nJ/pulse) in 0.1 M $HClO_4$ (aq) at pump-probe delays of -6 (black), 2 (purple), 10 (blue), 50 (green), 200 (orange), 500 (red), 1200 (dark red) ps.

The decay kinetics for the bpy$^{\bullet-}$ band at 380 nm were fit to a single exponential for ZrO_2|**RuP**$^{2+}$|5c-*a*-TiO_2 and to a biexponential equation for all other ZrO_2|**RuP**$^{2+}$|xc-*a*-TiO_2 films to determine the time scales for injection into the *a*-TiO_2 overlayer (Table 5.3). For ZrO_2|**RuP**$^{2+}$|5c-*a*-TiO_2, it is clear that some injection is occurring with a time constant of 92 ps. This film is an outlier because only a small amount of injection is occurring and it is difficult to

resolve a fast and slow component in this case. With thicker overlayers, we observe typical biphasic injection kinetics that become faster as thickness increases from 10.3 ps and 278 ps in ZrO_2|**RuP^{2+}**|10c-*a*-TiO_2 to 3.9 ps and 111 ps in ZrO_2|**RuP^{2+}**|40c-*a*-TiO_2, consistent with an increase in *a*-TiO_2 acceptor states.

Table 5.3 Fit of ESA kinetics (λ_{probe} = 380 nm) with eq. 5.11 for ZrO_2|**RuP^{2+}**|5c-*a*-TiO_2

ZrO_2	**5c**	**10c**	**20c**	**40c**
Offset	66%	3%	3%	2%
A_1	34%	44%	54%	39%
τ_1, ps	92	10.3	17.8	3.9
A_2		53%	43%	59%
τ_2, ps		278	237	111

Loss of the ground state bleach at 460 nm (Table 5.4) occurs on a similar time scale as the loss of the bpy$^{\bullet-}$ band. This similarity suggests that in these films recombination immediately follows the injection process. Additionally, the blue edge of the bleach (λ = 460 nm) decays faster than the red edge (λ = 525 nm), where for ZrO_2|**RuP^{2+}**|40c-*a*-TiO_2, the fast and slow components for the red edge of the bleach are 52 ps and 472 ps, due to this progressive red shift that increases with increasing pump-probe delay.

Table 5.4. Fit of GSB kinetics (λ_{probe} = 460 nm) with eq. 5.11 for ZrO_2|**RuP^{2+}**|xc-*a*-TiO_2 (10c-40c) and eq. 5.12. for ZrO_2|**RuP^{2+}**|5c-*a*-TiO_2

ZrO_2	**5c**	**10c**	**20c**	**40c**
Offset	63%	33%	33%	40%
A_1	37%	22%	22%	20%
τ_1, ps	126	14.2	6.4	4.5
A_2		45%	45%	40%
τ_2, ps		283	190	163

5.3.5. Spectral Modeling in ZrO_2|RuP^{2+}|40c-*a*-TiO_2.

The shape and behavior of features in the ZrO_2|**RuP^{2+}**|xc-*a*-TiO_2 transient absorption spectra are atypical of surface-bound **RuP^{2+}**. To simulate the early time spectrum at 1 ps of ZrO_2|**RuP^{2+}**|xc-*a*-TiO_2, we need a linear combination of spectral components (Figure 5.8A), including the 1st derivative of the ground state absorption using transflectance measurements to eliminate scatter, the excited state spectrum of surface bound **RuP^{2+*}** (Figure 5.4A, ZrO_2|**RuP^{2+*}**), and the hole absorption in the *a*-TiO_2 overlayer (Figure 5.5A). The late time spectrum at 1 ns of ZrO_2|**RuP^{2+}**|40c-*a*-TiO_2 (Figure 5.7B) has a similar linear combination including the hole in the *a*-TiO_2 overlayer, and some contribution from the excited state (for ZrO_2|**RuP^{2+*}**); however, the 1st derivative no longer adequately describes the spectrum. Instead, we collected UV-Vis spectra under 450 nm steady state illumination and used the difference spectrum between dark and light conditions in the simulated sum to accurately describe the transient absorption spectrum at 1 ns. Similar results are obtained by shifting the absorption spectrum ~30 nm and taking the difference between the original (measured) position and the shifted spectrum.

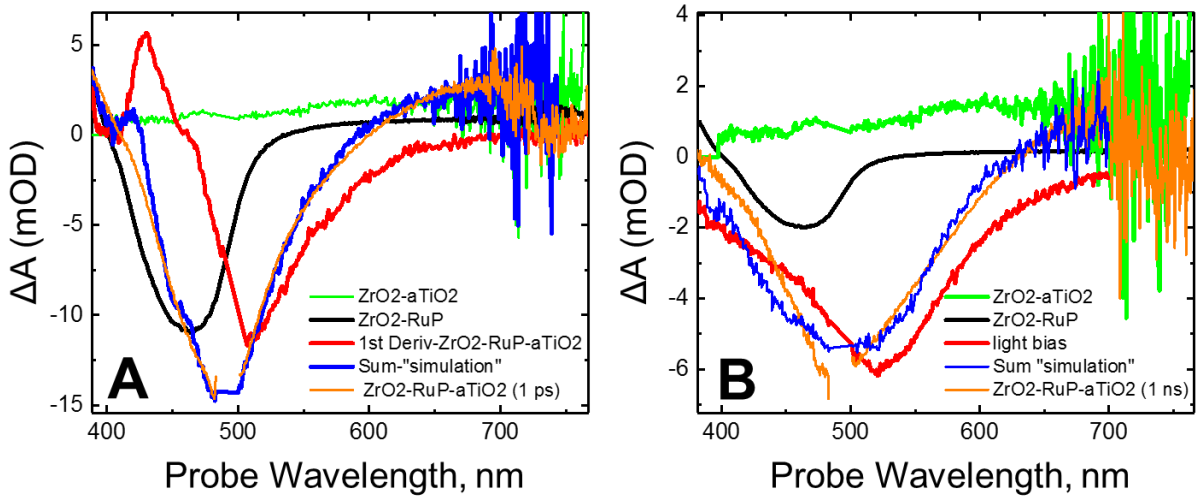

Figure 5.8. (A) Components and weighted simulated sum of the 1 ps transient absorption spectrum of ZrO_2|**RuP**$^{2+}$|40c-*a*-TiO_2 (orange) where the first derivative spectrum of the ground state from transflectance measurements (red), excited state of surface-bound **RuP**$^{2+*}$ (ZrO_2|**RuP**$^{2+*}$, black), and the hole in the *a*-TiO_2 film (green) are added together in a linear combination to produce the simulated spectrum (blue). (B) Components and weighted simulated sum of the 1 ns transient absorption spectrum of ZrO_2|**RuP**$^{2+}$|40c-*a*-TiO_2 (orange) where the difference spectrum of the ground state and illuminated film (red), excited state of surface-bound **RuP**$^{2+*}$ (ZrO_2|**RuP**$^{2+*}$, black), and the hole in the *a*-TiO_2 film (green) are added together in a linear combination to produce the simulated spectrum (blue).

The 1st derivative is often used in modeling to describe the changes to a spectrum due to a Stark effect, or the effects due to an electric field.[27] The electric field in the ZrO_2|**RuP**$^{2+}$|xc-*a*-TiO_2 films arises from injection from photoexcited **RuP**$^{2+*}$ into the CB-like states in the *a*-TiO_2 overlayer creating an oxidized **RuP**$^{3+}$. The oxidized **RuP**$^{3+}$ is reduced by a filled defect state in the *a*-TiO_2 overlayer recreating **RuP**$^{2+}$, and leaving a higher energy electron and a hole in the *a*-

TiO_2 overlayer, changing the environment around the $\mathbf{RuP^{2+}}$ and shifting its absorption to lower energies. Recalling equations 5.8-5.10:

$$ZrO_2/\mathbf{RuP^{2+}}/a\text{-}TiO_2 + h\nu \rightarrow ZrO_2/\mathbf{RuP^{2+*}}/a\text{-}TiO_2 \quad (5.8)$$

$$ZrO_2/\mathbf{RuP^{2+*}}/a\text{-}TiO_2 \rightarrow ZrO_2/\mathbf{RuP^{3+}}/a\text{-}TiO_2\,(e^-) \quad (5.9)$$

$$ZrO_2/\mathbf{RuP^{3+}}/a\text{-}TiO_2\,(e^-) \rightarrow ZrO_2/\mathbf{RuP^{2+}}/a\text{-}TiO_2\,(e^-\text{-}h^+) \quad (5.10)$$

This process continues through the picosecond timescale, further perturbing the spectrum to lower energies. The relative contribution of the generated holes in the *a*-TiO_2 overlayer increases with time, while excited state contributions ($ZrO_2|\mathbf{RuP^{2+*}}$), decreases. Additionally, we would expect the electric field signal to simply increase in intensity as the concentration of $\mathbf{RuP^{2+}}$ increased; however, this continued red shift in the GSB with increasing pump-probe delay may be indicative of mobile electrons[28] undergoing a random walk through localized states at differing energies in this amorphous overlayer.[29] The magnitude of this electric field is larger for $ZrO_2|\mathbf{RuP^{2+}}|$xc-*a*-TiO_2 because all charges are localized in the *a*-TiO_2 overlayer, where in the $TiO_2|\mathbf{RuP^{2+}}|$xc-*a*-TiO_2 case, the injected electron can move throughout the nanocrystalline TiO_2 film in addition to the *a*-TiO_2 overlayer.

The behavior on both $ZrO_2|\mathbf{RuP^{2+}}|$xc-*a*-TiO_2 and $TiO_2|\mathbf{RuP^{2+}}|$xc-*a*-TiO_2 point to an ultrafast loss of oxidized chromophores via reduction by filled defect states in the mid-gap region of the *a*-TiO_2 overlayer. Our group has also observed a similar ultrafast loss from this amorphous TiO_2 on SnO_2/*a*-TiO_2 core/shell films; however, it was difficult to determine the origin. The observations in this study suggest that the loss of oxidized chromophores we observed in the SnO_2/*a*-TiO_2 is, in fact, non-geminate in nature, where the injected electron is not the same electron reducing the oxidized chromophore.

5.4. Conclusions.

The interfacial dynamics of dye-sensitized nanocrystalline films "buried" with varying thicknesses of an amorphous TiO_2 overlayer were investigated using transient absorption spectroscopy. On TiO_2|**RuP**$^{2+}$|xc-*a*-TiO_2 films, we observe an ultrafast loss component (τ~250 ps) consistent with what has been measured for dye-sensitized SnO_2/*a*-TiO_2 core/shell films. On ZrO_2|**RuP**$^{2+}$|xc-*a*-TiO_2, where the only path for electron injection is into the *a*-TiO_2 overlayer, we observe a transient Stark effect from an electric field produced by reduction of oxidized chromophores via filled defect states in the *a*-TiO_2 after injection into higher energy, empty *a*-TiO_2 states. We are able to simulate the spectrum using a linear combination of the hole absorption in the *a*-TiO_2 film, the excited state of **RuP**$^{2+*}$, and the difference spectrum of the red-shifted ground state represented by the 1st derivative curve at early times and the difference spectrum under steady state illumination at 1 ns. The mechanism of chromophore regeneration uncovered in this study could be exploited successfully in DSPEC devices, where the holes in the *a*-TiO_2 overlayer can be transported to a catalyst, while also resetting the chromophore to undergo the next light absorption/injection event.

REFERENCES

1. Brennaman, M. K.; Dillon, R. J.; Alibabaei, L.; Gish, M. K.; Dares, C. J.; Ashford, D. L.; House, R. L.; Meyer, G. J.; Papanikolas, J. M.; Meyer, T. J. Finding the Way to Solar Fuels with Dye-Sensitized Photoelectrosynthesis Cells. *J. Am. Chem. Soc.* **2016,** *138* (40), 13085-13102.

2. Ashford, D. L.; Gish, M. K.; Vannucci, A. K.; Brennaman, M. K.; Templeton, J. L.; Papanikolas, J. M.; Meyer, T. J. Molecular Chromophore-Catalyst Assemblies for Solar Fuel Applications. *Chem. Rev.* **2015,** *115* (23), 13006-13049.

3. Concepcion, J. J.; House, R. L.; Papanikolas, J. M.; Meyer, T. J. Chemical Approaches to Artificial Photosynthesis. *Proc. Natl. Acad. Sci. U. S. A.* **2012,** *109* (39), 15560-15564.

4. Norris, M. R.; Concepcion, J. J.; Glasson, C. R. K.; Fang, Z.; Lapides, A. M.; Ashford, D. L.; Templeton, J. L.; Meyer, T. J. Synthesis of Phosphonic Acid Derivatized Bipyridine Ligands and Their Ruthenium Complexes. *Inorg. Chem.* **2013,** *52* (21), 12492-12501.

5. She, C. X.; Guo, J. C.; Irle, S.; Morokuma, K.; Mohler, D. L.; Zabri, H.; Odobel, F.; Youm, K. T.; Liu, F.; Hupp, J. T., et al. Comparison of Interfacial Electron Transfer through Carboxylate and Phosphonate Anchoring Groups. *J. Phys. Chem. A* **2007,** *111* (29), 6832-6842.

6. Wang, L.; Ashford, D. L.; Thompson, D. W.; Meyer, T. J.; Papanikolas, J. M. Watching Photoactivation in a Ru(II) Chromophore-Catalyst Assembly on TiO_2 by Ultrafast Spectroscopy. *J. Phys. Chem. C* **2013,** *117* (46), 24250-24258.

7. Ashford, D. L.; Stewart, D. J.; Glasson, C. R.; Binstead, R. A.; Harrison, D. P.; Norris, M. R.; Concepcion, J. J.; Fang, Z.; Templeton, J. L.; Meyer, T. J. An Amide-Linked Chromophore-Catalyst Assembly for Water Oxidation. *Inorg. Chem.* **2012,** *51* (12), 6428-6430.

8. Ashford, D. L.; Song, W. J.; Concepcion, J. J.; Glasson, C. R. K.; Brennaman, M. K.; Norris, M. R.; Fang, Z.; Templeton, J. L.; Meyer, T. J. Photoinduced Electron Transfer in a Chromophore-Catalyst Assembly Anchored to TiO2. *J. Am. Chem. Soc.* **2012,** *134* (46), 19189-19198.

9. Ryan, D. M.; Coggins, M. K.; Concepcion, J. J.; Ashford, D. L.; Fang, Z.; Alibabaei, L.; Ma, D.; Meyer, T. J.; Waters, M. L. Synthesis and Electrocatalytic Water Oxidation by Electrode-Bound Helical Peptide Chromophore-Catalyst Assemblies. *Inorg. Chem.* **2014,** *53* (15), 8120-8128.

10. Bettis, S. E.; Ryan, D. M.; Gish, M. K.; Alibabaei, L.; Meyer, T. J.; Waters, M. L.; Papanikolas, J. M. Photophysical Characterization of a Helical Peptide Chromophore-Water Oxidation Catalyst Assembly on a Semiconductor Surface using Ultrafast Spectroscopy. *J. Phys. Chem. C* **2014,** *118* (12), 6029-6037.

11. Song, W. J.; Ito, A.; Binstead, R. A.; Hanson, K.; Luo, H. L.; Brennaman, M. K.; Concepcion, J. J.; Meyer, T. J. Accumulation of Multiple Oxidative Equivalents at a Single Site by Cross-Surface Electron Transfer on TiO2. *J. Am. Chem. Soc.* **2013,** *135* (31), 11587-11594.

12. Gao, Y.; Ding, X.; Liu, J. H.; Wang, L.; Lu, Z. K.; Li, L.; Sun, L. C. Visible Light Driven Water Splitting in a Molecular Device with Unprecedentedly High Photocurrent Density. *J. Am. Chem. Soc.* **2013,** *135* (11), 4219-4222.

13. Leem, G.; Sherman, B. D.; Burnett, A. J.; Morseth, Z. A.; Wee, K. R.; Alibabaei, L.; Papanikolas, J. M.; Meyer, T. J.; Schanze, K. S.; Alibabaei, L. Light-Driven Water Oxidation Using Polyelectrolyte Layer-by-Layer Chromophore-Catalyst Assemblies (vol 1, pg 339, 2016). *Acs Energy Lett* **2016,** *1* (6), 1118-1118.

14. Bettis, S. E.; Hanson, K.; Wang, L.; Gish, M. K.; Concepcion, J. J.; Fang, Z.; Meyer, T. J.; Papanikolas, J. M. Photophysical Characterization of a Chromophore/Water Oxidation Catalyst Containing a Layer-by-Layer Assembly on Nanocrystalline TiO_2 using Ultrafast Spectroscopy. *J. Phys. Chem. A* **2014,** *118* (45), 10301-10308.

15. Hanson, K.; Torelli, D. A.; Vannucci, A. K.; Brennaman, M. K.; Luo, H. L.; Alibabaei, L.; Song, W. J.; Ashford, D. L.; Norris, M. R.; Glasson, C. R. K., et al. Self-Assembled Bilayer Films of Ruthenium(II)/Polypyridyl Complexes through Layer-by-Layer Deposition on Nanostructured Metal Oxides. *Angew Chem Int Edit* **2012,** *51* (51), 12782-12785.

16. Lapides, A. M.; Ashford, D. L.; Hanson, K.; Torelli, D. A.; Templeton, J. L.; Meyer, T. J. Stabilization of a Ruthenium(II) Polypyridyl Dye on Nanocrystalline TiO_2 by an Electropolymerized Overlayer. *J. Am. Chem. Soc.* **2013,** *135* (41), 15450-15458.

17. Ashford, D. L.; Lapides, A. M.; Vannucci, A. K.; Hanson, K.; Torelli, D. A.; Harrison, D. P.; Templeton, J. L.; Meyer, T. J. Water Oxidation by an Electropolymerized Catalyst on Derivatized Mesoporous Metal Oxide Electrodes. *J. Am. Chem. Soc.* **2014,** *136* (18), 6578-6581.

18. Hyde, J. T.; Hanson, K.; Vannucci, A. K.; Lapides, A. M.; Alibabaei, L.; Norris, M. R.; Meyer, T. J.; Harrison, D. P. Electrochemical Instability of Phosphonate-Derivatized, Ruthenium(III) Polypyridyl Complexes on Metal Oxide Surfaces. *Acs Appl Mater Inter* **2015,** *7* (18), 9554-9562.

19. Hanson, K.; Brennaman, M. K.; Ito, A.; Luo, H. L.; Song, W. J.; Parker, K. A.; Ghosh, R.; Norris, M. R.; Glasson, C. R. K.; Concepcion, J. J., et al. Structure-Property Relationships in Phosphonate-Derivatized, Ru^{II} Polypyridyl Dyes on Metal Oxide Surfaces in an Aqueous Environment. *J. Phys. Chem. C* **2012,** *116* (28), 14837-14847.

20. Lapides, A. M.; Sherman, B. D.; Brennaman, M. K.; Dares, C. J.; Skinner, K. R.; Templeton, J. L.; Meyer, T. J. Synthesis, Characterization, and Water Oxidation by a Molecular Chromophore-Catalyst Assembly Prepared by Atomic Layer Deposition. The "Mummy" Strategy. *Chem. Sci.* **2015,** *6* (11), 6398-6406.

21. Hu, S.; Shaner, M. R.; Beardslee, J. A.; Lichterman, M.; Brunschwig, B. S.; Lewis, N. S. Amorphous TiO_2 Coatings Stabilize Si, GaAs, and GaP Photoanodes for Efficient Water Oxidation. *Science* **2014,** *344* (6187), 1005-1009.

22. Zigler, D. F.; Morseth, Z. A.; Wang, L.; Ashford, D. L.; Brennaman, M. K.; Grumstrup, E. M.; Brigham, E. C.; Gish, M. K.; Dillon, R. J.; Alibabaei, L., et al. Disentangling the Physical Processes Responsible for the Kinetic Complexity in Interfacial Electron Transfer of Excited Ru(II) Polypyridyl Dyes on TiO_2. *J. Am. Chem. Soc.* **2016,** *138* (13), 4426-4438.

23. Gish, M. K.; Lapides, A. M.; Brennaman, M. K.; Templeton, J. L.; Meyer, T. J.; Papanikolas, J. M. Ultrafast Recombination Dynamics in Dye-Sensitized SnO2/TiO2 Core/Shell Films. *J. Phys. Chem. Lett.* **2016,** *7* (24), 5297-5301.

24. Song, W. J.; Glasson, C. R. K.; Luo, H. L.; Hanson, K.; Brennaman, M. K.; Concepcion, J. J.; Meyer, T. J. Photoinduced Stepwise Oxidative Activation of a Chromophore-Catalyst Assembly on TiO2. *J. Phys. Chem. Lett.* **2011,** *2* (14), 1808-1813.

25. Green, A. N. M.; Palomares, E.; Haque, S. A.; Kroon, J. M.; Durrant, J. R. Charge Transport Versus Recombination in Dye-Sensitized Solar Cells Employing Nanocrystalline TiO_2 and SnO_2 Films. *J. Phys. Chem. B* **2005,** *109* (25), 12525-12533.

26. Knauf, R. R.; Brennaman, M. K.; Alibabaei, L.; Norris, M. R.; Dempsey, J. L. Revealing the Relationship between Semiconductor Electronic Structure and Electron Transfer Dynamics at Metal Oxide-Chromophore Interfaces. *J. Phys. Chem. C* **2013,** *117* (48), 25259-25268.

27. Ardo, S.; Sun, Y.; Staniszewski, A.; Castellano, F. N.; Meyer, G. J. Stark Effects after Excited-State Interfacial Electron Transfer at Sensitized TiO2 Nanocrystallites. *J. Am. Chem. Soc.* **2010,** *132* (19), 6696-6709.

28. Styers-Barnett, D. J.; Ellison, S. P.; Mehl, B. P.; Westlake, B. C.; House, R. L.; Park, C.; Wise, K. E.; Papanikolas, J. M. Exciton dynamics and biexciton formation in single-walled carbon nanotubes studied with femtosecond transient absorption spectroscopy. *J. Phys. Chem. C* **2008,** *112* (12), 4507-4516.

29. Nelson, J.; Haque, S.; Klug, D. R.; Durrant, J. R. Trap-Limited Recombination in Dye-Sensitized Nanocrystalline Metal Oxide Electrodes. *Phys Rev. B: Condens. Matter Mater. Phys.* **2001,** *63* (20), 205321.

Chapter 6: Role of Structure in Ultrafast Charge Separation and Recombination in Naphthalene Diimide End-Capped Thiophene Oligomers

This chapter presents a manuscript in preparation with co-authors: Austin L. Jones, Kirk S. Schanze, and John M. Papanikolas.

6.1. Introduction

Understanding photoinduced charge separation in organic systems provides critical insight into solar cell performance as well as fundamental biological processes like photosynthesis.[1-7] Conjugated polymers, such as poly(3-hexyl)thiophene (**pT**) are often utilized as electron donors in organic photovoltaic cells;[8] however, polymers inhibit precise synthetic control, and quantitative electron transfer (ET) studies often require a combination of experiment and expensive computational simulations.[9] Oligomers have well-defined structures combined with tunable optical properties making them effective tools to study the dynamics of conformationally flexible organic systems.[10-13] Here, we characterize the excited state and charge separation dynamics in a series of thiophene oligomers (**nT**, n = 4, 6, 8, 10, 12) with and without naphthalene diimide (**NDI**) end-caps (Figure 6.1) using transient absorption spectroscopy.

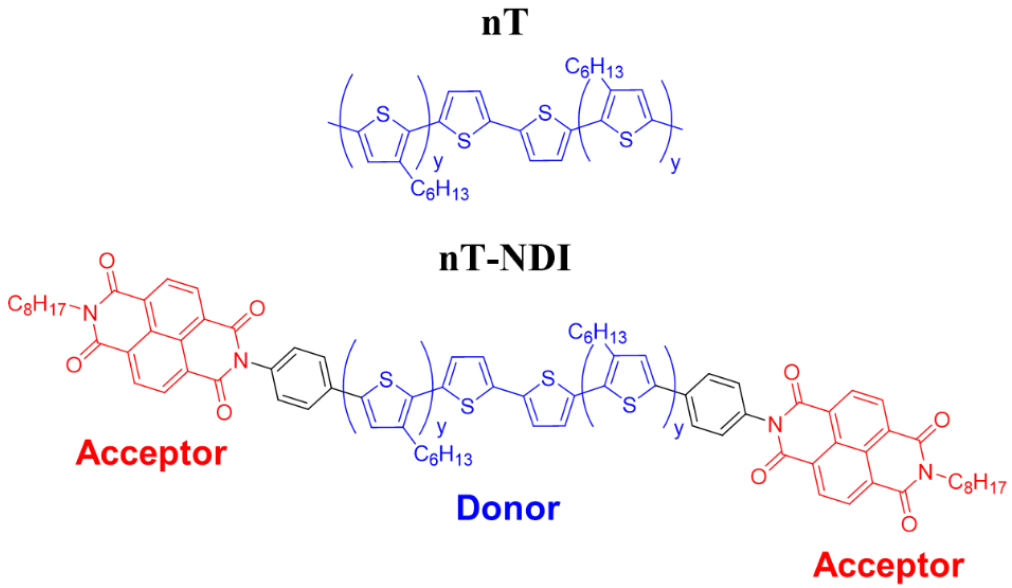

Figure 6.1. Thiophene (**nT**, Top) and donor-accepter oligomers (**nT-NDI**, Bottom) with donor colored in blue, acceptors colored in red and the phenyl bridge in black. n = 2(y+1) and y = 1, 2, 3, 4, or 5.

The π-conjugated **nT** oligomers have unique optoelectronic properties arising from the overlap of π-orbitals across the carbon-based chain.[12-13] Breaks in the π-conjugation within an oligomer create subunits that are best described as chain-linked chromophores with energies determined by the length of the conjugated segment. This property, in particular, make **nT** oligomers and their polymeric counterparts useful light harvesters for solar cells as the various configurations absorb across a wide range of the visible spectrum.

Incorporating the **NDI** end-caps with the thiophene oligomers to create acceptor-donor-acceptor (ADA) assemblies allows us to study photoinduced charge separation and recombination, and how structure and delocalization in the thiophene segment influence the dynamics of these processes. Selective excitation of the thiophene donor leads to charge

separation (Eq. 1) creating an **NDI** radical anion (**NDI**$^{\bullet-}$) and a thiophene cation (i.e. polaron, **nT**$^{\bullet+}$), e.g.

$$\text{NDI-nT-NDI} + h\nu \rightarrow \text{NDI-}^{1}(\text{nT})^{*}\text{-NDI} \rightarrow \text{NDI-(nT)}^{\bullet+}\text{-NDI}^{\bullet-} \quad (6.1)$$

$$\text{NDI-(nT)}^{\bullet+}\text{-NDI}^{\bullet-} \rightarrow \text{NDI-nT-NDI} \quad (6.2)$$

The **nT-NDI** oligomers integrate an electron donor and acceptor connected through a phenylene bridge to create a molecular wire-like structure. Variations of these molecular wires, including altering donors,[14] acceptors,[15] and bridge length,[16] are of great interest in solar energy conversion, but overlapping spectral features, and competitive energy and electron transfer pathways make the mechanism of charge separation and recombination difficult to quantify.[17-20] Understanding the effects of thiophene donor length on the charge separation and recombination dynamics is extremely beneficial for the continued development and implementation of these molecular wires in solar cell devices.

Our previous work on this series determined that these electron transfer reactions are essentially activationless occurring on the ultrafast timescale.[21] The current work, the second of two papers, delves into the mechanism and dynamics of the charge separation and recombination processes of the **nT-NDI** oligomers, and how that relates to the excited state dynamics of the **nT** oligomers.

6.2. Experimental Methods.

6.2.1. Sample Preparation.

The synthesis and structural characterization of the **nT** and **nT-NDI** oligomers are described elsewhere.[21] Prior to transient absorption experiments, the solid samples were dissolved in CH_2Cl_2 and transferred to a 1mm path length cuvette with a peak absorbance of 0.1 monitored by UV-visible absorption spectroscopy. The samples were degassed with argon for approximately 10 minutes to prevent any effects due to the presence of oxygen. Studies done at different concentrations and powers show no significant differences. Samples were stirred throughout the duration of the transient absorption experiment.

6.2.2. UV-Visible Absorption Spectroscopy.

UV-visible absorption spectra were collected using an Agilent 8453 diode array. The UV-Vis spectra were monitored before and after transient absorption experiments to ensure no photodegradation had occurred.

6.2.3. Femtosecond Transient Absorption.

Femtosecond transient absorption (fsTA) experiments were conducted with a mode-locked Ti:Sapphire laser (Clark-MXR 2001) in a pump-probe configuration. The generated 775 nm light (150 fs pulse) is split at the output with 90% of the beam dedicated to the pump pulse and 10% to the probe. The 425 nm (100 nJ/pulse) pump is generated in a home-built optical parametric amplifier (OPA) where the generated idler is frequency doubled to 940 nm and combined with residual 775 nm to undergo sum frequency generation. The probe pulse is sent through a mechanically controlled delay stage to control the distance between pump and probe. After the delay stage, the 775 nm is focused into a rotating CaF_2 window to generate a white light probe (λ = 325-750) through supercontinuum generation. The polarization of the probe is vertical and the

pump is set to magic angle (54.7°) relative to the probe. The pump and probe beams are focused and spatially overlapped at the sample and changes of the white light probe with time are monitored by a CMOS sensor.

6.3. Results and Discussion.

6.3.1. Steady State Absorption Spectra and Photoexcitation.

The steady state absorption spectra of the thiophene-only, the **nT** series, exhibit a broad, structureless π-π* absorption that red shifts with chain length (Figure 6.2, Table 6.1). The largest red shift occurs between **4T** and **6T** due to the extended conjugation length. The degree of red shifting decreases for the subsequent oligomers, suggesting that the effective conjugation length is ~8-10 thiophene repeats. Addition of the NDI end-caps introduces two vibronically-resolved absorption features in the near-UV, corresponding to the π-π* absorptions of the **NDI** units.[22] The absorption profiles of the **nT-NDI** oligomers are, qualitatively, a superposition of the structureless absorption bands of the **nT** series and the sharp **NDI** peaks. This superposition suggests weak coupling between donor and acceptor allowing for selective excitation of the thiophene donor. Note that the thiophene absorption maximum in **4T-NDI** (and to a lesser extent, **6T-NDI**) is significantly perturbed relative to the corresponding **nT** oligomers by extended conjugation length introduced by the phenylene bridge that links the thiophene segments to the diimide N-atom.

Table 6.1. Thiophene absorption peak wavelength from steady state absorption spectrum.

n	4	6	8	10	12
λ_{max}, nm (**nT**)	378	412	429	436	440
λ_{max}, nm (**nT-NDI**)	409	428	433	439	440

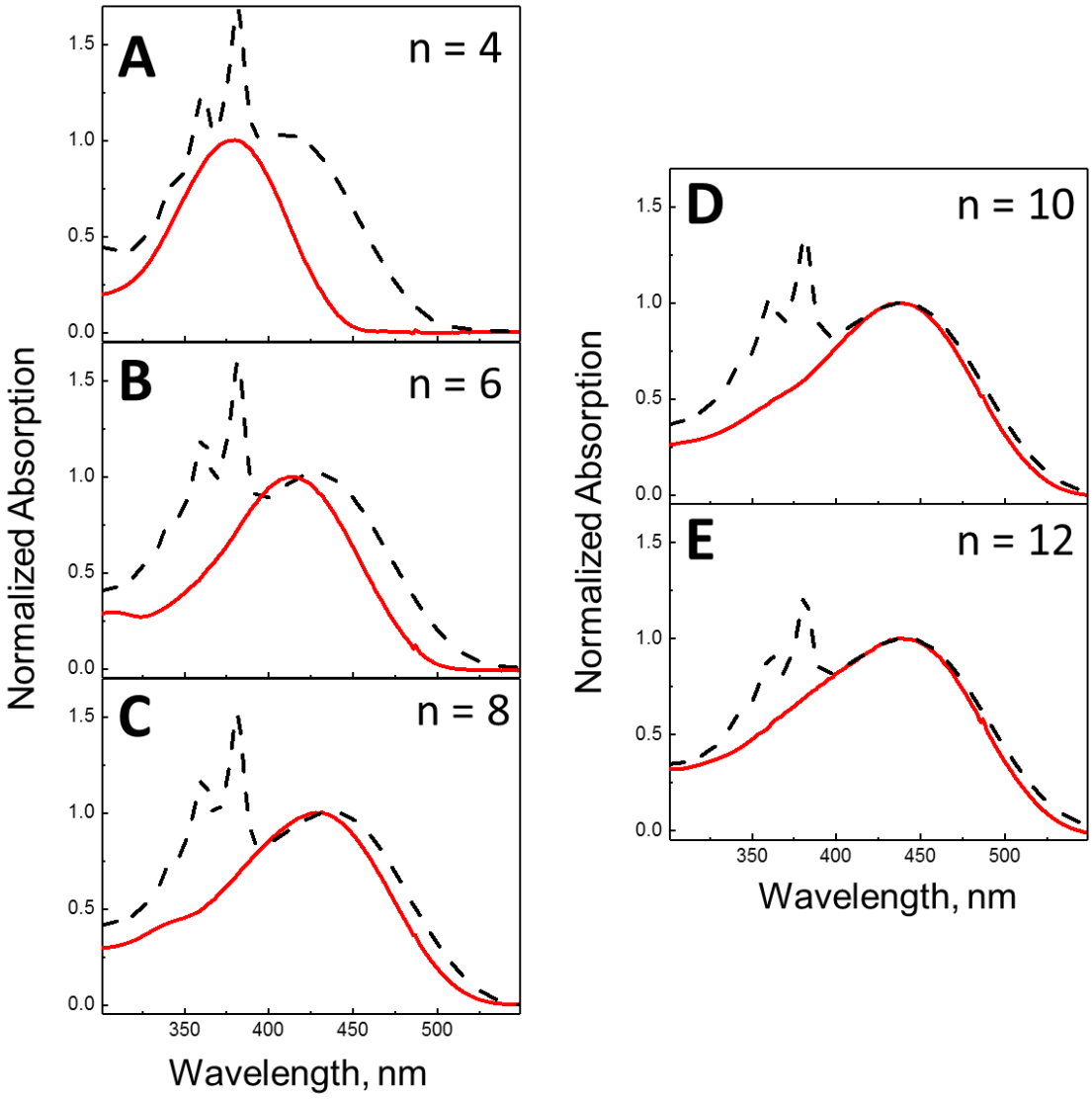

Figure 6.2. Normalized UV-Visible absorption spectra of **nT** (red) and **nT-NDI** (black-dotted line) with A. n = 4, B. n = 6, C. n = 8, D. n = 10, E. n = 12 in CH_2Cl_2 at 25°C.

The structureless thiophene absorption in the steady state arises from the conformational freedom these oligomers have in the ground state in solution.[23] The structural disorder introduced by breaks in the π-conjugation increases with thiophene length. The small segments created by these breaks can absorb photons and undergo structural relaxation in the excited state to a quinoidal-like planar structure, resulting in a structured emission profile.[10, 24] The shifts in the

spectra speak to the size of the exciton in the **nT** oligomers. The exciton created by photoexcitation likely extends across the entire chain in the smallest oligomer (**4T**), while the limiting nature of the spectral position suggest that for larger oligomers (n > 6), the excited state extends across 5-6 monomers.[25]

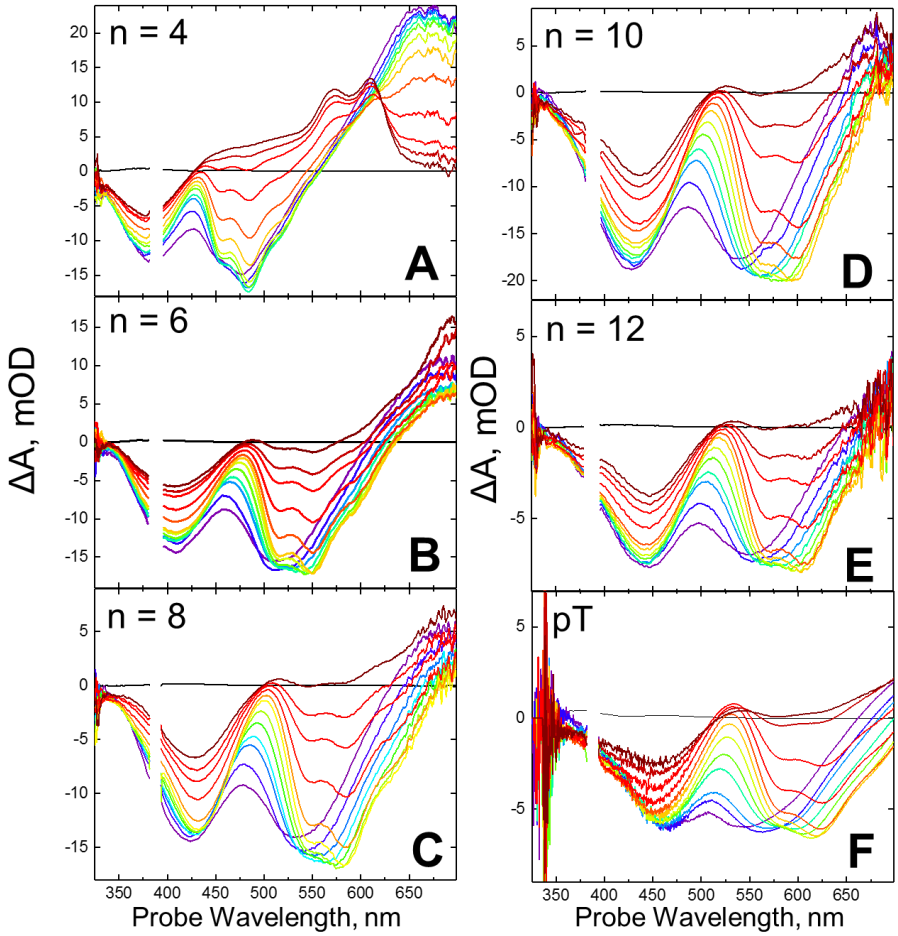

Figure 6.3. Transient absorption spectra of (A) **4T**, (B) **6T**, (C) **8T**, (D) **10T**, (E) **12T**, (F) **pT** in CH_2Cl_2 at 25°C after photoexcitation at 388 nm (100 nJ/pulse) at pump-probe delays of -6 (black), 0.33 (purple), 1, 3, 5, 10, 20, 50, 100, 250, 500, 750, 1300 (dark red) ps. The pT spectra has been reproduced from REF 9.

6.3.2. Excited State Dynamics of nT Oligomers.

The transient absorption spectra of the **nT** series and **pT** at 300 fs after 388 nm photoexcitation (Figure 6.3, A-E, purple) contains several characteristic features[26] of thiophene excited states including a ground state bleach (GSB) in the blue, stimulated emission from the singlet excited state (SE) between 500-600 nm and a singlet excited state absorption (ESA) in the red. The SE rapidly red shifts in oligomers with n > 4, evolving from a broad, structureless band to a vibronically-resolved SE reminiscent of the steady state emission.[21] The SE decays with time constants ranging from 249 ps in **4T** to 585 ps in **12T** (Table 6.2), similar to the lifetime (580 ps) reported for **pT** by Wang and coworkers.[27]

Table 6.2. Results of fit of simulated emission decay for **nT** series.

n	**4**	**6**	**8**	**10**	**12**
τ_1, ps		0.26	0.24	0.4	0.32
τ_2, ps	0.47	3	4	4.8	4.0
τ_3, ps	249	448	467	562	585

The rapid red shifts of the SE bands in the longer oligomers (n ≥ 6) without significant loss of the GSB amplitude, reflects evolution of the exciton to lower energy states (i.e., longer conjugated segments). In **pT**, this relaxation is often attributed to a combination of exciton migration (i.e. energy transfer from a shorter, high-energy segment to longer segments with lower energies) and torsional relaxation to produce a more planar structure in the vicinity of the excitation, lowering the energy of the exciton.[24-25, 28] The observation of the same behavior in oligomers with as few as 6 monomer units (**6T**) as that in **pT** suggests that the rapid SE band red shift is most likely a consequence of conformational relaxation, rather than exciton hopping. In addition to exhibit a significant shift in position, the SE band shows a substantial change in its spectral shape, evolving from a broad and featureless band at early times to a structured spectrum

with a clear vibronic progression. The emergence of the vibronic structure most likely reflects progression towards a narrow distribution of conformational states, combined with stronger electron-vibrational coupling to high frequency modes.

While the spectral evolution observed in the 4 longest oligomers (**6T**-**12T**) qualitatively resembles that observed in **pT**, the spectral dynamics of the shortest oligomer (**4T**) is noticeably different. Unlike the longer chains, the SE in 4T contains vibronic structure at the earliest observation point, and shows no appreciable time-dependent red-shift. These observations suggest that the excited state produced by optical excitation is similar to the emitting state, and that **4T** dynamics are free of the conformational relaxation processes taking place in the longer chains.

The decay of the SE band reflects relaxation of the **nT** excited state back to the ground state. The lifetime of the relaxed singlet exciton also increases with length (Table 6.2) where the largest increase occurs between **4T** and **6T** ($\Delta\tau$~200 ps). This is likely due to the significant increase in structural disorder with the addition of two thiophene rings causing a decrease in the Franck Condon factors and, therefore, decreasing the rate of radiationless deactivation of the singlet state.[10, 29] Previously measured quantum yields show a significant increase between **4T** and **6T**,[21] further supporting this increase in structural disorder.

On longer timescales, intersystem crossing (ISC) occurs, as observed by the growth of the triplet state absorption at longer delay times in the red for $\lambda > 600$ nm (Figure 6.2). Although we observe the blue edge of this triplet-triplet absorption (TTA), the peak red-shifts out of the available observation window ($\lambda > 700$ nm) for **10T**, **12T**, and **pT**. The rise of the TTA absorption for **4T**, **6T**, and **8T** (Figure 6.4) occurs with time constants of 337 ps, 1059 ps, and 1220 ps, respectively. Not surprisingly, the rise of the TTA parallels the decay of the singlet

state, with the largest difference in triplet rise-time dynamics lying between **4T** and **6T**, while the growth rate levels off for **6T** and **8T**. The rise times for **6T** and **8T** are in good agreement with previous studies on the ISC dynamics of **pT**, where the measured ISC time constant was 1.2 ns.[30] Together, these observations suggest the behavior of **4T** is molecular in nature while all longer oligomers are approaching the behavior of **pT**.

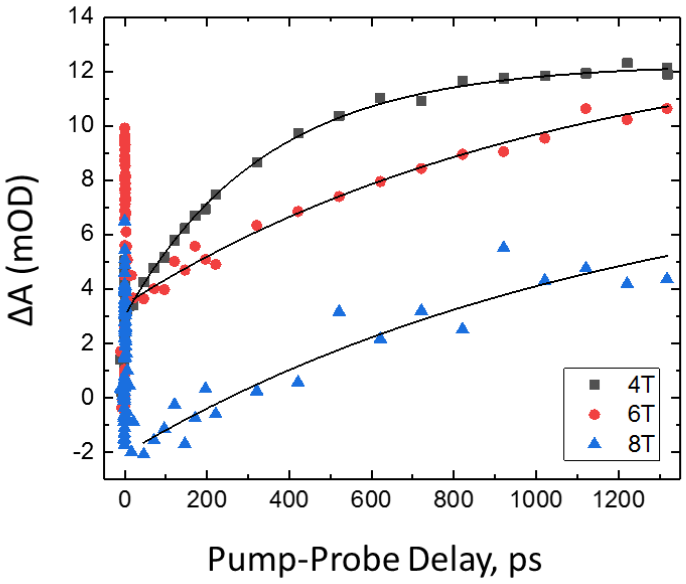

Figure 6.4. Growth of TTA at probe wavelengths of 573 nm, 668 nm, and 672 nm for **4T**, **6T**, and **8T**, respectively. Oligomers were photoexcited at 388 nm in CH_2Cl_2.

6.3.3. Charge Separation and Recombination Dynamics in nT-NDI.

The early time transient absorption spectra of the **nT-NDI** series (Figure 6.5, A-E), photoexcited at 425 nm to avoid direct excitation of **NDI**, has similar spectral features to that of the **nT** series: a GSB in the blue, SE in the mid-visible and a singlet ESA in the red. Using **8T-NDI** (Figure 6.5C) as an example, the magnitude of the SE signal is partially quenched relative to the same time point in **8T** and quickly decays. Within 10 ps, new features appear including two sharp bleach features at 360 nm and 380 nm, a large positive peak at 490 nm, and a smaller

peak at 610 nm, consistent with bleaching of the **NDI** ground state and formation of the anion radical, **NDI**$^{\bullet-}$.[22] The absorption band increases slightly in intensity before decaying, signifying a change from the singlet excited state (^{1}**8T**) to a thiophene cation (**8T**$^{\bullet+}$).[21] The features related to this charge separated state (CSS, **8T**$^{\bullet+}$**-NDI**$^{\bullet-}$) return nearly to baseline within 50 ps, much faster than the microsecond lifetime of **8T** triplet state.

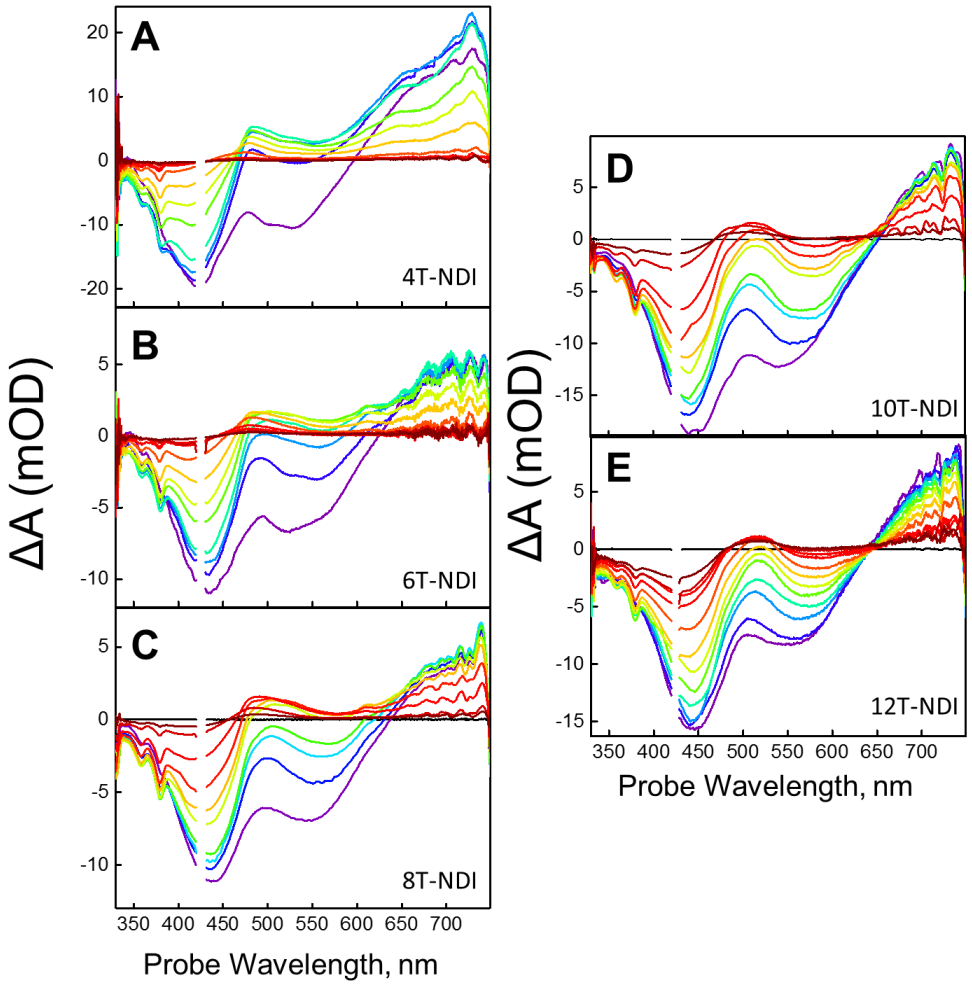

Figure 6.5. Transient absorption spectra of (A) **4T-NDI** (B) **6T-NDI** (C) **8T-NDI** (D) **10T-NDI** (E) **12T-NDI** photoexcited at 425 nm (100 nJ/pulse) at time delays of -6 (black), 0.2 (purple), 0.85, 1.5, 2.3, 4.0, 5.0, 7.0, 11.4, 20.5, 27, 35, 50 ps (dark red) in CH_2Cl_2.

The transient absorption spectra of the **nT-NDI** series as a whole reveal major differences in the charge separation and recombination dynamics with the length of the thiophene backbone.

Like the **nT** series, the same major features are present in all **nT-NDI** compounds, but the behavior varies from **4T-NDI** through **12T-NDI**.

With the creation of the CSS, the spectral features are not static, suggesting conformational relaxation is occurring in conjunction with charge separation. Within 850 fs, the SE in **4T-NDI** is completely quenched and evidence of the CSS is apparent. Some vibronic structure is present in the **4T-NDI** SE, though it does not evolve prior to charge separation. With the addition of two thiophene units in **6T-NDI**, the disappearance of the SE slows, but it does not shift. In the longer chains (**8T-NDI**-**12T-NDI**), however, there is a pronounced red shift in the SE as it decays. This is indicative of structural relaxation as charge separation occurs, though the lack of vibronic structure suggests charge separation is faster than complete structural relaxation. In addition to the SE, the **NDI**$^{\bullet-}$ peak at 490 nm blue shifts and broadens as it decays implying structural relaxation continues through the charge separation process.

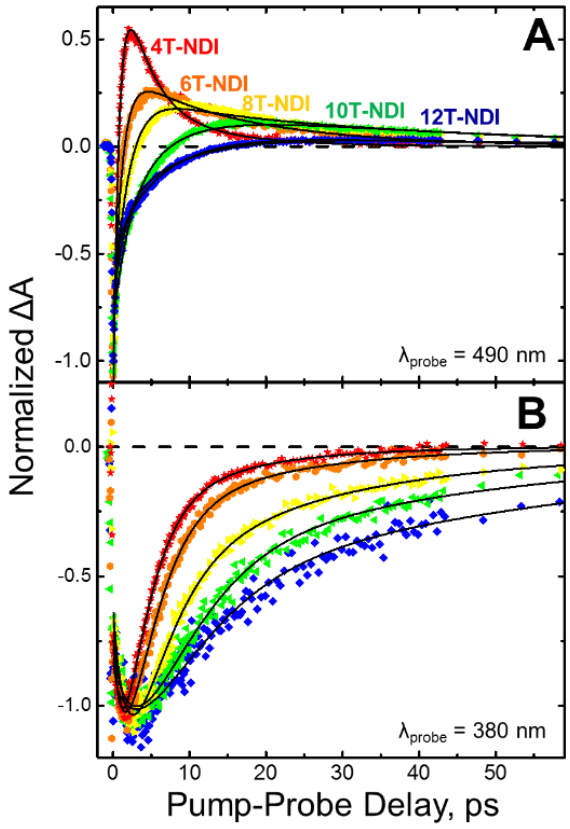

Figure 6.6. (A) Normalized transient absorption kinetics at 490 nm and (B) 380 nm after 425 nm excitation of **4T-NDI** (red), **6T-NDI** (orange), **8T-NDI** (yellow), **10T-NDI** (green), and **12T-NDI** (blue) in CH_2Cl_2 at 25°C. Fits are shown as black lines.

To understand the dynamics and mechanism of charge separation and recombination, the kinetics were monitored at two wavelengths, 380 nm and 490 nm, corresponding to the **NDI** GSB and the **NDI**$^{\bullet-}$, respectively (Figure 6.6). The traces were fit to a sum of four exponentials (eq. 6.3) simultaneously with shared time constants consisting of two growth and two decay components (Table 6.3). The biexponential rise in the signals correspond to the growth of the CSS, where τ_1 is ultrafast and independent of length, while τ_2 is dependent on the length of the thiophene segment. Likewise, recombination is biphasic with a fast (τ_3) and slow (τ_4) component;

however, both components are dependent on thiophene length. Similar recombination dynamics have been observed in wire-like[31] and dendrimeric structures.[15]

$$y = A_1 e^{-x/\tau_1} + A_2 e^{-x/\tau_2} + A_3 e^{-x/\tau_3} + A_4 e^{-x/\tau_4} \quad (6.3)$$

Table 6.3. Results of global fit at 380 nm and 490 nm for **nT-NDI** complexes.

	τ_1, fs	**τ_2, ps**	**τ_3, ps**	**τ_4, ps**
4T-NDI	300	0.90	3.83	14.8
6T-NDI	355	1.91	3.66	18.5
8T-NDI	236	2.38	4.37	23.6
10T-NDI	276	4.34	6.27	44.7
12T-NDI	289	5.06	6.93	58.3

The first time component, τ_1 (Table 6.3), is ultrafast and independent of chain length. Because this time component is ~300 fs, it is likely that a portion of this ultrafast charge separation is occurring within our instrument response. The timescale for this process suggests ultrafast charge separation is more complicated than simple donor-acceptor dynamics. A possible mechanism for the ultrafast process (τ_1) is shown in Figure 6.7A, where photoexcitation near the end of the chain creates a delocalized excited state across the phenylene bridge with partial positive character on the thiophene and partial negative on the **NDI** end-cap. Twisting of the bridge localizes the positive and negative charges creating the CSS.

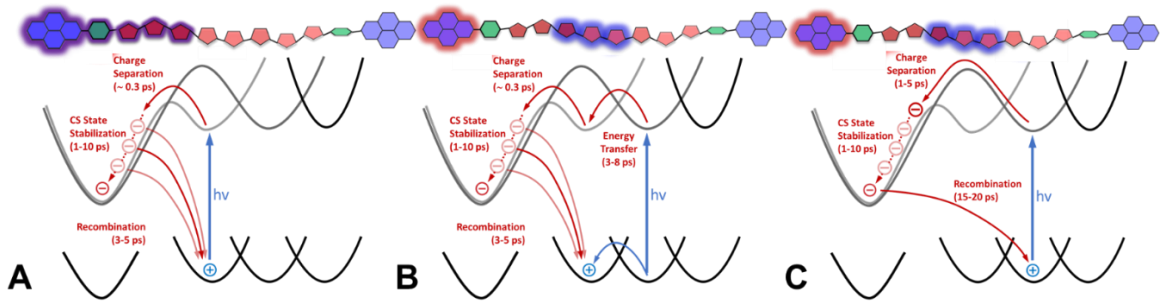

Figure 6.7. Mechanism of charge separation and recombination in **nT-NDI** for photoexcitation (A) at end of thiophene chain (red pentagons), delocalized across phenylene bridge (green hexagon) (B) center of thiophene chain where energy transfer is followed by ET, (C) center of thiophene chain where long-range ET occurs. See text for description.

Evidence for the production of this charge-transfer excited state lies in the transient absorption spectra. Interestingly, the **nT-NDI** series exhibit a blue shift in the **NDI**$^{\bullet-}$ absorption at 490 nm (Figure 6.5). This blue shift is a result of the localization of the charges through the bridge twisting.[32] The magnitude of this shift decreases with increasing chain length (Figure 6.8) with the largest shift occurring in **4T-NDI** (Figure 6.8A). The minimal structural heterogeneity in **4T-NDI** allows this pathway towards charge separation to dominate. In the longer chains, structural relaxation and slow charge separation diminish this effect to the point where it is not present in **12T-NDI**.

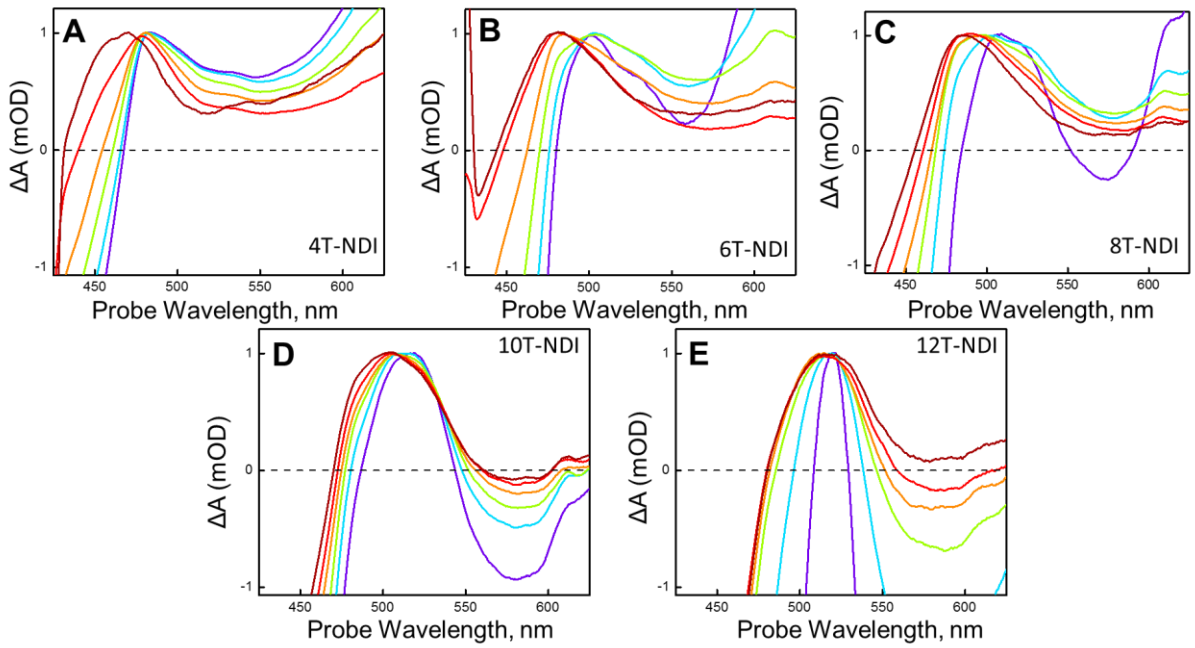

Figure 6.8. Snapshot of the **NDI**$^{\bullet-}$ band at ~490 nm in (A) **4T-NDI** at pump probe-delays of 1.77 (purple), 2.5, 5, 6, 10, 20 ps (dark red) (B) **6T-NDI** at pump-probe delays of 2 (purple), 3, 4.5, 8, 14, and 20 ps (dark red), (C) **8T-NDI** at pump-probe delays of 4 (purple), 6, 9, 10, 14, and 30 ps (dark red), (D) **10T-NDI** at pump-probe delays of 9, 10, 12, 14,17, and 30 ps (dark red), and (E) **12T-NDI** at pump-probe delays of 8 (purple), 11, 20, 30, 37, and 50 ps (dark red) in CH_2Cl_2 photoexcited at 425 nm, normalized to visualize the blue shift as a function of thiophene length.

Slower charge separation, represented by τ_2, ranges from 900 fs through 5 ps from **4T-NDI** to **12T-NDI**, respectively. In this case, photoexcitation occurs in the center of the chain and there are two paths for charge separation (Figure 6.7, B-C): energy transfer or torsional relaxation followed by electron transfer (ET) (Figure 6.7B) and long-range ET (Figure 6.7C). In our previous paper, the charge separation process was determined to be activationless and nonadiabatic.[21] Long range ET proceeds through a typical Marcus donor-acceptor interaction,

where the distance between the exciton created in the center of the chain and the **NDI** acceptor dictates the rate. However, a second mechanism is present where the exciton may undergo an energy transfer step to a chromophore closer to the **NDI** and then undergo ET to create the CSS.

The behavior of the SE of the **nT-NDI** series points to the dominant mechanism for slow charge separation. In the short oligomers (**4T-NDI**, **6T-NDI**), no apparent shift in the SE suggests that slow charge separation proceeds through long range ET. Longer oligomers (**8T-NDI**–**12T-NDI**) exhibit a red shift in the SE indicative of some torsional relaxation or energy trasnfer, as in the case of the **nT** series. Complete excited state structural relaxation does not occur in the **nT-NDI** series as there is no vibronic progression observed. Instead, this energy transfer/ET mechanism is occurring in conjunction with long range ET preventing full excited state relaxation in favor of CSS creation.

The monitored kinetics exhibit a biexponential decay back to baseline, which is not surprising considering the proposed mechanism for charge separation in Figure 6.7. However, unlike charge separation, both recombination time components are dependent on the length of the oligomer. The fact that the timescale for recombination is under 100 ps in all **nT-NDI** compounds agrees with our previous thermodynamics calculations,[21] which determined that for all of the oligomers recombination occurs in the Marcus inverted region. Physically, a distribution of thiophene cations (i.e. polarons) at different distances from the **NDI**$^{\bullet-}$ leads to a length dependence in both τ_3 and τ_4. This is also further evidence for an energy transfer/ET mechanism in addition to long range ET.

6.3.4. Conclusions.

We investigated the ultrafast excited state dynamics and charge separation/recombination dynamics of a series of **nT** and ADA **nT-NDI** oligomers, respectively. Photoexcitation of the **nT** oligomers creates a localized exciton somewhere along the chain that undergoes rapid structural relaxation via planarization and/or energy transfer (n = 10, 12) within 10s of picoseconds. Introduction of the **NDI** acceptor end-caps to produce the **nT-NDI** oligomers inhibits this structural relaxation in favor of rapid charge separation and recombination after selective excitation of the thiophene backbone. Timescales of electron transfer depend on the location of photoexcitation along the backbone, where excitations near the acceptor result in a 300 fs component, independent of length. An exciton created in the center of the chain must undergo long distance electron transfer to an **NDI**, or an exciton migration step, followed by electron transfer. The former mechanism is dominant in the shorter chains ($n \leq 8$), while both are likely occurring in the longer chains (n = 10, 12). The lifetime of the charge separated state increases significantly between **4T-NDI** and **12T-NDI** from 14.8 ps to 58.3 ps. The observed dynamics present a clear mechanistic picture of charge separation and recombination in a donor-acceptor system incorporating π-conjugated thiophene oligomers. The information gained in this study provide a framework to improve the efficiencies of these molecular wire-like structures for use in solar cells.

REFERENCES

1. Chu, P. H.; Zhang, L.; Colella, N. S.; Fu, B. Y.; Park, J. O.; Srinivasarao, M.; Briseno, A. L.; Reichmanis, E. Enhanced Mobility and Effective Control of Threshold Voltage in P3HT-Based Field-Effect Transistors via Inclusion of Oligothiophenes. *Acs Appl Mater Inter* **2015,** *7* (12), 6652-6660.

2. Barbarella, G.; Melucci, M.; Sotgiu, G. The versatile thiophene: An overview of recent research on thiophene-based materials. *Adv Mater* **2005,** *17* (13), 1581-1593.

3. Beaujuge, P. M.; Frechet, J. M. J. Molecular Design and Ordering Effects in pi-Functional Materials for Transistor and Solar Cell Applications. *J Am Chem Soc* **2011,** *133* (50), 20009-20029.

4. Brennaman, M. K.; Dillon, R. J.; Alibabaei, L.; Gish, M. K.; Dares, C. J.; Ashford, D. L.; House, R. L.; Meyer, G. J.; Papanikolas, J. M.; Meyer, T. J. Finding the Way to Solar Fuels with Dye-Sensitized Photoelectrosynthesis Cells. *J Am Chem Soc* **2016,** *138* (40), 13085-13102.

5. Ortmann, F.; Radke, K. S.; Gunther, A.; Kasemann, D.; Leo, K.; Cuniberti, G. Materials Meets Concepts in Molecule-Based Electronics. *Adv Funct Mater* **2015,** *25* (13), 1933-1954.

6. Kan, B.; Li, M. M.; Zhang, Q.; Liu, F.; Wan, X. J.; Wang, Y. C.; Ni, W.; Long, G. K.; Yang, X.; Feng, H. R., et al. A Series of Simple Oligomer-like Small Molecules Based on Oligothiophenes for Solution-Processed Solar Cells with High Efficiency. *J Am Chem Soc* **2015,** *137* (11), 3886-3893.

7. Brennaman, M. K.; Norris, M. R.; Gish, M. K.; Grumstrup, E. M.; Alibabaei, L.; Ashford, D. L.; Lapides, A. M.; Papanikolas, J. M.; Templeton, J. L.; Meyer, T. J. Ultrafast, Light-Induced Electron Transfer in a Perylene Diimide Chromophore-Donor Assembly on TiO2. *J Phys Chem Lett* **2015,** *6* (23), 4736-4742.

8. Guo, J. C.; Liang, Y. Y.; Xiao, S. Q.; Szarko, J. M.; Sprung, M.; Mukhopadhyay, M. K.; Wang, J.; Yu, L. P.; Chen, L. X. Structure and dynamics correlations of photoinduced charge separation in rigid conjugated linear donor-acceptor dyads towards photovoltaic applications. *New J Chem* **2009,** *33* (7), 1497-1507.

9. Morseth, Z. A.; Wang, L.; Puodziukynaite, E.; Leem, G.; Gilligan, A. T.; Meyer, T. J.; Schanze, K. S.; Reynolds, J. R.; Papanikolas, J. M. Ultrafast Dynamics in Multifunctional Ru(II)-Loaded Polymers for Solar Energy Conversion. *Accounts Chem Res* **2015,** *48* (3), 818-827.

10. Becker, R. S.; deMelo, J. S.; Macanita, A. L.; Elisei, F. Comprehensive evaluation of the absorption, photophysical, energy transfer, structural, and theoretical properties of alpha-oligothiophenes with one to seven rings. *J Phys Chem-Us* **1996,** *100* (48), 18683-18695.

11. Colditz, R.; Grebner, D.; Helbig, M.; Rentsch, S. Theoretical studies and spectroscopic investigations of ground and excited electronic states of thiophene oligomers. *Chem Phys* **1995,** *201* (2-3), 309-320.

12. Rentsch, S.; Chosrovian, H.; Grebner, D.; Naarmaan, H. Picosecond Spectroscopic Studies on Thiophene Oligomers in Solution - Size-Dependent Effects. *Synthetic Met* **1993,** *57* (2-3), 4740-4746.

13. Costa, T.; Pina, J.; de Melo, J. S. S. Photophysical processes in polymers and oligomers. *Photochem-Spec Perio* **2009,** *37*, 44-71.

14. Jiang, J. L.; Alsam, A.; Wang, S. S.; Aly, S. M.; Pan, Z. X.; Mohammed, O. F.; Schanze, K. S. Effect of Conjugation Length on Photoinduced Charge Transfer in pi-Conjugated Oligomer-Acceptor Dyads. *J Phys Chem A* **2017,** *121* (26), 4891-4901.

15. Gong, Z.; Bao, J. H.; Nagai, K.; Iyoda, T.; Kawauchi, T.; Piotrowiak, P. Generation Dependent Ultrafast Charge Separation and Recombination in a Pyrene-Viologen Family of Dendrons. *J Phys Chem B* **2016,** *120* (18), 4286-4295.

16. Goldsmith, R. H.; Sinks, L. E.; Kelley, R. F.; Betzen, L. J.; Liu, W. H.; Weiss, E. A.; Ratner, M. A.; Wasielewski, M. R. Wire-like charge transport at near constant bridge energy through fluorene oligomers. *P Natl Acad Sci USA* **2005,** *102* (10), 3540-3545.

17. Balaji, G.; Kale, T. S.; Keerthi, A.; Della Pelle, A. M.; Thayumanavan, S.; Valiyaveettil, S. Low Band Gap Thiophene-Perylene Diimide Systems with Tunable Charge Transport Properties. *Org Lett* **2011,** *13* (1), 18-21.

18. Wonneberger, H.; Ma, C. Q.; Gatys, M. A.; Li, C.; Bauerle, P.; Mullen, K. Terthiophene-Perylene diimides Color Tuning via Architecture Variation. *J Phys Chem B* **2010,** *114* (45), 14343-14347.

19. Sartin, M. M.; Huang, C.; Marshall, A. S.; Makarov, N.; Barlow, S.; Marder, S. R.; Perry, J. W. Nonlinear Optical Pulse Suppression via Ultrafast Photoinduced Electron Transfer in an Aggregated Perylene Diimide/Oligothiophene Molecular Triad. *J Phys Chem A* **2014,** *118* (1), 110-121.

20. Araki, Y.; Luo, H. X.; Nakamura, T.; Fujitsuka, M.; Ito, O.; Kanato, H.; Aso, Y.; Otsubo, T. Photoinduced charge separation and charge recombination of oligothiophene-viologen dyads in polar solvent. *J Phys Chem A* **2004,** *108* (48), 10649-10655.

21. Jones, A. L.; Gish, M. K.; Zeman, C. J.; Papanikolas, J. M.; Schanze, K. S. Photoinduced Electron Transfer in Naphthalene Diimide End-Capped Thiophene Oligomers. *J Phys Chem A* **2017,** *121* (50), 9579-9588.

22. Greenfield, S. R.; Svec, W. A.; Gosztola, D.; Wasielewski, M. R. Multistep photochemical charge separation in rod-like molecules based on aromatic imides and diimides. *Journal of the American Chemical Society* **1996,** *118* (28), 6767-6777.

23. Grebner, D.; Helbig, M.; Rentsch, S. Size-Dependent Properties of Oligothiophenes by Picosecond Time-Resolved Spectroscopy. *J Phys Chem-Us* **1995,** *99* (46), 16991-16998.

24. Busby, E.; Carroll, E. C.; Chinn, E. M.; Chang, L. L.; Moule, A. J.; Larsen, D. S. Excited-State Self-Trapping and Ground-State Relaxation Dynamics in Poly(3-hexylthiophene) Resolved with Broadband Pump-Dump-Probe Spectroscopy. *J Phys Chem Lett* **2011,** *2* (21), 2764-2769.

25. Wells, N. P.; Blank, D. A. Correlated exciton relaxation in poly(3-hexylthiophene). *Phys Rev Lett* **2008,** *100* (8).

26. Chosrovian, H.; Grebner, D.; Rentsch, S.; Naarmann, H. Size-Dependent Transient-Behavior of Thiophene Oligomers Studied by Picosecond Absorption-Spectroscopy. *Synthetic Met* **1992,** *52* (2), 213-225.

27. Wang, L.; Puodziukynaite, E.; Grumstrup, E. M.; Brown, A. C.; Keinan, S.; Schanze, K. S.; Reynolds, J. R.; Papanikolas, J. M. Ultrafast Formation of a Long-Lived Charge-Separated State in a Ru-Loaded Poly(3-hexylthiophene) Light-Harvesting Polymer. *J Phys Chem Lett* **2013,** *4* (14), 2269-2273.

28. Wells, N. P.; Boudouris, B. W.; Hillmyer, M. A.; Blank, D. A. Intramolecular exciton relaxation and migration dynamics in poly(3-hexylthiophene). *J Phys Chem C* **2007,** *111* (42), 15404-15414.

29. Chosrovian, H.; Rentsch, S.; Grebner, D.; Dahm, D. U.; Birckner, E.; Naarmann, H. Time-Resolved Fluorescence Studies on Thiophene Oligomers in Solution. *Synthetic Met* **1993,** *60* (1), 23-26.

30. Kraabel, B.; Moses, D.; Heeger, A. J. Direct Observation of the Intersystem Crossing in Poly(3-Octylthiophene). *J Chem Phys* **1995,** *103* (12), 5102-5108.

31. Davis, W. B.; Svec, W. A.; Ratner, M. A.; Wasielewski, M. R. Molecular-wire behaviour in p-phenylenevinylene oligomers. *Nature* **1998,** *396* (6706), 60-63.

32. Koch, M.; Myahkostupov, M.; Oblinsky, D. G.; Wang, S. W.; Garakyaraghi, S.; Castellano, F. N.; Scholes, G. D. Charge Localization after Ultrafast Photoexcitation of a Rigid Perylene Perylenediimide Dyad Visualized by Transient Stark Effect. *J Am Chem Soc* **2017,** *139* (15), 5530-5537.